Measurement of Neutral Mesons via Photon Conversions in p-Pb Collisions at 5.02 TeV with ALICE

Annika Passfeld, Dissertation 2018

WWU
MÜNSTER

wissen.leben

Experimentelle Physik

Measurement of Neutral Mesons via Photon Conversions in p–Pb Collisions at 5.02 TeV with ALICE

Inauguraldissertation
zur Erlangung des Doktorgrades
der Naturwissenschaften im Fachbereich Physik
der Mathematisch-Naturwissenschaftlichen
Fakultät
der Westfälischen Wilhelms-Universität Münster

vorgelegt von
Annika Passfeld
aus Münster
– 2018 –

Dekan: Prof. Dr. M. Klasen
Erster Gutachter: Prof. Dr. J. P. Wessels
Zweiter Gutachter: PD Dr. C. Klein-Bösing

Tag der Disputation:
Tag der Promotion:

Contents

Chapter 1

Motivation and Theoretical Background

The Quark-Gluon Plasma (QGP) is a state of matter that is thought to have existed up to about a microsecond after the Big Bang. In this plasma the quarks and gluons are not confined into hadrons like it is for our normal hadronic matter, but exist in a deconfined phase. In the laboratory this phase can be created in heavy-ion collisions at high collision energies where the temperature is sufficiently high to enable the phase transition. This is for example possible in Pb–Pb collisions at the Large Hadron Collider (LHC). With the ALICE detector, located at the LHC, such heavy-ion collisions are studied in order to characterize the properties of the Quark-Gluon Plasma and to gain knowledge about the early universe and the formation of the matter that surrounds us all.

For this purpose, several different observables are studied as evidence for the QGP formation. One signature is the suppression of hadrons in heavy-ion collisions compared to proton-proton collisions, studied via the nuclear modification factor, defined as:

$$R_{\mathrm{AA}}(p_{\mathrm{T}}) = \frac{\mathrm{d}^2 N^{\mathrm{AA}}/\mathrm{d}y\mathrm{d}p_{\mathrm{T}}}{\langle T_{\mathrm{AA}} \rangle \mathrm{d}^2 \sigma^{\mathrm{PP}}/\mathrm{d}y\mathrm{d}p_{\mathrm{T}}}$$

It is the ratio of the particle yield measured in Pb–Pb collisions and the corresponding pp cross section, scaled with the nuclear overlap function $\langle T_{\mathrm{AA}} \rangle$. In the absence of nuclear effects, the R_{AA} should be consistent with unity for transverse momenta above $2\,\mathrm{GeV}/c$ and Pb–Pb collisions could be interpreted as a simple superposition of pp collisions.

ALI-PUB-81794
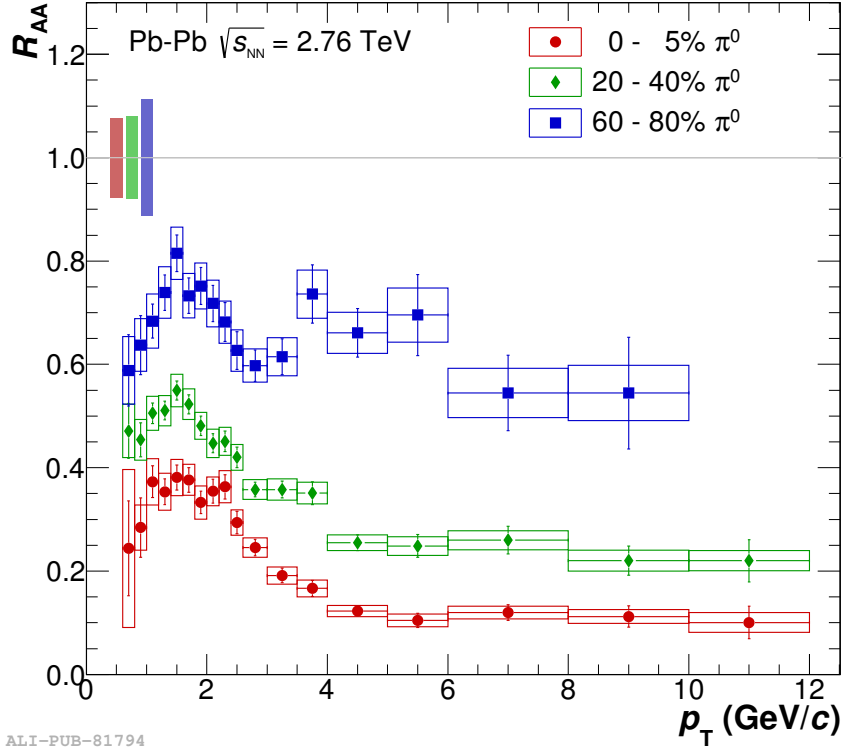
Figure 1.1: Neutral pion nuclear modification factor for different event centralities in Pb–Pb collisions at $\sqrt{s} = 2.76$ TeV. [1]

The nuclear modification factor for neutral pions in Pb–Pb collisions at $\sqrt{s} = 2.76$ TeV is shown in Fig. 1.1 [1], where a clear suppression compared to unity is seen. The suppression is most pronounced for the most central collisions and is attributed to an energy loss of the produced parton, prior to fragmentation into hadrons, in the created medium, the QGP.

In order to quantify energy loss mechanisms, it becomes evident that a reference measurement is needed, as in case of the R_{AA} the measurement of pp collisions, where, in contrast to Pb–Pb collisions, no nuclear effects are present. In addition to the creation of the QGP, which is a hot nuclear matter effect, also so-called cold nuclear matter (CNM) effects can occur, due to the presence of the colliding nuclei. To disentangle these hot and cold nuclear matter effects, p–Pb collisions play an important role, as the formation of a QGP is a priori not expected, while CNM effects are possible. Recent LHC results, however, show that some collective phenomena, which have been attributed to the formation of the QGP in Pb–Pb collisions, are also present in p–Pb and even high multiplicity pp collisions, as for example reported in Refs. [2, 3]. So far, it is not clear how these results can be interpreted: Is the

2

collective behavior due to the formation of maybe small QGP droplets also in p–Pb and pp collisions? Is the recent interpretation of QGP signatures not correct? Or do different processes in the different collision systems lead to the same observed phenomena? These questions make the investigation of the so-called small systems also as a function of particle multiplicity even more important and interesting.

Besides the importance as baseline for Pb–Pb collisions, the measurement of p–Pb collisions at LHC energies also allows for the study of fundamental properties of Quantum Chromodynamics (QCD) like the partonic structure of matter at low parton momentum fraction x [4]. This is possible in particular with the reconstruction of the neutral mesons π^0 and η, as it provides high statistics of identified particles over a large p_T range. In addition, the neutral meson yields are crucial as input for other analyses, like the measurement of direct photons [5, 6] or electrons from heavy flavor decays [7], as they represent the dominant source of background.

In this thesis, the measurement of neutral mesons via photon conversions in p–Pb collisions at 5.02 TeV with ALICE is presented. The following sections focus on some theoretical aspects of the measurement. First, some basic QCD properties and possible cold nuclear matter effects will be treated. The last two sections focus on the pseudoscalar meson nonet, to which the measured π^0 and η meson belong, and on the photon conversion process.

1.1 Basic Properties of Quantum Chromodynamics

Quantum Chromodynamics (QCD) is the quantum field theory of the strong interaction, which is, besides the electromagnetic interaction, the weak interaction and gravity, one of the four fundamental forces in nature. It describes the interaction of particles that carry color charge (hence the name Chromodynamics), which are quarks and gluons, the constituents of hadrons.

QCD is a local non-abelian gauge theory, with symmetry group $SU_c(3)$, connected to the three quark colors: red, green and blue. Local gauge symmetries are always associated with bosonic gauge fields [8], in case of the $SU_c(3)$ with eight gauge fields A_μ^a ($a = 1,2,...,8$), the gluons. They can be compared to the photon, the gauge boson of Quantum Electrodynamics (QED), an abelian gauge symmetry with symmetry group U(1). The photon is the mediator of the electromagnetic force and couples to electrically charged particles, while the photon itself does not carry electric charge. In contrast to that, the gluons themselves carry color charge, or more specific color and anti-color, and thus do not only interact with quarks, but also with each other. This self-interaction is a consequence of the non-abelian gauge symmetry and leads to the main properties of QCD, confinement and asymptotic freedom, which will be discussed later on.

1.1.1 QCD Lagrangian

In a general form, the QCD Lagrangian can be written as [9]

$$\mathcal{L}_{QCD} = -\frac{1}{4} F_{\mu\nu}^a F^{a\mu\nu} + \sum_q \bar{q}_i (i\gamma^\mu D_\mu - m_q)_{ij} q_j , \tag{1.1}$$

where sums over repeating indices are implied. Here, q_i are the quark fields. $F_{\mu\nu}^a$ and D_μ represent the field strength tensor and the covariant derivative:

$$F_{\mu\nu}^a = \partial_\mu A_\nu^a - \partial_\nu A_\mu^a - g_s f^{abc} A_\mu^b A_\nu^c$$
$$(D_\mu)_{ij} = \delta_{ij}\partial_\mu + ig_s T_{ij}^a A_\mu^a \tag{1.2}$$

Here, g_s is the gauge coupling, f^{abc} the structure constants and T_{ij}^a the generators of the Lie group that defines the gauge symmetry.

The first term on the right side of Eq. 1.1 contains the self-coupling of the gluons as characteristic of a gauge theory based on a non-abelian group where the gauge bosons carry the charge of the interaction. The second term is a sum over all quark flavors describing the quark-gluon interaction. A pictorial representation of the QCD Lagrangian is given in Fig. 1.2, with the gluonic term consisting of a free field term and two interaction terms for the triple-gluon and the four-gluon interaction. The fermionic part also owns a free field term as well as a term that represents the coupling of two quarks of color i and j to a gluon of type a.

Figure 1.2: Pictorial representation of the QCD Lagrangian. [9]

1.1.2 Confinement and Asymptotic Freedom

Despite extensive experimental searches, for example for fractionally charged particles [10], free quarks or compound states with color have not been found. Quarks and gluons seem only to exist in color-neutral objects, the hadrons. Those can be baryons, consisting of three valence quarks, all with different color, or mesons, quark-antiquark pairs with color and respective anti-color. This phenomenon is called confinement.

Phenomenologically, confinement can be explained by a quark-antiquark potential of the following form [11]:

$$V_{q\bar{q}}(r) = -\frac{4}{3}\frac{\alpha_s}{r} + \sigma r \,, \tag{1.3}$$

5

with $\alpha_s = \frac{g_s^2}{4\pi}$. The constant σ was found to be of the order of $1\,\text{GeVfm}^{-1}$.

At small distances r, the QCD potential behaves similarly to the QED potential, see Fig. 1.3. For larger distances, the linear term σr becomes dominant and leads to a rising potential that prevents the quark and the antiquark from separation. Phenomenologically, this can be explained by the Lund string model [12]. The gluons that mediate the interaction between quark and anti-quark are treated as field lines. Due to the gluon self-interaction, these color lines attract each other and form a narrow tube or string. If the quark and antiquark are separated, the string is strained and already at a distance of $0.2\,\text{fm}$, the potential energy is larger than the pion mass, so that the production of a new quark-antiquark pair becomes energetically favored. This is when the string breaks and two colorless objects remain.
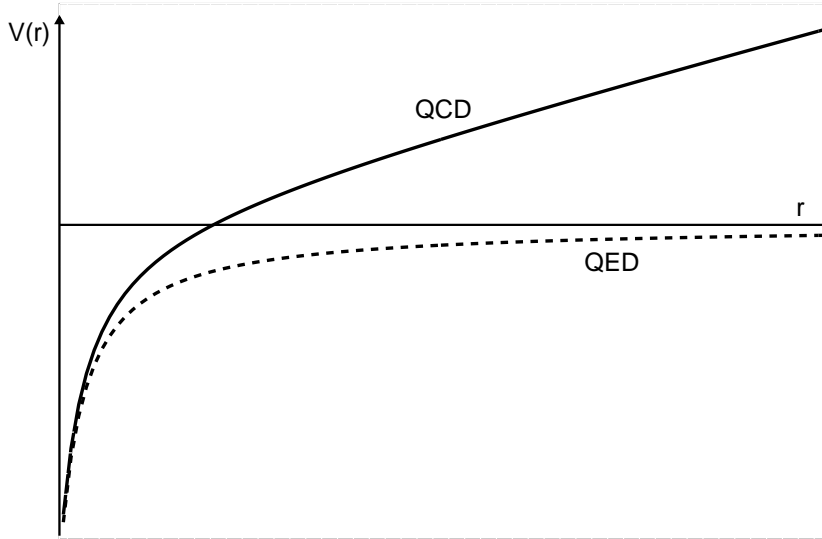
Figure 1.3: Schematic comparison of the QED and QCD potentials.

While the quarks are confined at low energies, they behave as quasi-free particles at small distances or high energies. This behavior is called asymptotic freedom.

It can be understood by looking at the QCD coupling constant α_s, which is technically not a constant, but strongly depends on the momentum transfer Q. At leading order in perturbative QCD, α_s can be written as [9]:

$$\alpha_s(Q^2) = \frac{12\pi}{(33 - 2N_f)\ln(Q^2/\Lambda_{\text{QCD}}^2)}\,,\tag{1.4}$$

with N_f as number of flavors. The QCD scale parameter Λ_{QCD} is experimentally found to be $\mathcal{O}(200\,\text{MeV})$.

A summary of measurements of the QCD coupling constant α_s for different momentum transfers Q is shown in Fig. 1.4 [13]. While the strength of the coupling increases logarithmically for decreasing momentum transfers, it decreases asymptotically for high momenta: $\alpha_s \to 0$ for $Q \to \infty$. The asymptotic freedom is again a consequence of the gluons carrying color charge. The color charge of the quark is smeared since part of it is carried by the surrounding gluon field. With increasing momentum, the resolution gets better and the incoming gluon hence "sees" less of the color charge which leads to the smaller coupling [8].
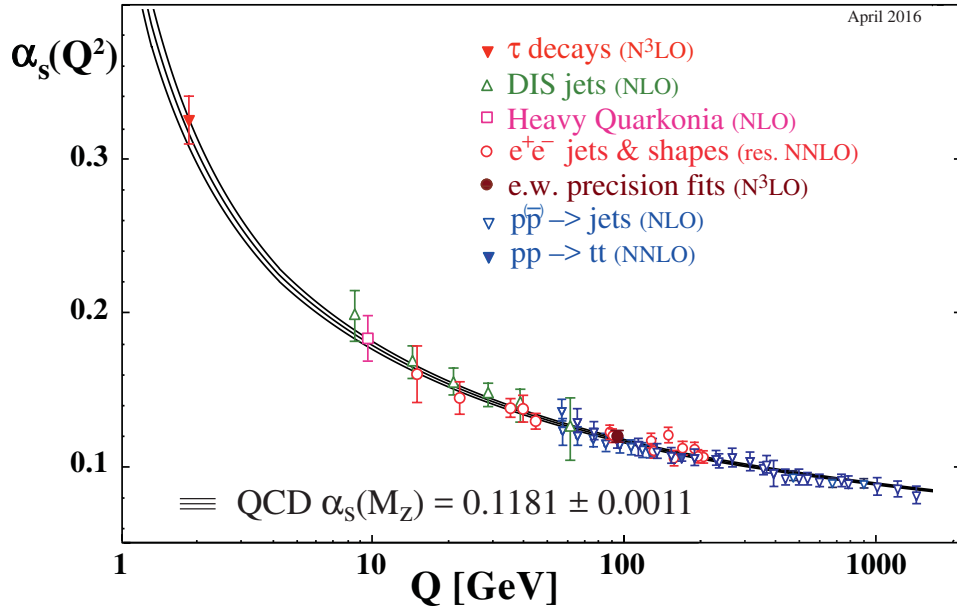

Figure 1.4: Summary of measurements of α_s as a function of the energy scale Q, leading to a world average value for α_s of 0.1181 at the mass of the Z boson. [13]

Due to the running coupling, different theoretical approaches are needed for QCD calculations at different energy scales. At high momentum transfer where the coupling constant is small ($\alpha_s \ll 1$), perturbative QCD (pQCD) calculations can be applied. At lower energies, however, this is not possible. For hadronic processes at an energy scale $\lesssim 1\,\text{GeV}$ the strong coupling constant is ~ 1 and perturbation theory in α_s fails. Here, phenomenological models or Lattice QCD [14], a discrete formulation of QCD on a finite space-time lattice, are often used.

Lattice calculations predict that under certain circumstances quarks and gluons are not confined into hadrons anymore, but exist in a deconfined phase, the so-called Quark-Gluon Plasma (QGP). The QGP can exist at very high temperatures, where the phase space is so densely populated that hadrons overlap and become indistinguishable, or at very high densities.
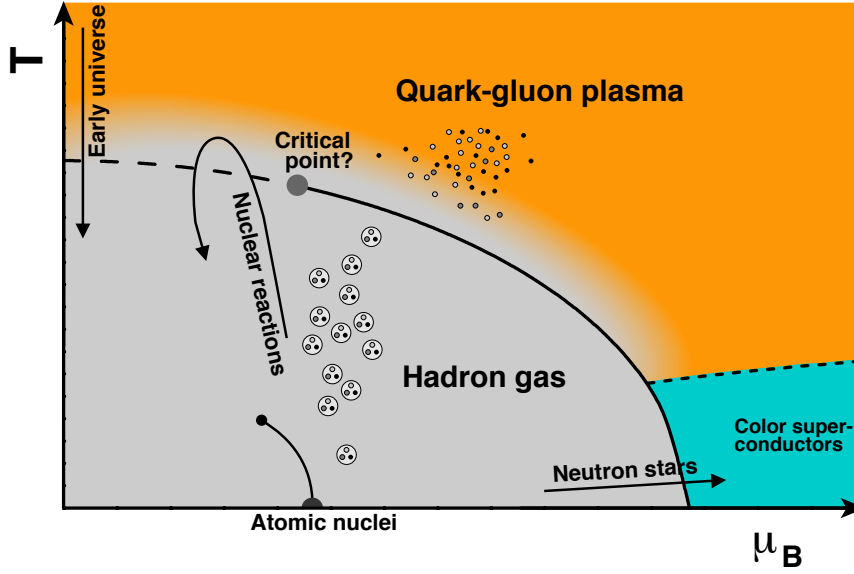

Figure 1.5: QCD phase diagram as function of temperature T and baryochemical potential μ_b. [15]

Figure 1.5 shows the QCD phase diagram as a function of temperature T and baryochemical potential μ_b, based on the current knowledge [15]. So far, it is not clear of which order the phase transition between hadron gas and QGP is, but at small μ_b and high temperatures, a crossover is expected. In Fig. 1.5, this is indicated by the dashed line. For higher net baryon densities, above a possible critical point, a first order phase transition, represented as continuous line, is assumed. For $\mu_b \rightarrow 0$, lattice QCD calculations predict a critical temperature for the phase transition of $T_{\text{crit}} \approx 170\,\text{MeV}$, see Ref. [16] and references therein.

To our current knowledge, the QGP has permeated the first microseconds of the universe. In ultra-relativistic heavy-ion collisions, like in Au–Au collisions at the Relativistic Heavy Ion Collider (RHIC) or in Pb–Pb collisions at the LHC, it can be produced and studied in the laboratory [17], where it exists for a few $\text{fm}/c \approx 10^{-23}\,s$.
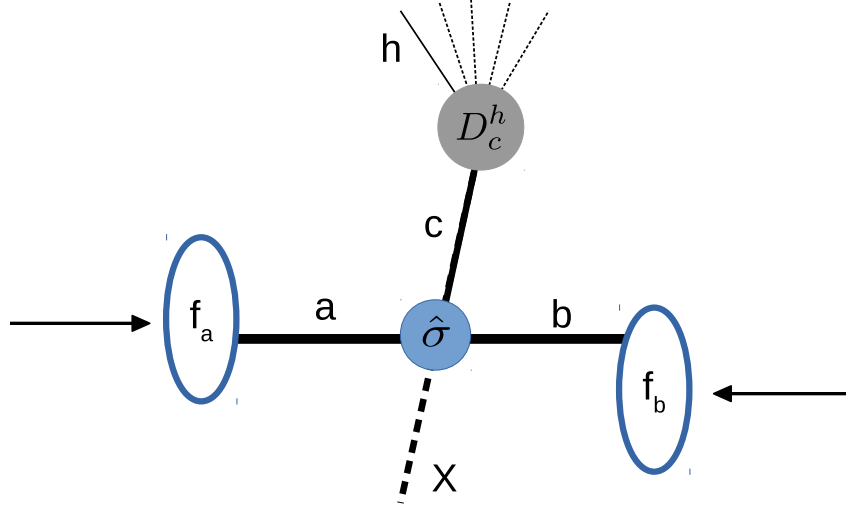
1.1.3 QCD Factorization

Figure 1.6: Illustration of the hard scattering factorization.

The QCD factorization theorem [18] allows for the separation of long-distance and short-distance effects in high energy collisions. As the collision of two hadrons is mainly defined by the hard collision of just two of the constituents, the cross section for the production of a hadron in a proton-proton collision can be factorized as follows [19]:

$$E\frac{d^3\sigma^{pp \to hX}}{d^3p} = \sum_{a,b,c} f_a(x_a,\mu_f) \otimes f_b(x_b,\mu_f) \otimes D_c^h(z_c,\mu_{f'})$$

$$\otimes d\hat{\sigma}_{ab \to cX}(s,\alpha_s,x_a,x_b,z_c,\mu_f,\mu_r,\mu_{f'}) \tag{1.5}$$

Here, $f_a(x_a,\mu_f)$ and $f_b(x_b,\mu_f)$ are the parton distribution functions (PDF) of the partons a and b (these can be quarks, antiquarks or gluons) with parton momentum fractions x_a and x_b in the colliding protons. $D_c^h(z_c,\mu_{f'})$ is the fragmentation function (FF) for a parton of type c to produce a hadron of type h that carries the fraction z_c of the parton momentum. The scales μ_f and $\mu_{f'}$ are introduced to factorize initial and final-state collinear singularities into the scale dependent PDFs and FFs. The perturbatively calculable cross section for the hard scattering process $ab \to cX$, $\hat{\sigma}_{ab \to cX}(s,\alpha_s,x_a,x_b,z_c,\mu_f,\mu_r,\mu_{f'})$, depends on the collision energy $\sqrt{s}$, the strong coupling constant α_s, the momentum fractions of the partons and the produced hadron, as well as on the scale parameters μ_f, $\mu_{f'}$ and μ_r. μ_r denotes the energy scale at which α_s is being renormalized.

The different elements of the factorization of a hard scattering process are illustrated in Fig. 1.6. While hard scattering cross sections can be obtained from pQCD calculations, parton distribution functions and fragmentation functions have to be determined by measurements. Simplified, the factorized hadronic cross section can also be written as $\sigma^{pp \to hX} = \text{PDF} \otimes \text{pQCD} \otimes \text{FF}$.

Fragmentation functions can be derived from cross section measurements in $e^+ e^-$ collisions, where parton distribution functions don't play a role and the hadron production cross section can be factorized schematically as $\sigma^{e^+ e^- \to hX} = \text{pQED}/\text{pQCD} \otimes \text{FF}$.

Parton distribution functions are for example determined from cross section measurements in deep inelastic electron-proton scatterings. In the left panel of Fig. 1.7, PDFs for valence and sea quarks as well as for gluons at a squared momentum transfers $Q^2 = 10\,\text{GeV}^2$, obtained by fits to ZEUS data [20] are shown. Here, xf is the parton distribution function f, weighted with the momentum fraction x. For the PDFs, the following normalization applies: $\sum_i \int_0^1 xf_i(x,Q^2)\mathrm{d}x = 1$.

While at high parton momentum fraction x the proton momentum is mostly carried by the valence quarks, it is dominated by gluons for small x. With increasing resolution, the momentum carried by gluons at small x highly increases, as depicted in the right plot of Fig. 1.7.
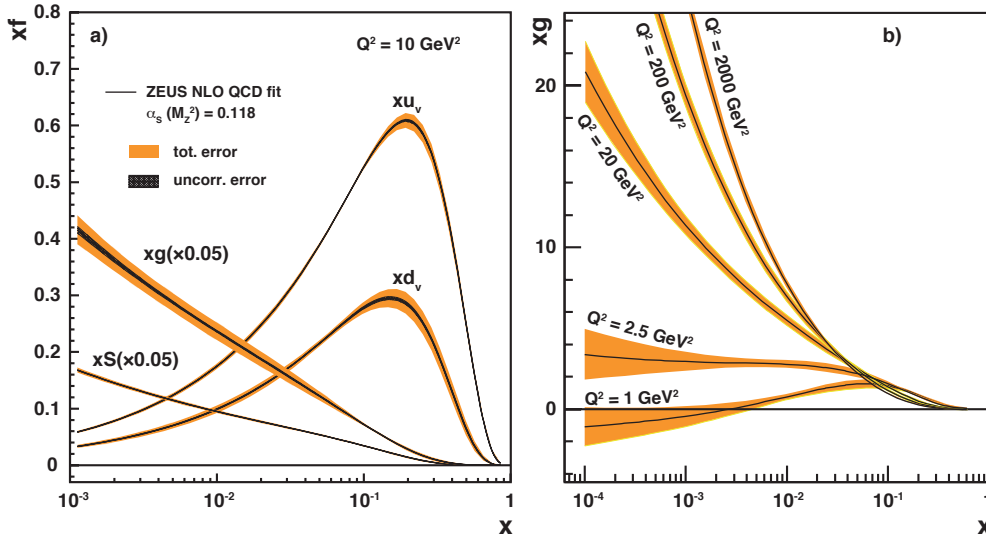

Figure 1.7: Left: Parton distribution functions for valence quarks, sea quarks and gluons, determined by the ZEUS experiment [20] at a squared momentum transfer $Q^2 = 10\,\text{GeV}^2$. Right. Gluon distributions for different Q^2. Figures taken from [15].

1.2   Cold Nuclear Matter Effects

In heavy-ion collisions, nuclear effects can lead to a modified particle production with respect to pp collisions. Even in the absence of hot nuclear matter effects, i.e. when a QGP is not created, the nuclear environment of the colliding nuclei can cause a modification. In p–Pb collisions, where the formation of a QGP is a priori not expected, these so-called cold nuclear matter (CNM) effects can be studied separately from hot nuclear matter effects. The measurement of particle production cross sections can help to study the partonic structure of the lead nucleus and to constrain nuclear parton density functions (nPDFs).

As described in Sec. 1.1.3, the distribution of partons inside the colliding nucleons affects the hadron production. It is observed that the partonic structure of nucleons inside a nucleus differ from that of the free proton [21]. These observations rule out the naive picture of the nucleus as a system of quasi-free nucleons.

The parton distribution function of a bound proton inside a nucleus with mass number A can be expressed as

$$ f_i^A(x,Q^2) = R_i^A(x,Q^2) f_i(x,Q^2) \, , \tag{1.6} $$

with $R_i^A(x,Q^2)$ being the nuclear modification with respect to the free proton PDF. Figure 1.8 shows a schematic illustration of $R_i^A(x,Q^2)$, indicating different regions of nuclear modification. Note that the limits of the regions depend on A and Q^2.

At large parton momentum fraction $x > 0.8$, $R_i^A(x,Q^2)$ exceeds unity. This indicates more scattering centers and thus an increased particle production in p–A or A–A collisions compared to pp. The increase in $R_i^A(x,Q^2)$ is due to the so-called "Fermi motion". Nucleons are not stationary within a nucleus, but move with a certain average momentum. This momentum smearing becomes most visible at large x where the parton distribution in the free proton quickly approaches zero and the parton basically carries the full nucleon's momentum.

For parton momentum fractions between approximately 0.2 and 0.8, $R_i^A(x,Q^2)$ is observed to be smaller than one. This EMC effect is named after the European Muon Collaboration (EMC) which first reported a modification in deep-inelastic muon-iron scatterings compared to muon-deuterium scatterings [23]. The origin of the suppression is not fully understood yet,
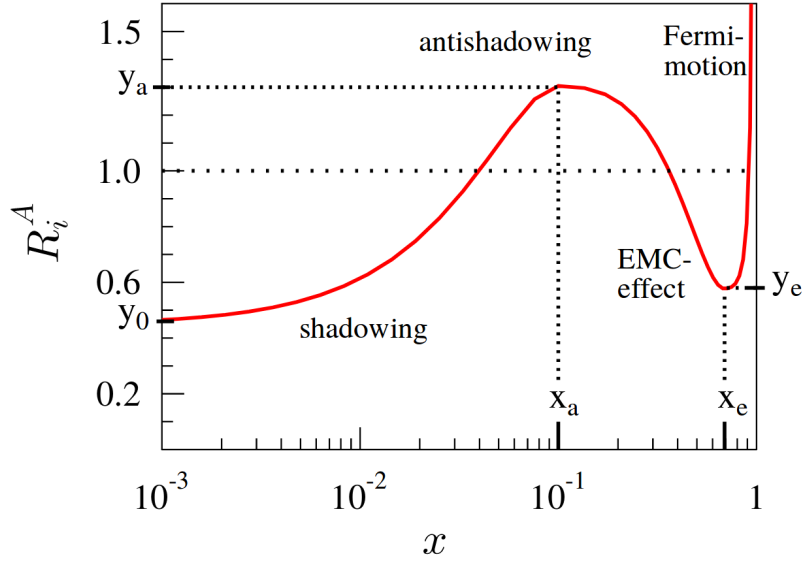
Figure 1.8: Schematic illustration of the nuclear modification $R_i^A(x,Q^2)$ as a function of momentum fraction x. [22]

but several theoretical approaches exist to explain the effect, for example by multiquark clusters or nuclear binding. See Ref. [24] for a detailed review of the EMC effect.

With further decreasing parton momentum fraction, $R_i^A(x,Q^2)$ first increases to values above unity and then decreases again. These regions are called anti-shadowing and shadowing. With p–Pb collisions at LHC energies, parton momentum fractions in the shadowing region are probed. The reason for the suppression at low x is not fully understood yet. One possible explanation on the partonic level is that partons with low x spread over a large longitudinal distance due to the uncertainty principle. Partons from different nucleons may thus occupy the same region in space and can interact and fuse, which leads to a depletion of partons in the shadowing region. Momentum conservation consequently leads to an increase of partons at larger x, the anti-shadowing [21].

Figure 1.9 shows a comparison of two recent nPDF analyses, EPPS16 [25] and nCTEQ15 [26]. Although the results agree within the large uncertainties, the mean values partially show a different trend, especially at low x. It becomes evident that in the region that is probed at the LHC[1], $10^{-4} < x < 10^{-2}$, the distributions aren't as well determined as for the free proton and that further measurements are needed to better constrain the nPDFs.

---

[1]x can be approximated by $x \approx \frac{p_T}{\sqrt{s}}e^{-y}$; $x \approx \frac{p_T}{\sqrt{s}}$ at midrapidity $y = 0$
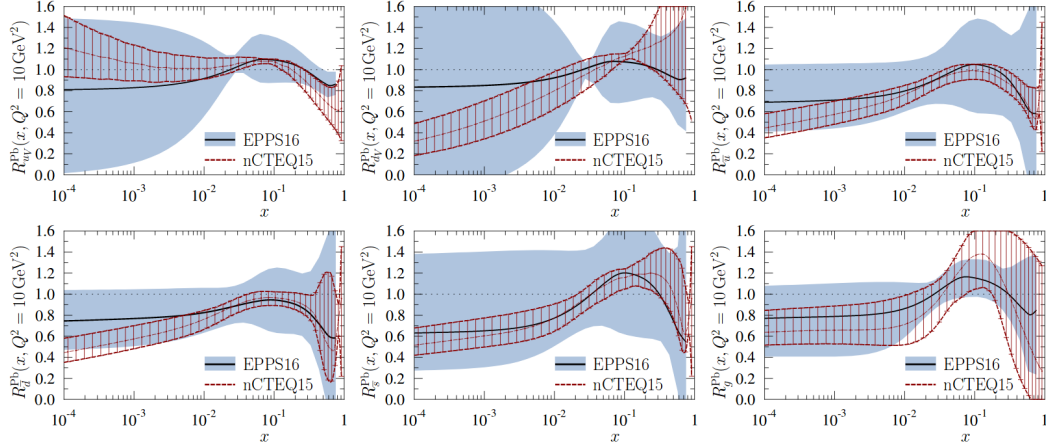
Figure 1.9: Comparison of two different nPDF analyses. In the upper panel, from left to right, the nuclear modification R^{Pb} is shown for valence u quarks, valence d quarks and ū quarks. In the lower panel R^{Pb} is given for d̄ and s̄ quarks and gluons. [25]

Another cold nuclear matter effect is the so-called Cronin-effect, which is the observation of an enhanced particle production at intermediate p_{T} ($\approx 2 - 4\,\text{GeV}/c$). It was first reported by Cronin *et al.* in 1975 [27] for hadron production in fixed-target p–A collisions at incident proton energies of $200 - 400\,\text{GeV}$. While the effect is not fully understood, a possible explanation are multiple soft scatterings of the proton that lead to an enhancement of the average particle momentum. However, in p–Pb collisions at $\sqrt{s_{\text{NN}}} = 5.02\,\text{TeV}$, an enhancement in the Cronin region is reported for the production of protons, but not for lighter hadrons [28]. This contradicts multiple scattering in the initial state and is more likely to be caused by a final state interaction.

In the context of p–Pb collisions at the LHC also the Color Glass Condensate (CGC) may play an important role. The CGC is an effective theory that describes the gluon content of hadrons and nuclei in high energy collisions [29]. The nucleons consist of three valence quarks and additional short lived fluctuations into gluons and quark-antiquark pairs. At low energies, interactions between the constituents during the collision have to be considered. At high energies, however, the situation changes. Due to relativistic kinematics, the colliding nucleons are Lorentz contracted and appear nearly two-dimensional in the laboratory frame. In addition, the time scale of the fluctuations and the interactions of the constituents inside the nucleons is dilated. The time dilation leads to two effects: the constituents can be regarded as free during the collision and more of the fluctuations, at

low x mainly gluons, are visible in the nucleons. This leads to the increase of gluon distributions for decreasing x also in the free proton, see Fig. 1.7. However, the gluon distributions are not expected to increase to infinity, otherwise, unitarity of QCD would be violated. At a saturation scale Q_s, where the gluon densities are sufficiently high, gluon recombination could lead to a saturation of the growths of gluon PDFs.

The regime of high parton densities is non-perturbative, even if the coupling is weak, and cannot be treated in pQCD calculations. In this saturation regime, QCD can be approximated by the CGC. The effective degrees of freedom in this framework are the valence quarks as color sources at large x and the gluon gauge fields at small x, treated as classical fields [30]. Due to the time dilation, the color sources appear as frozen and randomly distributed at the short time scale of small x gluons. The name "color glass" refers to the stochastic nature and the individual behavior at different time scales, as known from silica. "Condensate" refers to the high gluon densities that are especially achieved in highly Lorentz contracted heavy ions.

1.3 The Pseudoscalar Mesons

Particles which are composed of quarks and bound by the strong interaction are called hadrons. They are categorized into two groups: Baryons, composed of three quarks, and mesons, which are composed of a quark and an anti-quark. Protons and neutrons, which form our ordinary matter, belong to the group of baryons. The π^0 and the η that are reconstructed in the presented analysis are mesons.

All mesons are unstable and decay into photons or leptons, either directly or via the decay into lighter mesons. As quarks are fermions with half-integer spin, mesons are bosons with integer spin S. It can be 0 for anti-parallel quark spins ($\downarrow\uparrow$) or 1 for parallel quark spins ($\uparrow\uparrow$). In the lowest state with an orbital angular momentum $l = 0$ and without any radial excitation the total angular momentum J can be either $J = 0$ or $J = 1$. For mesons, the parity P is related to the orbital angular momentum and is given by $P = (-1)^{l+1}$. Consequently, the parity is negative for the lowest states with $l = 0$.

Mesons are grouped into multiplets, according to their quantum numbers J and P. Mesons with $J^P = 0^-$ are called pseudoscalar mesons, mesons with $J^P = 1^-$ are vector mesons. The name pseudoscalar is in contrast to a real scalar for which a positive parity is required. Table 1.1 gives an overview of different mesons categories with their corresponding quantum numbers.

Meson Type	S	l	P	J	J^P
Pseudoscalar Meson	0	0	-	0	0^-
Pseudovector Meson	0; 1	1	+	1	1^+
Vector Meson	1	0; 2	-	1	1^-
Scalar Meson	1	1	+	0	0^+
Tensor Meson	1	1; 3	+	2	2^+

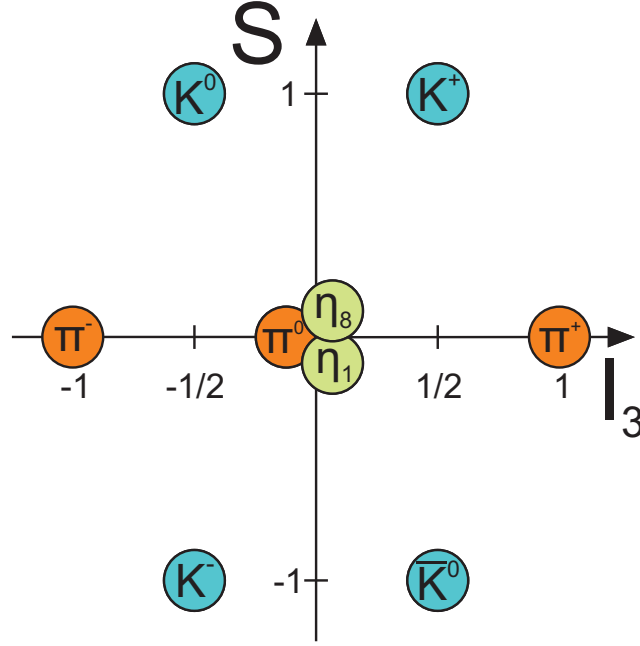Table 1.1: Meson categories with corresponding quantum numbers.

Figure 1.10: Pseudoscalar meson nonet as a function of the strangeness S and the third component of the isospin vector I_3.

The combination of the six different quarks and corresponding antiquarks leads to $6 \times 6 = 36$ different possibilities to form a meson. If the number of quarks is constrained to the three lightest flavors - up, down and strange - $3 \times 3 = 9$ combinations are possible. Or, if regarded as special unitary group $SU(3)_F$ (with F for flavor) $3 \otimes 3 = 8 \oplus 1$, building an octet plus a singlet state, together a nonet. The nonet of the light pseudoscalar mesons is shown in Fig. 1.10, plotted as a function of the strangeness S and the third component of the isospin vector, I_3. The quark content of the pseudoscalar mesons is listed in Table 1.2.

The six $q\bar{q}$ states located at the corners of the meson multiplet can be directly assigned to the respective mesons, the kaons and the charged pions. For the three different states $|u\bar{u}\rangle$, $|d\bar{d}\rangle$ and $|s\bar{s}\rangle$ at the center this is however not easily possible. Due to their accordance in strangeness S and in I_3, as well as in J^P, theses states can mix.

The singlet state which has to be completely symmetrical can be constructed as follows:

$$|\eta_1\rangle = \frac{1}{\sqrt{3}} |u\bar{u} + d\bar{d} + s\bar{s}\rangle \qquad (1.7)$$

	I	I_3	S	Meson	Quark Content
	1	1	0	π^+	$u\bar{d}$
	1	-1	0	π^-	$d\bar{u}$
	1	0	0	π^0	$(d\bar{d} - u\bar{u})/\sqrt{2}$
Octet	$\frac{1}{2}$	$\frac{1}{2}$	+1	K^+	$u\bar{s}$
	$\frac{1}{2}$	$-\frac{1}{2}$	+1	K^0	$d\bar{s}$
	$\frac{1}{2}$	$-\frac{1}{2}$	-1	K^-	$s\bar{u}$
	$\frac{1}{2}$	$\frac{1}{2}$	-1	$\bar{K}^0$	$s\bar{d}$
	0	0	0	η_8	$(d\bar{d} + u\bar{u} - 2s\bar{s})/\sqrt{6}$
Singlet	0	0	0	η_1	$(d\bar{d} + u\bar{u} + s\bar{s})/\sqrt{3}$

Table 1.2: Quark content and quantum numbers of the pseudoscalar mesons. [31]

The two remaining states at the multiplet center have to belong to the $SU(3)_F$-octet. The third component of the isospin for the charged pions π^+ and π^- is $I_3 = +1$ and $I_3 = -1$, respectively. They both belong to the isospin triplet with $I = 1$. The neutral component of this triplet with $I_3 = 0$ is the π^0:

$$|\pi^0\rangle = \frac{1}{\sqrt{2}} |u\bar{u} - d\bar{d}\rangle \tag{1.8}$$

As the third state has to be orthogonal to the singlet state η_1 as well as to the π^0, the following octet state is obtained:

$$|\eta_8\rangle = \frac{1}{\sqrt{6}} |u\bar{u} + d\bar{d} - 2 \times s\bar{s}\rangle \tag{1.9}$$

For an ideal $SU(3)_F$ symmetry, same masses of the up, down and strange quarks are required. While the mass difference between up an down quark is small, which makes it possible to treat them like an isospin doublet, the strange quark is much heavier. Estimates for the current-quark masses are $m_u = 2.2^{+0.6}_{-0.4}$ MeV, $m_d = 4.7^{+0.5}_{-0.4}$ MeV and $m_s = 96^{+8}_{-4}$ MeV [13]. This mass difference is responsible for the breaking of the $SU(3)_F$ symmetry, which causes that the $SU(3)_F$ states η_1 and η_8 are not identical with the physical

particles named η and η'. The latter are linear combinations of the SU(3)$_F$ states with the mixing angle θ:

$$|\eta\rangle = \cos \theta |\eta_8\rangle - \sin \theta |\eta_1\rangle$$
$$|\eta'\rangle = \sin \theta |\eta_8\rangle + \cos \theta |\eta_1\rangle \qquad (1.10)$$

The octet-singlet mixing angle has been determined in multiple ways in various experiments and calculations. It is found to be between -13° and -20° [32].

A mixing of the π^0 with the η and η' is at first order not allowed due to the different isospin I. But as the isospin symmetry is also slightly broken in the strong interaction due to the slightly different u and d masses (but much less than the SU(3)$_F$ symmetry), also small η and η' contributions to the π^0 could be possible [33]. Admixtures of the pseudoscalar meson η_c with the quark content $|c\bar{c}\rangle$ are suppressed due to the large mass differences between strange and charm quark.

The main properties of pseudoscalar mesons like mass and mean life time are listed in Table 1.3. Common decay modes with branching ratios above 5% are also given. For the charged pions and kaons the decay modes are only given for the positively charged particle. The negative mesons decay analogously into the corresponding anti-particles.

The neutral kaons K^0 and $\bar{K}^0$ are created as strong eigenstates with well defined strangeness $S \neq 0$. As they are the lightest mesons that carry open strangeness, they cannot decay via the strong interaction due to strangeness conservation. In the weak interaction, however, strangeness is not a conserved quantity. The weak eigenstates K^0_S and and K^0_L are linear combinations of the strong eigenstates K^0 and $\bar{K}^0$ with undefined strangeness, as they are no strange eigenstates, but defined lifetime and branching ratios, which can be found in Table 1.3. The K^0 and $\bar{K}^0$ both have a probability of 50% each to appear as a K^0_S or a K^0_L. The K^0_S can decay into two pions, which is forbidden for the K^0_L for the reason of charge parity (*CP*) conservation. The phase space is larger for the two pion decay compared to the three pion decay mode of the K^0_L, which is reflected in the mean life times and the naming of the particles with S for short and L for long.

However, the *CP* violating decay $K^0_L \rightarrow \pi^+\pi^-$ exists with a small branching ratio of 0.1967% [13] and was first measured in 1964 [34].

Meson	Mass m (MeV/c^2)	Mean Life Time τ (s)	$c\tau$ (m)	Common Decays
π^0	134.98	8.52×10^{-17}	25.5×10^{-9}	$\gamma\gamma$ (98.82%)
$\pi^\pm$	139.57	2.60×10^{-8}	7.80	$\mu^+\nu_\mu$ (99.99%)
$K^\pm$	493.68	1.24×10^{-8}	3.71	$\mu^+\bar{\nu}_\mu$ (63.55%)
				$\pi^0 e^+\nu_e$ (5.07%)
				$\pi^+\pi^0$ (20.66%)
				$\pi^+\pi^+\pi^+$ (5.59%)
K_S^0	497.61	8.95×10^{-11}	2.68×10^{-2}	$\pi^0\pi^0$ (30.69%)
				$\pi^+\pi^-$ (69.20%)
K_L^0	497.61	5.12×10^{-8}	15.34	$\pi^\pm e^\mp\nu_e$ (40.55%)
				$\pi^\pm\mu^\mp\nu_\mu$ (27.04%)
				$\pi^0\pi^0\pi^0$ (19.52%)
				$\pi^+\pi^-\pi^0$ (12.52%)
η	547.86	5.02×10^{-19}	0.15×10^{-9}	$\gamma\gamma$ (39.41%)
				$\pi^0\pi^0\pi^0$ (32.68%)
				$\pi^+\pi^-\pi^0$ (22.92%)
η'	957.78	3.32×10^{-21}	0.96×10^{-12}	$\pi^+\pi^-\eta$ (42.9%)
				$\rho^0\gamma$ (29.1%)
				$\pi^0\pi^0\eta$ (22.2%)

Table 1.3: Different properties of the pseudoscalar mesons. [13]

1.4   Photon Conversions

If a photon beam with an initial intensity I_0 traverses matter, the attenuation is exponential with the thickness of the absorbing medium [13]:

$$I(x) = I_0 \cdot e^{-x/\lambda} \tag{1.11}$$

Here, x is thickness (in mass/unit area) and λ the photon mass attenuation length or absorption length. The attenuation length λ can also be written as $\lambda = 1/(\mu/\rho)$, with μ/ρ as mass attenuation coefficient and ρ as density.
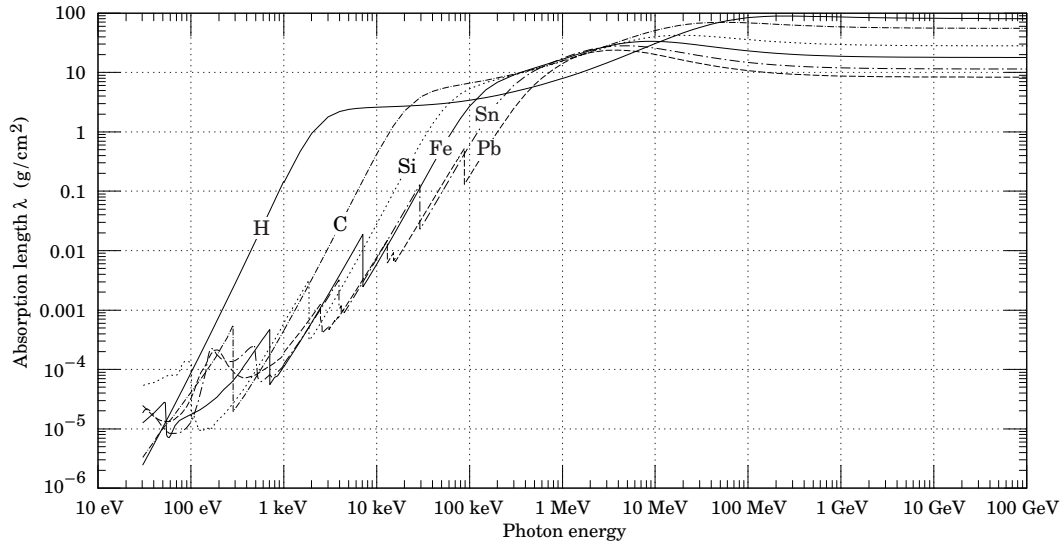

Figure 1.11: The photon mass attenuation length λ as a function of photon energy for various elemental absorbers. [13]

Figure 1.11 shows the attenuation length λ for various elemental absorbers as a function of photon energy. In the photon energy range above 100 MeV, which is relevant for the presented analysis, λ is nearly constant. For a chemical compound of different elements, the effective attenuation length λ_{eff} can be calculated via [13]:

$$\frac{1}{\lambda_{\text{eff}}} = \sum_{\text{elements}} \frac{w_Z}{\lambda_Z} \, , \tag{1.12}$$

where w_Z is the proportion by weight of the chemical element with the atomic number Z.
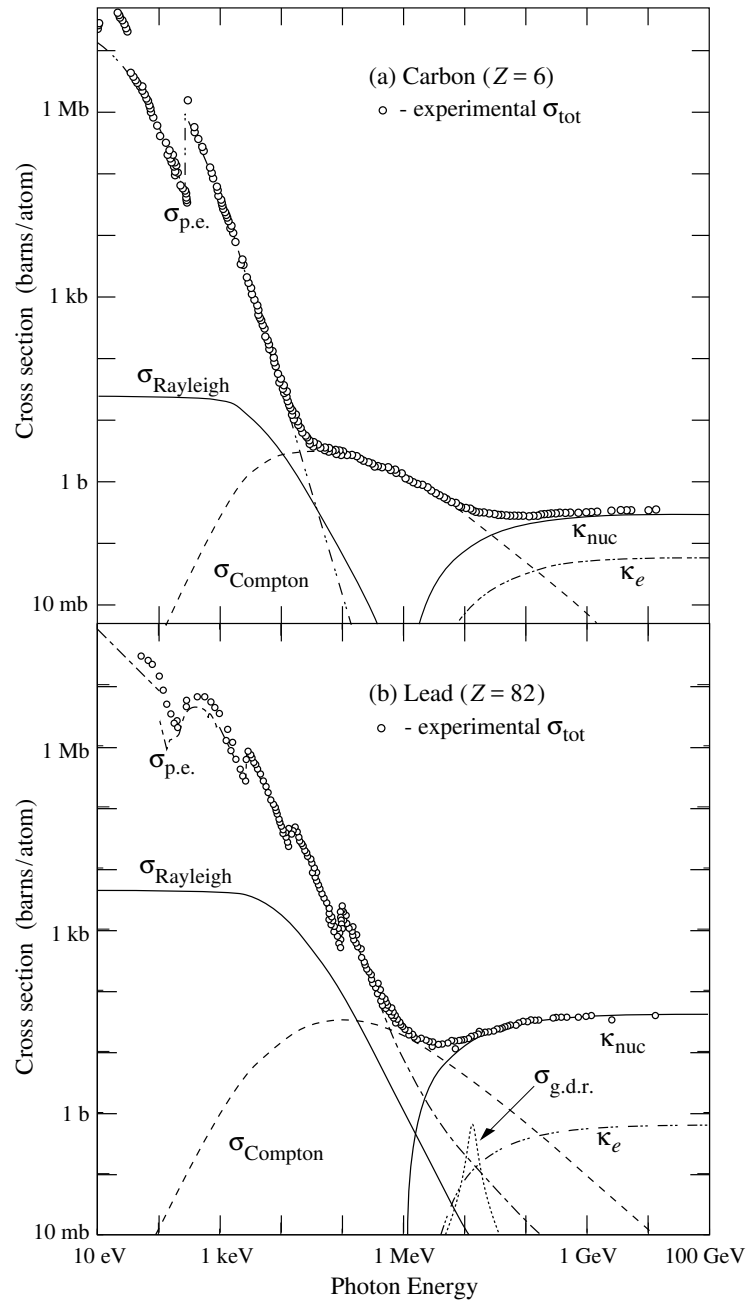
Figure 1.12: Photon total cross section as a function of photon energy in carbon and lead, with the following contributions [13]:

$\sigma_{p.e.}$ = atomic photoelectric effect;

$\sigma_{Rayleigh}$ = coherent Rayleigh scattering;

$\sigma_{Compton}$ = incoherent Compton scattering;

κ_{nuc} = pair production in the nuclear field;

κ_e = pair production in the field of an electron;

$\sigma_{g.d.r.}$ = photonuclear interactions (especially Giant Dipole Resonance)

Different processes lead to the attenuation of photons in matter. The most important ones are:

- Photoelectric effect

- Compton scattering

- Pair production

Figure 1.12 shows the photon cross section as a function of photon energy in carbon and lead. In addition to the total cross section, also the contributions of different interaction processes are presented. The total cross section σ is connected to the mass attenuation coefficient via the following relation [35]:

$$\frac{\mu}{\rho} = \frac{\sigma \cdot N_0}{A} \tag{1.13}$$

Here, N_0 is the Avogadro constant and A the molar mass of the traversed medium.

For small photon energies, the total photon cross section is dominated by the photoelectric effect, while for intermediate energies of about 0.5 to 5 MeV Compton scattering becomes the most important interaction process. At higher energies, pair production, also known as photon conversion, is the predominant process and will be described in more detail in the following paragraphs. The probability that a photon interaction results in a conversion is presented in Fig. 1.13 as a function of the photon energy for several materials.

Pair production is the emission of an electron-positron pair as a result of the absorption of a photon in the Coulomb field of an atomic nucleus or an electron.

$$\gamma + A \rightarrow e^+ e^- + A \tag{1.14}$$

Often, the short notation $\gamma \rightarrow e^+ e^-$ is used.

If the conversion takes place in the field of a nucleus, the latter receives some recoil. The energy threshold for this process is [36]:

$$E_\gamma \geq 2\,m_e c^2 + 2\frac{m_e^2}{m_{\text{nucleus}}}c^2 \tag{1.15}$$
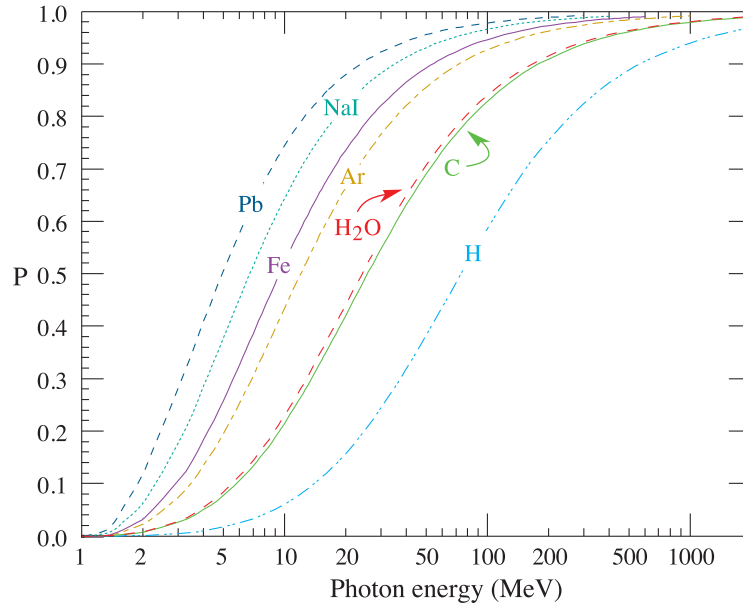
Figure 1.13: Probability P that a photon interaction results in the creation of an e^+e^- pair as function of the photon energy for different materials. [13]

As the recoil of the nucleus is often negligible, the energy threshold is approximately twice the electron rest mass, $2\,m_e c^2$. The necessity of a recoil partner becomes obvious in the limit $E_\gamma = 2\,m_e c^2$, where the leptons would be created without kinetic energy or momentum. As the momentum of the photon $\hbar k = E/c$ cannot be zero, momentum conservation cannot be fulfilled without the presence of another particle. Thus, pair production cannot take place in vacuum and the respective cross section strongly depends on the surrounding medium.

A characteristic quantity to describe the traversed medium is the radiation length X_0 that is related to the energy loss of high energy electrons and photons inside the material. It is defined as the mean distance over which a high energy electron loses all but $1/e$ of its energy by Bremsstrahlung and as $7/9$ of the mean free path for pair production by a high-energy photon [13]. X_0 can be expressed as [37]:

$$\frac{1}{X_0} = 4\alpha\,r_e^2\frac{N_A}{A}\left\{Z^2\left[L_{\text{rad}} - f(Z)\right] + ZL'_{\text{rad}}\right\} \tag{1.16}$$

Here, $A = 1\text{ g mol}^{-1}$ and $4\alpha\,r_e^2\frac{N_A}{A} = (716.408\text{ g cm}^{-2})^{-1}$. Values for L_{rad} and L'_{rad} for different elements can be found in Table 1.4. The function $f(Z)$ is an

23

infinite sum, which can be represented for elements up to uranium to 4-digit accuracy by [38]

$$f(Z) = a^2[(1 + a^2)^{-1} + 0.20206 - 0.0369\,a^2 + 0.0083\,a^4 - 0.002\,a^6]\,, \quad (1.17)$$

with $a = \alpha Z$.

Some typical radiation lengths for different materials, for example the counting gas of the ALICE TPC, are listed in Table 1.5.

With the use of the radiation length, the differential photon cross section for pair production at high photon energies can be approximated as [37]:

$$\frac{d\sigma_p}{dx} = \frac{A}{X_0 N_A}\left[1 - \frac{4}{3}x(1-x)\right] \quad (1.18)$$

Here, $x = E/k$ is the fractional energy transfer to the produced electron or positron and k the incident photon energy. At high photon energies, the cross section becomes basically constant with the high energy limit

$$\sigma_p = \frac{7}{9}\frac{A}{X_0 N_A}, \quad (1.19)$$

which is still accurate within a few percent for photon energies down to $1\,\text{GeV}$, particularly for high-Z materials [37].

Element	Z	L_{rad}	L'_{rad}
H	1	5.31	6.144
He	2	4.79	5.621
Li	3	4.74	5.805
Be	4	4.71	5.924
Others	>4	$\ln(184.15\,Z^{-1/3})$	$\ln(1194\,Z^{-2/3})$

Table 1.4: L_{rad} and L'_{rad} for different elements for the calculation of the radiation length X_0. [37]

Material	Radiation Length X_0 (g cm^{-2})
Al	24.01
Si	21.82
Fe	13.84
Ne	28.93
CO_2	36.20
$NeCO_2$ (90%/10%)	30.11
$PbWO_4$	7.39

Table 1.5: Radiation length for different materials, for example the ALICE TPC counting gas mixture $NeCO_2$. Values taken from [13].

Another representation elucidates the energy and material dependence of the photon cross section for pair production [8]:

$$\begin{aligned} \sigma_p &\sim Z^2 \ln(E_\gamma) \quad \text{for} \quad 5\, m_e c^2 < E_\gamma < 50\, m_e c^2 \\ \sigma_p &\cong 12\alpha\, Z^2 r_e^2 \quad \text{for} \quad E_\gamma > 10^3\, m_e c^2 \end{aligned} \tag{1.20}$$

If the conversion takes place in the Coulomb field of a shell electron, the latter is accelerated due to the recoil and kicked out of the atom. The kinetic energy is shared between the three particles, the two electrons and one positron. The energy threshold for this case is $E_\gamma = 4\, m_e c^2$, thus twice the threshold for the conversion in a Coulomb field of a nucleus. Due to the strong Z-dependence of the photon cross section, the cross section for the conversion in the field of a shell electron is one to three orders of magnitude smaller compared to the conversion in the field of a nucleus, see also Fig. 1.12.

Chapter 2

ALICE at the LHC

2.1 The Large Hadron Collider - LHC

The Large Hadron Collider at CERN is the world's largest and most powerful hadron accelerator [39]. Installed in the former LEP [40] tunnel with a circumference of 26.7 km, the LHC is designed to collide protons with a center-of-mass energy of up to 14 TeV and a luminosity of 10^{34} cm^{-2}s^{-1}, while heavy lead ions can be collided with 2.8 TeV per nucleon pair and a luminosity of 10^{27} cm^{-2}s^{-1}.

Protons and lead ions are pre-accelerated in several stages within the CERN accelerator complex as it can be seen in Fig. 2.1 [41]. The first acceleration stages of the protons are the linear accelerator LINAC 2 and the BOOSTER, whereas the heavy ions are accelerated in LINAC 3 and the low energy ion ring LEIR. The proton synchrotron PS and the super proton synchrotron SPS are the two last stages for both protons and lead ions before the injection into the LHC. Inside the LHC the hadrons circulate as bunches clock- and counter-clockwise in two beam pipes that are merged to one common pipe in the interaction regions where the four large LHC experiments are located. Superconducting magnets which are operated with liquid helium at 1.9 K and which produce a magnetic field of up to 8.3 T are used to maintain the hadrons on the proper trajectory. 2808 proton bunches with approximately 100 billion protons per bunch can be accelerated per beam. In the case of Pb ions, 592 bunches per beam with an occupancy of about 70 million ions per bunch are possible.

The collisions at the interaction points are recorded by the four LHC experiments: ATLAS [42], CMS [43], LHCb [44], and ALICE [45]. ATLAS and CMS are the multi-purpose particle detectors at the LHC. Their aim is to

study a wide range of physics, including the searches for the Higgs boson, Super Symmetry and Dark Matter. Their most well known achievement so far has been the actual discovery of the predicted standard model Higgs boson in 2012 [46][47]. LHCb is specialized for the investigation of CP violation in beauty decays. The ALICE detector, which will be described in more detail in the following section, is the only dedicated heavy-ion experiment at CERN, focusing on the study of the Quark-Gluon Plasma (QGP).

So far, the ALICE experiment has recorded pp, Pb–Pb, and p–Pb collisions at different energies, ranging from $\sqrt{s} = 0.9$ TeV up to $\sqrt{s} = 13$ TeV for pp collisions and from $\sqrt{s_{\mathrm{NN}}} = 2.76$ TeV to $\sqrt{s_{\mathrm{NN}}} = 5.02$ TeV for Pb–Pb collisions. The data sample that has been analyzed within the scope of this thesis was taken in p–Pb collisions at $\sqrt{s_{\mathrm{NN}}} = 5.02$ TeV in January 2013.

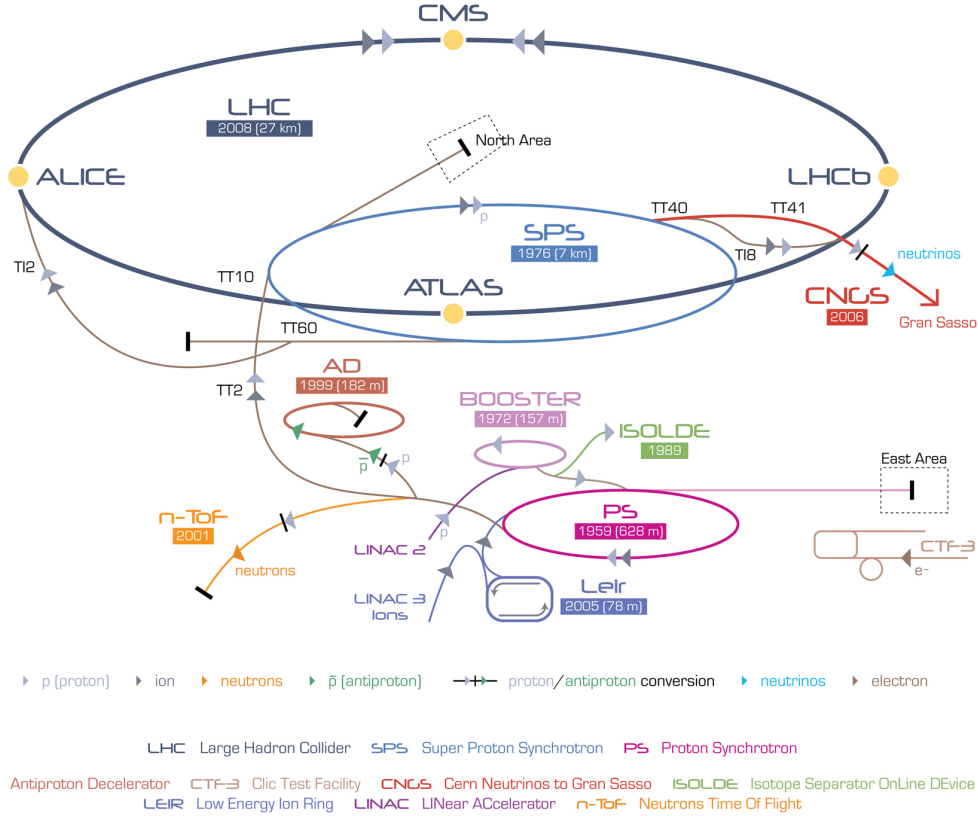Figure 2.1: Schematic view of the CERN accelerator complex. The first acceleration stages of the proton are the linear accelerator LINAC 2 and the BOOSTER, whereas the heavy ions are accelerated in LINAC 3 and the low energy ion ring LEIR. Afterwards, protons and lead ions are further pre-accelerated by the proton synchrotron PS and the super proton synchrotron SPS before being injected into the LHC. [48]
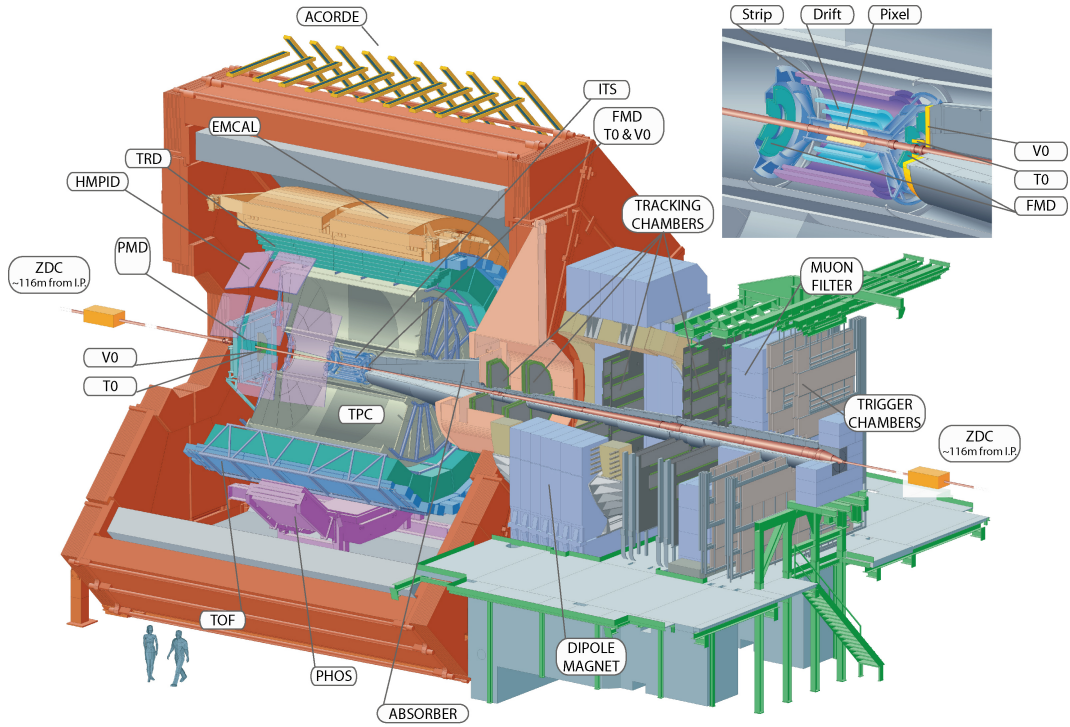
Figure 2.2: Schematic view of the ALICE detector. [49]

2.2   A Large Ion Collider Experiment - ALICE

The ALICE detector (Fig. 2.2) is a general-purpose heavy-ion detector at the LHC which focuses on the investigation of the Quark-Gluon Plasma in Pb–Pb collisions. In addition, also data from pp and p–Pb collisions is recorded and analyzed with ALICE, which serves as reference for Pb–Pb collisions on the one hand and allows for the study of QCD phenomena in smaller nuclear systems, presumably without the creation of a hot and dense matter on the other hand.

ALICE involves an international collaboration of more than 1500 physicists, engineers and technicians from more than 150 institutes in 37 countries across the world. The ALICE setup consists of 18 subdetectors which are mostly arranged in the central barrel, located around the interaction point inside the L3 solenoid [50], and the muon arm at forward rapidity. An illustration of the ALICE coordinate system is presented in Fig. 2.3. The origin is locate at the nominal interaction point in the middle of the central barrel. The x-axis runs horizontally from the interaction point towards the center of the LHC. The z-axis is perpendicular to x and parallel to the

beam line with the so-called A side defining the positive direction. The y-axis is perpendicular to x and z and points upwards. In p–Pb collisions, positive rapidity and pseudorapidity are defined in the direction of the proton beam, which means in direction of the muon arm. It has to be noted that this definition was introduced for p–Pb collisions and that earlier ALICE publications and technical design reports define positive rapidity for the positive z-direction.

As ALICE has to handle extreme numbers of particles produced in central heavy-ion collisions, the subsystems are optimized to provide a high momentum resolution and a precise particle identification (PID) over a large transverse momentum range also at highest multiplicities. The subsystems that have been used for the presented analysis are described in further detail in the following subsections.
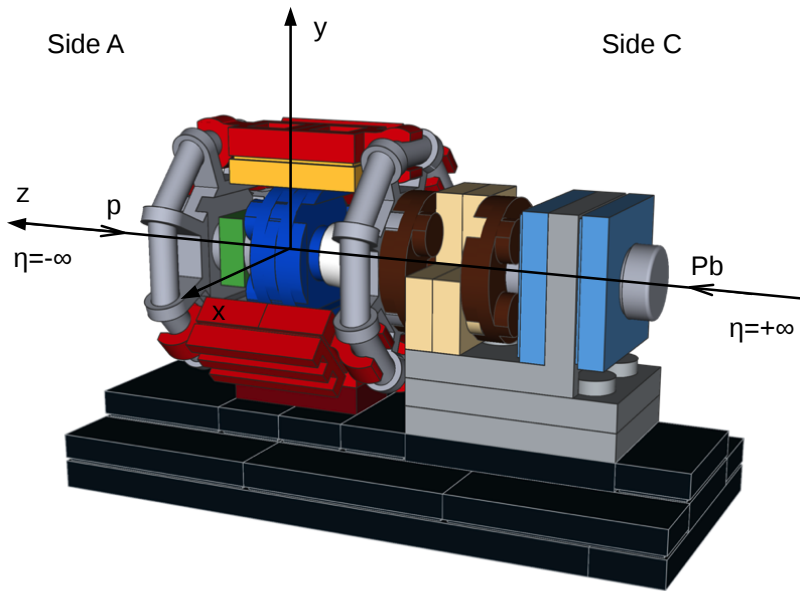
Figure 2.3: Illustration of the ALICE coordinate system. Modified from [51].

2.2.1 The Inner Tracking System - ITS

The ITS [52] is the innermost ALICE detector consisting of six layers of silicon detectors. Its main purpose is to reconstruct the primary vertex of the collision and secondary vertices from B and D meson decays with a resolution better than 100 μm. Therefore, the ITS is located directly around the beam pipe covering full azimuth. The two innermost layers are built

of Silicon Pixel Detectors (SPD) positioned at a radial distance of 4 and 7 cm, respectively. With cells of 50 x 300 μm^2, the two SPD layers have the highest granularity of the ITS in order to cope with about 50 particles per cm^2 produced in central heavy-ion collisions. The two SPD layers cover a pseudorapidity range in the laboratory system of $|\eta_{\text{lab}}| < 2$ and $|\eta_{\text{lab}}| < 1.4$, respectively. All subsequent ITS layers cover $|\eta_{\text{lab}}| < 0.9$ in pseudorapidity. The next two layers consist of Silicon Drift Detectors (SDD) at 15 and 23.9 cm radial distance to the interaction point, followed by double-sided Silicon micro-Strip Detectors (SSD) as the outermost two ITS layers at 38 and 43 cm.

Besides the precise vertex reconstruction, another main task of the ITS is to track particles with momenta below 200 MeV/c. In this way, momentum and angular resolution for particles reconstructed by the Time-Projection Chamber (see 2.2.2) can be improved and even particles traversing dead regions of the TPC can be reconstructed. As the SDD and the SSD are read out analogously they can be used for particle identification (PID) via dE/dx measurement in the non-relativistic region. This makes it possible to identify particles even with transverse momenta down to about 80 MeV/c.

2.2.2 The Time Projection Chamber - TPC

The TPC [53] is, together with the ITS, the main tracking device of ALICE. It is a cylindrical drift detector with a gas volume of nearly 90 m^3 which makes it the world largest TPC. It covers a pseudorapidity range of $|\eta_{\text{lab}}| < 0.9$ over the full azimuthal angle for the maximum track length of 159 reconstructed space points. The ALICE TPC is designed to handle even highest rapidity densities approaching dN_{ch}/dy = 8 000 in Pb–Pb collisions which translates to a total amount of up to 20 000 tracks in the active volume. A three dimensional sketch of the TPC field cage is shown in Fig. 2.4.

The TPC surrounds the ITS and its axis is aligned to the LHC beams and parallel to the solenoidal magnetic field of the L3 magnet. The active volume of the TPC ranges from 85 cm to 250 cm in the radial direction and has an overall length of 500 cm. The gas volume is divided into two symmetric drift volumes by the central HV electrode located at the axial center and aligned to the nominal interaction point. The central electrode is at a potential of 100 kV. Together with a voltage dividing network at the surface of the outer and inner cylinder, it creates a highly uniform axial electric field of 400 V/cm. This high drift field is required to keep the drift time of the TPC short and allow for the maximum interaction rate of 8 kHz for Pb–Pb collisions.
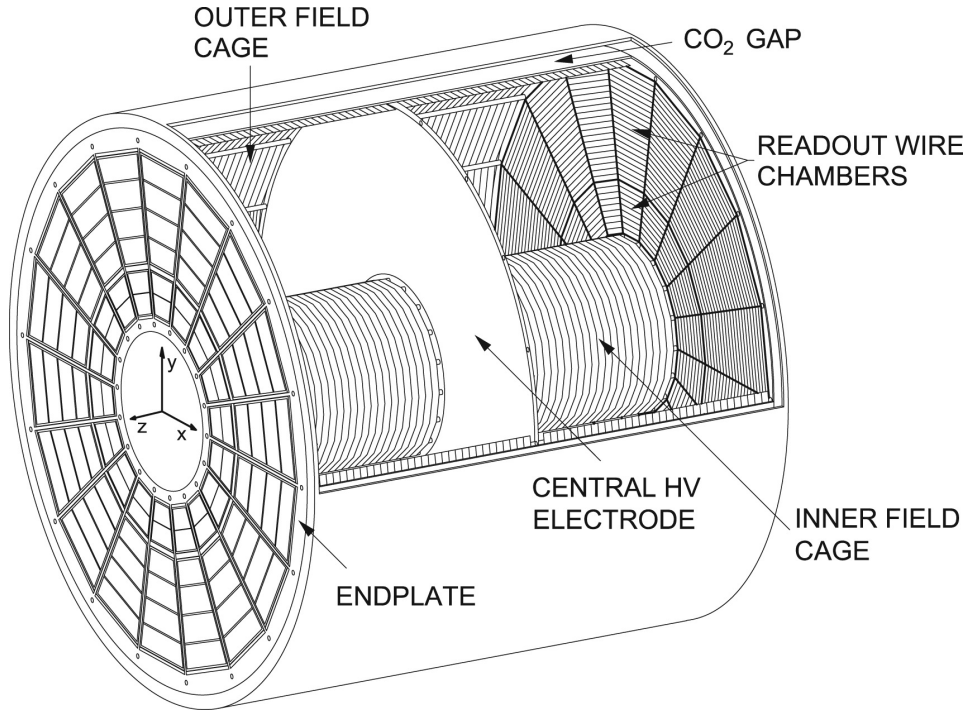
Figure 2.4: 3D sketch of the TPC field cage with the high voltage electrode located at the center and the end-plates equipped with 36 read-out chambers. [53]

The TPC is filled with a counting gas (Ne-CO_2 during the p-Pb data taking period) at atmospheric pressure. Charged tracks that cross the TPC volume ionize the counting gas along their path. The created electrons drift towards the TPC end-plates which are equipped with multi-wire proportional chambers (MWPCs) with cathode readout. The two end-plates are divided into 18 trapezoidal sectors, each covering 20° in azimuth. In radial direction the sectors are segmented into Inner and Outer Read-Out Chambers (IROC and OROC). This segmentation is needed as the radial dependence of the track density leads to different requirements at small and large radii. While the pads of the IROCs have a size of $4 \times 7.5 \, \text{mm}^2$ ($r\varphi \times r$), two different pad versions with the size of $6 \times 10 \, \text{mm}^2$ and $6 \times 15 \, \text{mm}^2$($r\varphi \times r$), respectively, are used for the OROCs. In total, the TPC end plates are equipped with 557 568 read out channels which allow for a precise measurement of the arrival point of the electrons. Together with an accurate determination of the arrival time this gives a precise three dimensional measurement of the charged particle trajectories. The charged particle momenta are determined from the curvature of the tracks in the magnetic field of the L3 magnet. The

best resolution is achieved for transverse momenta of about $1\,\mathrm{GeV}/c$. Here, $\sigma_{p_\mathrm{T}}/p_\mathrm{T}$ is better than 1%. With increasing p_T, the track curvature decreases, which leads to a linear worsening of the resolution. At $100\,\mathrm{GeV}/c$ the p_T resolution is about 10%.
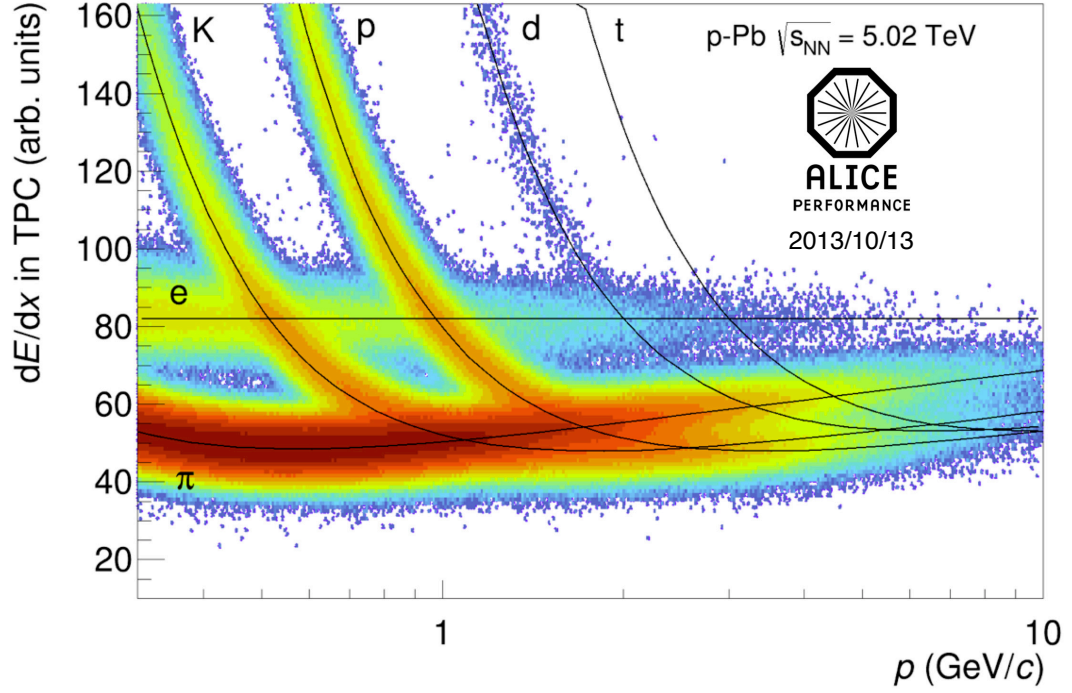
Figure 2.5: TPC ionization signal ($\mathrm{d}E/\mathrm{d}x$) versus the momentum p for charged tracks measured in p–Pb collisions. The black lines represent Bethe-Bloch parametrizations for the given particle species. [49]

Besides the tracking capabilities, the TPC also provides particle identification via the specific energy loss $\mathrm{d}E/\mathrm{d}x$, as presented in Fig. 2.5. The resolution in the ionization signal is 5% for tracks with the maximum number of space points.

2.2.3 The Electromagnetic Calorimeters - PHOS and EMCal

Two electromagnetic calorimeters are installed in the ALICE setup: the Photon Spectrometer PHOS and the Electromagnetic Calorimeter EMCal. The calorimeters were not used for the presented neutral meson analysis via photon conversions, but are included in the combined ALICE measurement described in Sec. 4.2.

PHOS

The Photon Spectrometer PHOS [54] is a lead tungstate ($PbWO_4$) electro-magnetic calorimeter with a fine granularity that measures the energy and hit coordinates of photons and electrons. Neutral mesons, π^0 and η, can be measured via their two photon decay channels. During the LHC Run1 data taking PHOS consisted of three detector modules mounted at a radial distance of 4.6 m from the ALICE interaction point and covering $|\eta_{lab}| < 0.12$ in pseudorapidity and $260° < \varphi < 320°$ in azimuth. Each module has 3584 detection channels in a matrix of 64×56 cells.

Lead tungstate crystals have been chosen as detector material as their small Molière radius and the high density match the requirements imposed by the high multiplicity environment in central Pb–Pb collisions. The highest rapidity densities of $dN/dy = 8\,000$ lead to approximately $16\,000$ clusters per rapidity interval when counting the decay photons of the π^0 rather than the π^0's themselves. In order to resolve overlapping showers a high segmentation at the order of the Molière radius and a large distance to the interaction point is needed in addition. In this way, a transverse cell size of 2.2×2.2 cm was chosen. The cell length of 18 cm which corresponds to 20 radiation lengths is a reasonable compromise between detector performance and production costs. The crystals are coupled to Avalanche Photo Diodes (APD) with low-noise charged-sensitive preamplifier (CSP) which detect the scintillation light generated within the detector cells. PHOS is operated at a working temperature of -25 °C. At this temperature the light yield is increased by a factor three compared to room temperature (20 °C) and the electronic noise is reduced. Both effects lead to an improved energy resolution.

The PHOS electromagnetic calorimeter is optimized to measure photons and neutral mesons in a low and intermediate p_T range up to 10 GeV/c with a high energy and position resolution. An energy resolution of $\sigma_E/E = 1.8\%/E \oplus 3.3\%/\sqrt{E} \oplus 1.1\%$, with E given in GeV is achieved. With still good resolution neutral pions can be measured up to ~ 50 GeV/c. On the low p_T side the small acceptance of PHOS restricts the measurement of neutral mesons as the opening angle of the decay photons increases with decreasing transverse momentum.

EMCal

The EMCal [55] [56] is a lead-scintillator sampling electromagnetic calorime-ter with a coverage of $|\eta_{lab}| < 0.7$ in pseudorapidity and $80° < \varphi < 187°$ in

azimuth. It consists of 12 super modules segmented into 12 288 towers in total which are approximately projective in η and φ to the interaction vertex at a radial distance of 4.6 m.

Each cell is composed of 77 alternating layers of lead absorber and plastic scintillator with light collection by the wavelength shifting fibers. The transverse size of the EMCal cells is 6×6 cm which is about twice as large as the effective Molière radius of the active cell material. The depths of the cells in terms of radiation length is 20 X_0 like in PHOS.

The active readout element of the EMCal detector is a radiation hard 5×5 mm^2 active area APD, connected directly to the back of a CSP. The energy resolution of the EMCal is parametrized as $\sigma_E / E = A^2 \oplus B^2 / E \oplus C^2 / E^2$ % with $A = 1.7 \pm 0.3, B = 11.3 \pm 0.3, C = 4.8 \pm 0.8$ and E given in units of GeV.

For the LHC Run2 the EMCal was extended with the Di-jet Calorimeter DCal [57] which uses six super modules of the EMCal design. The DCal subtends 60° in φ and $|\eta_{\text{lab}}| < 0.7$ in pseudorapidity. EMCal and DCal are situated almost back-to-back in azimuth, thereby forming a two arm spectrometer providing good acceptance for di-jets or correlation measurements.

2.2.4 The V0 Detector

The V0 detector [58][59] consists of two scintillator arrays at asymmetric positions (V0A and V0C), which cover a pseudorapidity range of $-5.1 < \eta_{\text{lab}} < -2.8$ and $1.7 < \eta_{\text{lab}} < 3.7$, respectively. Each of the V0 arrays is segmented in four rings in the radial direction and divided into eight sections in the azimuthal direction, giving 32 segments per array. The plastic scintillator arrays are equipped with wave-length shifting fibers which transfer the light to photomultiplier tubes.

The main purpose of the V0 system is to provide the ALICE experiment with a minimum bias trigger in pp, p–Pb or Pb–Pb collisions and with centrality based triggers in Pb–Pb. Using the time of flight of particles detected by both V0 arrays, collisions at the nominal interaction point and beam-gas interactions can be clearly distinguished. In addition, global properties of pp, p–Pb and Pb–Pb collisions such as particle multiplicity, collision centrality and event plane direction can be measured with the V0 system.

2.2.5 Charged Particle Tracking and Primary Vertex Reconstruction with ALICE

The starting point for tracking [60] in the central barrel is a first preliminary determination of the primary interaction vertex. For this purpose, the two innermost layers of the ITS, the SPD, are used. Cluster pairs from both SPD layers are connected by straight lines, forming so-called tracklets. The preliminary vertex is then found as the space point with the maximum tracklet density. In pp collisions, where several vertices can occur, the primary vertex is defined as the one with the largest number of contributing tracklets.

The track reconstruction follows an inward-outward-inward scheme [61] as depicted in Fig. 3.2 and further described below. For track finding and fitting with ITS and TPC the Kalman filter technique [62] is used.
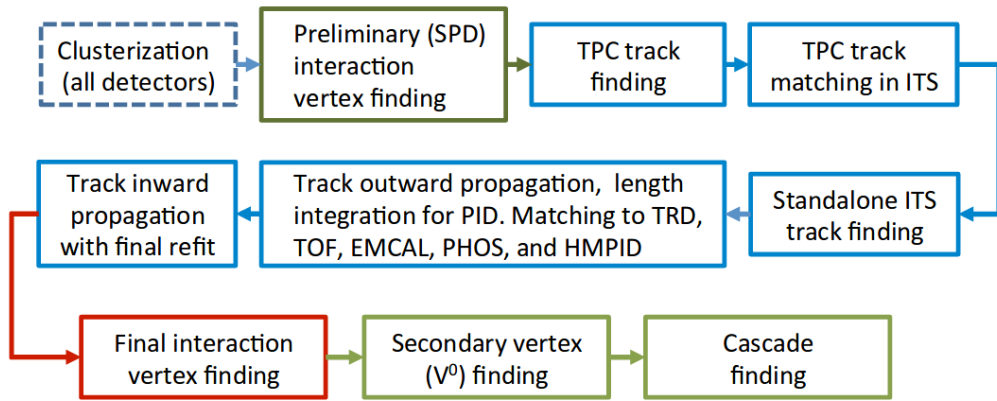

Figure 2.6: Schematic overview of the ALICE event reconstruction flow. [60]

The first inward stage of the tracking starts with track finding at large TPC radii. In a first step, two TPC cluster and the already determined preliminary interaction vertex are used as seeds for the tracks. In a second attempt, track seeds are built from three clusters without the vertex information. These seeds are propagated inwards and are updated at each step with the nearest cluster that lies within a given proximity cut. In case that two tracks found by the algorithm share too many clusters the track with the lower quality is rejected. The quality is determined based on the cluster density, number of clusters and momentum. In addition, only tracks with more than 20 clusters and at least 50% out of all findable clusters depending on the geometry are accepted. When the track is propagated to the inner TPC radius,

a preliminary particle identification via the specific energy loss $\mathrm{d}E/\mathrm{d}x$ is performed. The determined particle mass (with the charged pion mass as lowest possible value) is used for the further tracking steps to improve the corrections for ionization energy loss.

The reconstructed TPC tracks are propagated to the outermost ITS layer and serve as seeds for the ITS track finding. The seeds are updated at each ITS layer with every cluster within the proximity cut. The result of each update is saved as new seed. In this way each TPC track results in a tree of track hypotheses in the ITS. If no clusters are found within the proximity cut due to detection inefficiencies, the seed is further used for tracking, but the respective χ^2 is increased by a penalty factor. Again, the seeding procedure is performed in two passes, with and without the vertex information as constraint. When the TPC tracks are propagated to the innermost ITS layer, the track candidates are sorted according to their reduced χ^2. After a check for cluster sharing, the candidate with the highest quality from each hypothesis tree is added to the reconstructed event.

The reconstruction of low momentum tracks is limited for combined ITS-TPC tracks. For low momentum particles, the track radius, which can be approximated by $R \approx p/(0.3 \cdot B)$, with R given in meter, p in GeV$/c$ and B in Tesla, is not sufficiently large that they traverse more than the required $1/3$ of the radial TPC length. In addition, energy loss and multiple scattering in the detector material restrict the reconstruction of low p_{T} tracks to 200 MeV$/c$ for pions and 400 MeV$/c$ for protons for combined ITS-TPC tracks.

To further reduce the cutoff, a standalone ITS tracking is performed for clusters that were not used in ITS-TPC tracks. For this purpose, helical seeds are built from two clusters of the three innermost ITS layers in combination with the interaction vertex and are propagated outwards. The track hypotheses are refitted by a Kalman filter and the track with the best χ^2 is accepted. The clusters that contribute to those low transverse momentum tracks are removed for the further tracking procedure. With the ITS standalone tracking low p_{T} particles can be reconstructed down to about 80 MeV$/c$.

Subsequent to the ITS reconstruction all tracks are extrapolated to their point of closest approach to the preliminary interaction vertex. From there, the outward propagation starts by refitting the tracks with the Kalman filter using the clusters from the previous stage. For each step the track length integral and the expected time of flight for various particle species are updated. This allows for a subsequent particle identification with the Time Of Flight (TOF) [63] detector. Once the track reaches the outer TPC wall, it is

further propagated outwards to match with signals in the adjacent detectors as TOF, the Transition Radiation Detector (TRD) [64] or the electromagnetic calorimeters. So far, the detectors at larger radii than the TPC are not used to update the track kinematics, but their information is stored to the track object and can be used for particle identification.

At the final reconstruction step, all tracks are propagated inwards again, starting at the outer TPC radius. The tracks are refitted in TPC and ITS and the track's position, direction, inverse curvature and the covariance matrix are determined. Once the tracking is finished, the final interaction vertex is determined. This is done by using so-called global tracks, reconstructed in ITS and TPC, which leads to a higher precision than using only SPD tracklets.

2.3   The ROOT and AliRoot Framework

The presented neutral meson analysis is performed within the ALICE offline framework AliRoot [65] which is an extension of ROOT [66].

ROOT is an object orientated framework and library for large scale data analysis implemented in C++. It has been initially developed at CERN by Rene Brun and Fons Rademakers in 1994 as a replacement of The Physics Analysis Workstation PAW [67] written in FORTRAN. The development of ROOT was needed as PAW could not be significantly scaled up to cope with the huge data amount expected at the LHC. ROOT provides a large set of tools needed for analyses in particle physics such as mathematical operations, plotting and fitting of histograms and graphs or visualization tools.

Classes and functions that are exclusively required by the ALICE collaboration like a realistic implementation of the ALICE detector are embedded within the AliRoot framework. AliRoot interfaces with several event generators as PYTHIA [68], HIJING [69] or DPMJet [70]. Those generators simulate the collision of protons or lead ions and all particles produced in the primary interaction. The particle transport through the detector and the interaction with the detector material as well as the detector response is then further simulated with GEANT [71].

Reconstructed events can be stored in two different formats: as ESD (Event Summary Data) files and as AOD (Analysis Object Data) files. While the ESD files nearly contain all reconstruction and track parameters, AOD files are compressed by about a factor three and only contain relevant information for the analysis. In case that needed information is missing in the AODs it can be provided by additional deltaAOD files. Due to the absence of those deltaAOD files at the beginning of the presented meson analysis, ESD files have been used.

Via the AliEn system [72] AliRoot is connected to the computing grid used by the ALICE collaboration. Grid computing is necessary to handle the large amount of data produced at the LHC.

The analysis has been performed using the analysis framework of the Photon Conversion Group [73]. This framework has been developed to analyze neutral mesons and direct photons via conversions, but has recently been updated to also include measurements with calorimeters.

Chapter 3

Neutral Meson Analysis via Photon Conversions

Due to their short $c\tau$ of 25.5 nm and 0.15 nm (corresponding to mean life times of $8.52 \cdot 10^{-17}$ s and $5.0 \cdot 10^{-19}$ s [13], respectively) neutral pions and η mesons produced in the primary interaction already decay within the beam pipe. Thus, they cannot be directly measured in the ALICE detector, but have to be identified via their decay products. In case of the presented analysis, the mesons are reconstructed via their two-photon decay channels:

$$\pi^0 \to \gamma\gamma \quad \text{(branching ratio : 98.823\%)}$$

$$\eta \to \gamma\gamma \quad \text{(branching ratio : 39.31\%)}$$

In ALICE, photon reconstruction can be performed in different ways: either with one of the electromagnetic calorimeters, PHOS and EMCal, or with the reconstruction of electron-positron pairs resulting from photon conversions in ITS and TPC. The latter so-called Photon Conversion Method (PCM) allows for the reconstruction of low momentum photons and thus also neutral mesons can be measured down to very low p_T. In the presented analysis neutral pions and η mesons are measured from 0.3 GeV/c and 0.7 GeV/c on, respectively.

In this chapter the analysis of neutral mesons via photon conversions in p–Pb collisions at $\sqrt{s_{NN}}$ = 5.02 TeV is described. Section 3.1 addresses the analyzed data and Monte Carlo samples, as well as the event selection. The reconstruction and selection of conversion photons is covered in Sec. 3.2. The extraction of the neutral meson raw signal and the necessary spectra corrections are described in Sec. 3.3 and Sec. 3.4, respectively. The evaluation

of the systematic uncertainties is discussed in Sec. 3.5. All these reconstruction details are explained using the example of the minimum bias analysis. Modifications that have been made for the analysis of different multiplicity classes are treated in Sec. 3.6.

3.1 Data Sets and Monte Carlo Simulations

3.1.1 Data Sample

The data used for this analysis has been recorded during the p–Pb run in January and February 2013 at a collision energy of 5.02 TeV. In total, approximately 120 million minimum bias events are available in the analyzed data periods LHC13b and LHC13c. This corresponds to an integrated luminosity of about 50 μb^{-1}. The utilized runs for the analysis can be found in Tab. 3.1, runs with missing SDD signals are not considered. Data of the p–Pb pilot run from September 2012 recorded at the same collision energy is not taken into account since it does not significantly improve the statistics but could lead to bigger systematic uncertainties due to different run settings.

LHC13b	LHC13c
195344, 195351, 195389, 195391,	195529, 195531, 195566, 195567, 195568,
195478, 195479,195480, 195481,	195592, 195593, 195596, 195633, 195635,
195482, 195483	195644, 195673, 195675, 195677

Table 3.1: List of analyzed data runs.

The 2-in-1 magnet design of the LHC requires the same magnetic rigidity for both colliding beams, which leads to asymmetric beam energies for p–Pb collisions. For the used data sample, the beam energies per nucleon were $E_p = 4$ TeV for the proton beam and $E_{Pb} = 4$ TeV $\cdot (Z/A) = 4$ TeV $\cdot (82/208) = 1.58$ TeV for the Pb beam, leading to a collision energy of $\sqrt{s_{NN}} = \sqrt{4E_p \cdot E_{Pb}} = 5.02$ TeV. This asymmetry results in a shift of the center of mass system (cms) with respect to the laboratory system. In p–Pb collisions, the nucleon-nucleon cms is moving with $\Delta y \approx \frac{1}{2} \ln \left(\frac{208}{82} \right) \approx 0.465$ in rapidity, with positive rapidity defined by the direction of the proton beam.

3.1.2 Monte Carlo Productions

For the spectra corrections (see Sec. 3.4) two different Monte Carlo samples have been used: the DPMJet [70] production LHC13b2_efix_px (x=1,2,3,4; different productions with same settings and statistics) and the HIJING [69] production LHC13e7, both "anchored" to the data samples LHC13b and LHC13c. This means that statistics and detector conditions of the data periods are emulated in the simulations. While the DPMJet sample is purely minimum bias, neutral mesons with a flat distribution in p_{T} have been added to the minimum bias part of the HIJING production. In this way the π^0 and η signals are enhanced at higher transverse momenta where the neutral meson corrections suffer from too low statistics. A short description of the used Monte Carlo event generators is given in the following paragraphs.

DPMJet

The DPMJet event generator is based on the Dual Parton Model [74]. Soft particle production is dominant in most events of high energy hadronic and nuclear collisions. As the momentum transfer is small, pQCD calculations cannot be applied for soft processes. Therefore, they are usually treated by phenomenological models. The Dual Parton Model is such a model, based on the large-N expansion of non-perturbative QCD and the Reggeon field theory. Hard processes are described by lowest order pQCD within DPMJet. The Glauber-Gribov formalism is used for the calculation of nuclear cross sections.

HIJING - Heavy Ion Jet INteraction Generator

With the HIJING Monte Carlo program jet and associated particle production in high energy pp, p–A and A–A collisions can be studied. For this purpose, pQCD-inspired models for multijet production are combined with pheno-menological Lund-type models for soft interactions. Binary approximation and the Glauber model are used to simulate multiple interactions in p–A and A–A collisions. Besides multiple minijet production, also parton shadowing via a parametrized parton distribution function inside a nucleus, as well as jet quenching, modeled via energy loss of partons in the produced dense matter, are included in the model. For the hadronization the Lund jet fragmentation model is used.

3.1.3 Event Selection

The minimum bias analysis is performed for the periods LHC13b, reconstruction pass 3, and LHC13c, reconstruction pass 2. Despite the different pass numbers, both periods have been reconstructed with the same settings. For the event selection the standard Physics Selection with a minimum bias trigger (ALICE internal kINT7), which requires a coincident signal in V0A and V0C, is used. This removes contributions from single-diffractive and electromagnetic events. Only events with a reconstructed primary interaction vertex are taken into account. In addition, the standard p–Pb vertex selection (using AliAnalysisUtils::IsVertexSelected2013pA()) requires at least one contributor to the vertex (see Sec. 2.2.5) and the usage of SPD data for the vertex reconstruction. The z-coordinate of the vertex has to lie within 10 cm to the nominal interaction point.

Also events with more than one p–Pb collision, so-called pile-up events, are removed from the event sample. Those events are identified by the reconstruction of multiple primary vertices using the SPD. Furthermore, events are categorized as background events if the number of clusters in the SPD exceeds the number of SPD tracklets by the given relation:

$$N_{\text{cluster, SPD}} \; > \; 60 \; + \; 4 \cdot N_{\text{tracklets, SPD}} \tag{3.1}$$

The corresponding distributions for the analyzed data and Monte Carlo (MC) samples are shown in Fig. 3.1. The fraction of rejected events due to these two selection criteria amounts to 6‰.

After this quality selection approximately 103 million out of 123 million ESD events are still available for the minimum bias analysis, see Tab. 3.2. The number of accepted events is used for normalization.
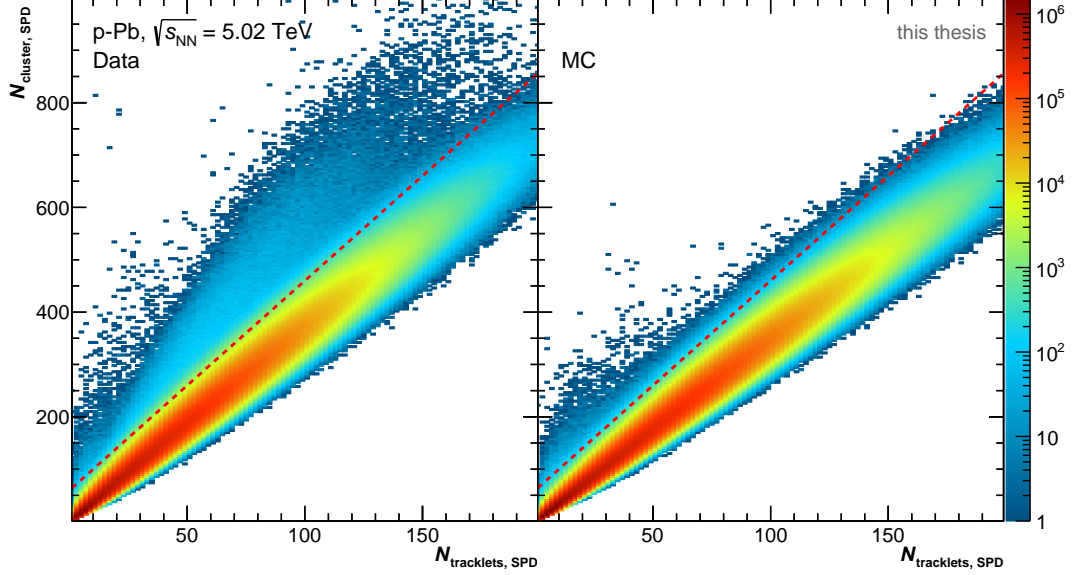
Figure 3.1: Number of SPD clusters versus number of SPD tracklets for the analyzed Data (left) and Monte Carlo sample (right). Events with an entry above the red dashed line are removed from the further analysis.

	Sample	$\sqrt{s_{NN}}$	Multiplicity	Events	accepted Events
Data	LHC13b.pass3	5.02 TeV	min bias	$30.1 \cdot 10^6$	$24.9 \cdot 10^6$
	LHC13c.pass2	5.02 TeV	min bias	$92.8 \cdot 10^6$	$77.9 \cdot 10^6$
MC	LHC13b2_efix_px	5.02 TeV	min bias	$130.3 \cdot 10^6$	$111.9 \cdot 10^6$
	LHC13e7	5.02 TeV	min bias	$48.1 \cdot 10^6$	$42.1 \cdot 10^6$

Table 3.2: Number of p–Pb events passing the event selection for data and Monte Carlo simulations.

3.2   Photon Reconstruction and Selection

Photons converted into e^+e^- pairs are reconstructed with a secondary vertex algorithm that searches for oppositely charged track pairs originating from a common vertex, referred to as V^0 [60]. The working principle of this so-called V^0 finder is illustrated in Fig. 3.2 with the decay of a K_s^0 into two pions as example. Photons that convert into e^+e^- pairs are reconstructed analogously. The name V^0 refers to the neutral mother particle and the characteristic V-like shape of the daughter tracks. Since only secondary tracks should be taken into account, the secondary vertex finder checks that the distance of closest approach (DCA) to the primary interaction vertex is larger than 0.5 mm. For each unlike-sign pair of secondary tracks the point of closest approach (PCA), which corresponds to a possible secondary vertex, is calculated. These V^0 candidates have to pass certain selection criteria. The distance of the two charged tracks at the PCA has to be smaller than 1.5 cm. It is also checked that the PCA is closer to the interaction vertex than the innermost hits of the charged tracks. Otherwise, these tracks could not originate from the PCA. In addition, the total momentum vector of the reconstructed pair $\vec{p}_{\text{pair}}$ has to point to the interaction vertex. Therefore, $\cos(\theta)$ is required to be larger than 0.9, with θ being the angle between the V^0 momentum vector and the straight connection between primary and secondary vertex.

In general, two different V^0 finder algorithms with similar working principles are available in the AliRoot framework. Their main difference is the stage of the track finding process. The so-called on-the-fly finder runs during the initial reconstruction of the tracks and the offline finder runs after all tracks are processed and stored in ESD events. For that reason the on-the-fly finder can access more track relevant information than the offline finder and gives a better spatial and momentum resolution of reconstructed V^0 candidates. In addition, the secondary track selection criteria for the offline finder are not optimized for the photon reconstruction in p–Pb collisions and cannot be well reproduced by the Monte Carlo productions. The on-the-fly V^0 finder is hence used as standard for the presented analysis and is further only referred to as V^0 finder.

The V^0 finder is optimized for the reconstruction of massive particles with the K_s^0 decay as standard hypothesis and assumes a non-zero opening angle between the two oppositely charged tracks. As the opening angle for the conversion of a massless photon is close to zero, the calculated conversion point can be displaced. Thus, the resolution of the conversion point is further

improved by recalculating the secondary vertex under the assumption that the momenta of the conversion products are parallel at the moment of their creation, as described in [75]. The obtained mean resolution of the conversion point was found to be better than $3\,\mu$rad in φ, while the resolution in R and z is approximately 1.3 cm and 0.8 cm, respectively [76].

Figure 3.2: Illustration of the secondary vertex reconstruction using the decay of a K^0_s into two pions as example. The conversion of a photon could be presented analogously. [60]

Main contributors to the reconstructed V^0 sample are K^0_s, Λ, $\bar{\Lambda}$ and γ. To select photons among the V^0 candidates, several selection criteria, so-called cuts, are applied. These cuts can be split into three categories: cuts on the charged track level to ensure a good track quality, particle identification (PID) cuts on the track level for electron selection and pion rejection, and cuts on the V^0 sample that exploit the specific conversion topology of the photon. They will be discussed in more detail in the following subsections.

3.2.1 Track and V^0 Cuts

After the selection of the V^0 candidates, several requirements are made for the secondary tracks to ensure a good quality. Tracks that do not fulfill the TPC refit condition and those with a kink-topology are rejected for the further analysis. Such a charged track with a sharp change of direction can for example be cause by a kaon that decays into a muon and a neutrino. Also a minimum track p_T of $50\,\mathrm{MeV}/c$ is required. The ratio of reconstructed TPC clusters over all theoretically findable clusters has to be at least 0.6 for both tracks.

Additionally to these quality cuts, also the position of the conversion point and the reconstructed tracks is restricted to the fiducial volume of the detector. The pseudorapidity of the V^0 candidate and the e^+e^- tracks in the laboratory reference frame, $\eta_{V^0,\,\mathrm{lab}}$, has to lie within $|\eta_{V^0,\,\mathrm{lab}}| < 0.9$, which corresponds to a pseudorapidity range of $-1.365 < \eta_{V^0,\,\mathrm{cms}} < 0.435$ in the center of mass system. The pseudorapidity is determined based on the angle between the beam-axis and the orientation of the 3-momentum vector of the particle candidate in the z-R-plane alone. The chosen $\eta_{V^0,\,\mathrm{lab}}$ range is also used in pp and Pb–Pb analyses and covers the full rapidity range available for this analysis for which the acceptance and efficiency can be determined most reliably.

As the starting point of the trajectory is not taken into account for the pseudorapidity cut, some photon candidates will pass it although they are not contained in the geometrical η_{lab} region defined by the center of the detector and the corresponding angles in the z-R-plane. Therefore, an additional condition has to be satisfied for the V0 candidates:

$$R_{\mathrm{conv}} > |z_{\mathrm{conv}}| \cdot \tan\left(2 \cdot \arctan(\exp(-\eta_{\mathrm{cut}}))\right) - z_0 \,, \tag{3.2}$$

with $z_0 = 7$ cm and $\eta_{\mathrm{cut}} = 0.9$. The coordinates of the secondary vertex (i.e. $R_{\mathrm{conv}}, z_{\mathrm{conv}}$) are determined with respect to the nominal center of the detector $(x,y,z) = (0,0,0)$ and do not depend on the primary vertex position. This cut is often referred to as *line-cut* and is similar to a cut on the geometrical η distribution of the conversion points with $(0,0,0)$ as point of their origin.

To ensure the reconstruction of secondary tracks with enough findable TPC clusters, secondary vertices with $R_{\mathrm{conv}} > 180$ cm and $z_{\mathrm{conv}} > 240$ cm are rejected. Furthermore, all V^0 candidates with $R_{\mathrm{conv}} < 5$ cm are rejected to reduce the contamination from Dalitz decays. The Dalitz decay $\pi^0 \rightarrow \gamma^*\gamma \rightarrow e^+e^-\gamma$ includes a primary e^+e^- pair coming from the virtual photon that can

Track & V^0 Cuts	p–Pb Analysis
V^0-finder	on-the-fly
e^+e^- track p_T	$p_{T,track} > 0.05\,\mathrm{GeV}/c$
findable clusters	$\frac{N_{\text{cluster TPC}}}{N_{\text{findable clusters}}} > 60\%$
pseudorapidity	$\mid \eta_{V^0,\,\text{lab}} \mid\, < 0.9$
line-cut	$R_{\text{conv}} > \mid z_{\text{conv}} \mid \cdot \tan\left(2 \cdot \arctan(\exp(-\eta_{\text{cut}}))\right) - z_0$ $z_0 = 7\,\mathrm{cm}$ and $\eta_{\text{cut}} = 0.9$
conversion radius	$5\,\mathrm{cm} < R_{\text{conv}} < 180\,\mathrm{cm}$
z_{conv}	$\mid z_{\text{conv}} \mid\, < 240\,\mathrm{cm}$
multiple counting	$\vartheta_{\text{opening}} < 0.02\,\mathrm{rad}$ and $\Delta R < 6\,\mathrm{cm}$

Table 3.3: Standard cuts for the track and V^0 selection.

be misidentified as a secondary e^+e^- pair with small conversion radius. For conversion radii larger than $5\,\mathrm{cm}$, the Dalitz contamination is negligible.

It is observed that in some rare cases, about 0.3‰, the signal of one converted photon is interpreted as coming from two or even more photons and is hence written more than ones into the list of photon candidates. This happens for data and Monte Carlo simulations. These multiply counted photons can be identified by their similar conversion radius and the small opening angle between them. If two or more photons with an opening angle $\vartheta_{\text{opening}} < 0.02\,\mathrm{rad}$ and a difference of the conversion radii $\Delta R < 6\,\mathrm{cm}$ are found in an event, only the photon candidate with the lowest χ^2 is kept for the further analysis.

Table 3.3 shows an overview of the standard cuts used for the track and V^0 selection. The spatial distributions in the x-y and the z-R plane of the reconstructed conversion points that pass these selection criteria are shown in Fig. 3.3.
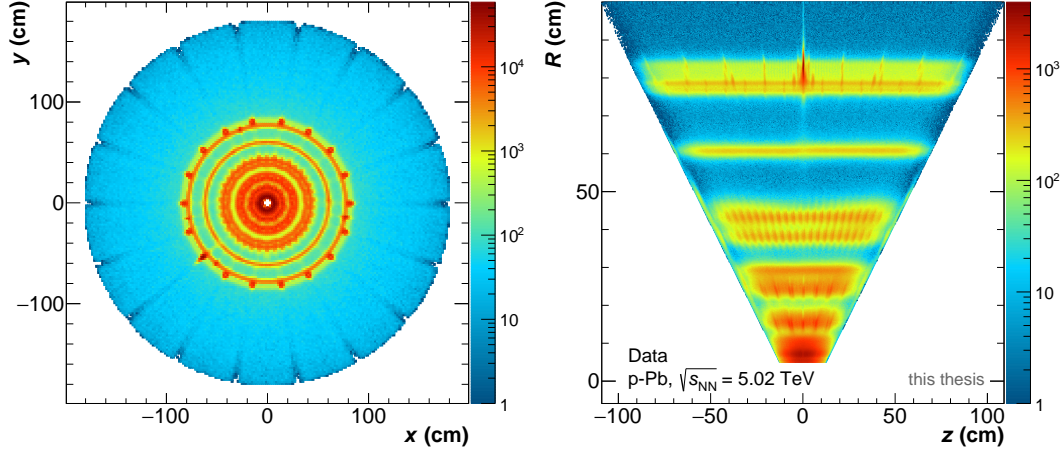
Figure 3.3: Reconstructed conversion points in the x-y plane (left) and the z-R plane that pass the track and V^0 selection criteria.

3.2.2 PID Cuts

The tracks that pass the track and V^0 selection are not necessarily electrons from photon conversions, but can also be other decay products, mostly pions, of particles that fulfill the V^0 topology. To select the converted photons among these V^0 candidates electron identification and pion rejection cuts, which can be found in Tab. 3.3, are applied to the secondary tracks.

In general, electrons in ALICE can be identified by five different techniques:

- specific energy loss dE/dx in the ITS

- specific energy loss dE/dx in the TPC

- time-of-flight measurement with the TOF

- transition radiation or dE/dx measurement in the TRD

- energy deposit in the calorimeters

The electron identification for this analysis relies on the specific energy loss measurement in the TPC, since the fraction of secondary tracks in the other detectors is significantly lower and would dramatically decrease the statistics. This is more crucial for the neutral meson analysis than a 100% pure electron sample, since the mesons are identified via their invariant mass and a larger purity mainly suppresses the background. Smaller contributions, mainly by pions, can be tolerated.

PID Cuts	p–Pb Analysis
$n\sigma_{e^\pm}$ TPC dE/dx	$-4 < n\sigma_{e^\pm} < 5$
$n\sigma_{\pi^\pm}$ TPC dE/dx	$0.4\,\mathrm{GeV}/c < p < 100.0\,\mathrm{GeV/c}$: $n\sigma_{\pi^\pm} > 1$

Table 3.4: Standard electron identification cuts for the p–Pb analysis. The cuts are applied in the given order. The values stated here select the candidates that are kept.

The cut is applied around the dE/dx hypothesis for being an electron (electron-line) in terms of $n\sigma_{e^\pm}$. In this way, most of the electrons are kept while the majority of pions is suppressed. By default, all particles with an energy loss that does not lie within -4 $n\sigma_{e^\pm}$ and +5 $n\sigma_{e^\pm}$ around the electron-line are rejected. Additionally, a cut with respect to the pion hypothesis (pion-line) is performed to further suppress charged pions. This cut can be varied independently for low and high momentum tracks. The transition between low and high momentum is also adjustable, but not performed for the standard cut. The default choice is to reject everything below $+1\sigma_{\pi^\pm}$ with respect to the pion-line for tracks with $0.4\,\mathrm{GeV}/c < p < 100\,\mathrm{GeV/c}$.

Fig. 3.4 shows dE/dx and $n\sigma_{e^\pm}$ against particle momentum for all secondary tracks in the analyzed data sample before and after the described track and PID cuts. The respective distribution for the analyzed DPMJet and HIJING Monte Carlo productions are plotted in Fig. 3.5.

3.2.3 Photon Topology Cuts

After the mentioned track selection and electron identification cuts, the selected photon sample has a purity of about 80%. To further improve this, constraints on the photon candidate mass and on the opening angle between the reconstructed photon candidate momentum vector and the vector between collision vertex and conversion point can be made. These constraints are not made by direct cuts on the respective parameters, but indirectly via the AliRoot KFParticle package [77, 78] which is used for the photon reconstruction. In this way, the mentioned conditions can already be required at the reconstruction stage and the cut is performed on the reduced
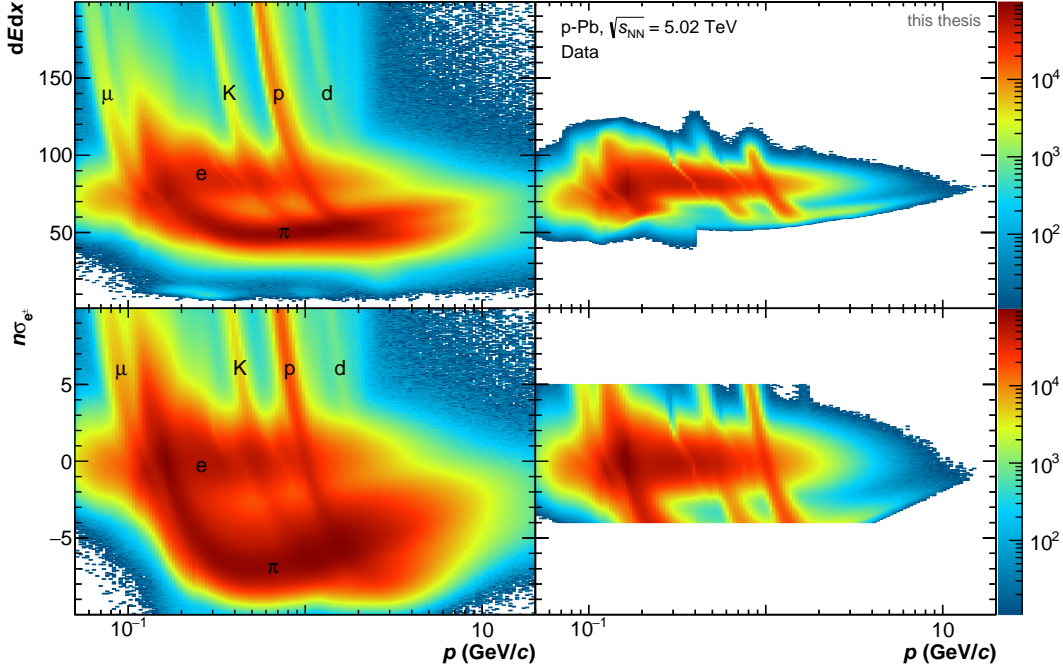
Figure 3.4: Specific energy loss in the TPC versus particle momentum for the analyzed data periods LHC13b and LHC13c. The upper plots show the dE/dx in arbitrary units before (left) and after (right) all described track and PID cuts. The lower plots show the energy loss in terms of standard deviations with respect to the electron hypothesis, $n\sigma_{e^\pm}$, before (left) and after (right) the cuts.

χ^2 of the converted photon fit to the V^0 candidate. This distribution can be interpreted as the photon "quality".

Another cut applied on the photon sample is the so-called ψ_pair cut. Here, ψ_pair is defined as the opening angle of the e^+e^- pair plane, perpendicular to the magnetic field (x-y-plane in ALICE) and the plane defined by the opening angle of the pair [79]. It can also be written as

$$\psi_\text{pair} = \arcsin\left(\frac{\Delta\theta}{\zeta_\text{pair}}\right) , \tag{3.3}$$

where $\Delta\theta$ is the polar angle difference between electron and positron tracks, $\Delta\theta = \theta(e^+) - \theta(e^-)$, and ζ_pair is the total opening angle between them. The position of the ψ_pair angle in the ALICE coordinate system with the magnetic field orientated along the z-axis is illustrated in Fig. 3.6. For converted photons with vanishing opening angle between the e^+e^- pair, ψ_pair is close to and peaked at zero degree. For heavier particles or Dalitz decays it usually
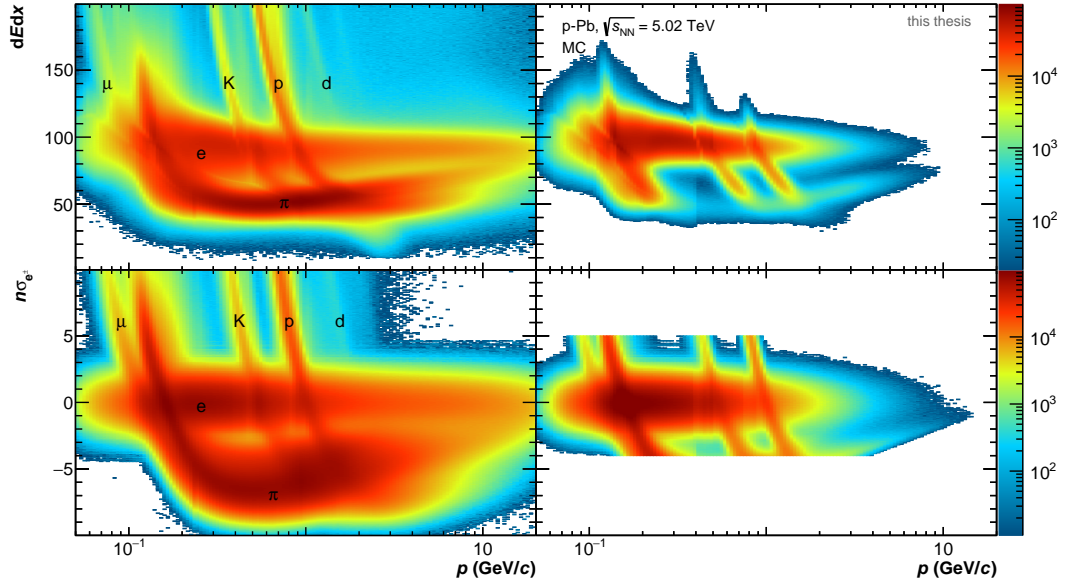
Figure 3.5: Specific energy loss in the TPC versus particle momentum for the used DPMJet and HIJING Monte Carlo productions. The upper plots show the dE/dx in arbitrary units before (left) and after (right) all described track and PID cuts. The lower plots show the energy loss in terms of standard deviations with respect to the electron hypothesis, $n\sigma_{e^{\pm}}$, before (left) and after (right) the cuts.
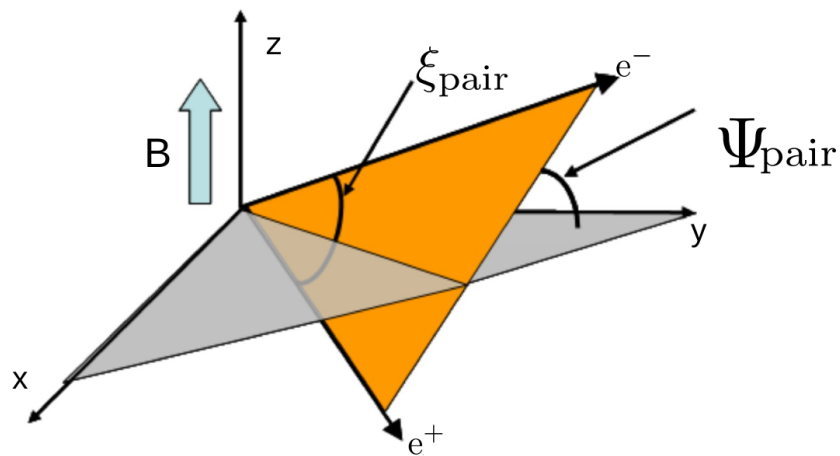
Figure 3.6: Illustration of the ψ_{pair} definition. [79]

Photon Topology Cuts	p–Pb Analysis
$\chi^2_{\max}$	$= 30$
$\psi_{\mathrm{pair,max}}$	$= 0.1$
$\left(\frac{\alpha}{0.95~\mathrm{GeV}/c}\right)^2 + \left(\frac{q_{\mathrm{T}}}{q_{\mathrm{T,\,max}}}\right)^2$	< 1

Table 3.5: Standard photon selection cuts for the p–Pb analysis.

has larger values. Combinatorial background has by definition random, but maybe not uniform values of invariant mass and opening angles. The corresponding ψ_{pair} distribution is flat.

The χ^2 cut and the ψ_{pair} cut can be applied separately or in a combined way by defining a two-dimensional rectangular cut in the ψ_{pair} versus χ^2 distribution as it is shown in Fig. 3.7. For the standard analysis this two-dimensional cut is chosen as it corresponds to the shape of the signal and leads to an increased photon purity compared to two separate cuts with the same cut values. All V^0 candidates that don't fulfill $|\psi_{\mathrm{pair}}| < \frac{-\psi_{\mathrm{pair,\,max}}}{\chi^2_{\gamma,\mathrm{max}}} \cdot \chi^2_{\gamma} + \psi_{\mathrm{pair,\,max}}$ with the given $\chi^2_{\gamma,\mathrm{max}}$ and $\psi_{\mathrm{pair,max}}$ from Tab. 3.5 are rejected.

The remaining $\mathrm{K}^0_{\mathrm{S}}$, Λ and $\overline{\Lambda}$ are effectively removed by cutting on the $q_{\mathrm{T}} = p \times \sin\theta_{\mathrm{mother\text{-}daughter}}$ of the Armenteros-Podolanski plot [80]. q_{T} is the projection of the momentum of the daughter particle with respect to the mother particle in the transverse direction. In the Armenteros-Podolanski plot this is plotted versus the longitudinal momentum asymmetry ($\alpha = (p_{\mathrm{L}+} - p_{\mathrm{L}-})/(p_{\mathrm{L}+} + p_{\mathrm{L}-})$). Since the opening angle of the electron-positron pair is very small, the direction of the daughter particle is nearly the same as for the mother. Therefore, converted photons have a q_{T} close to zero and can be well distinguished from the heavier V^0 candidates. Due to the same mass of the daughter particles the real photons appear symmetric in α as well as the $\mathrm{K}^0_{\mathrm{S}}$, whereas the distributions for Λ and $\overline{\Lambda}$ are shifted to positive and negative α, respectively. There are two possibilities to apply the q_{T} cut: a one dimensional cut in the Armenteros-Podolanski plot where all V^0 candidates with $q_{\mathrm{T}} > q_{\mathrm{T,max}}$ are rejected, or a two dimensional cut where all V^0 candidates with $\left(\frac{\alpha}{0.95~\mathrm{GeV/c}}\right)^2 + \left(\frac{q_{\mathrm{T}}}{q_{\mathrm{T,max}}}\right)^2 > 1$ are rejected. For the standard analysis the two dimensional method with $q_{\mathrm{T,max}} = 0.05~\mathrm{GeV/c}$ is used. The Armenteros-Podolanski plot for all V^0 candidates after the track selection (left) and after
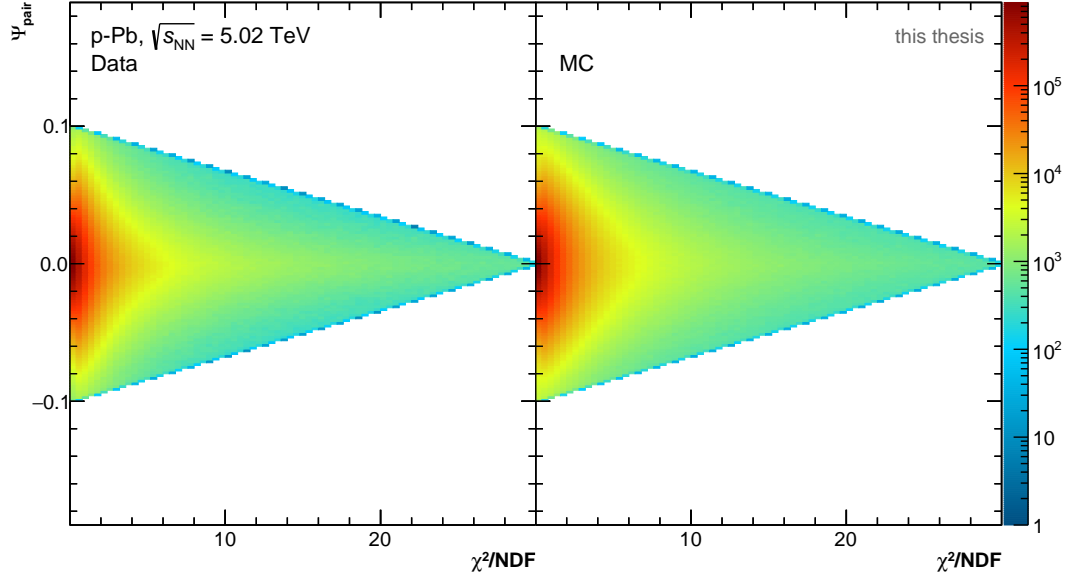
Figure 3.7: ψ_{pair} versus reduced χ^2 distribution for the used data (left) and Monte Carlo sample (right) after the combined ψ_{pair}-χ^2 cut.

the electron and photon selection (right) is shown in Fig. 3.8. It is clearly visible that the majority of V^0 candidates except the real photons does not survive this selection which gives a clean remaining photon sample.

Figure 3.9 shows the purity of the selected photon sample versus p_{T} for the standard analysis. It is deduced from the Monte Carlo productions as the ratio of all validated true primary photons over all photon candidates found in the simulated events. The described photon selection criteria lead to a clean sample with a purity between 98 and 99%.
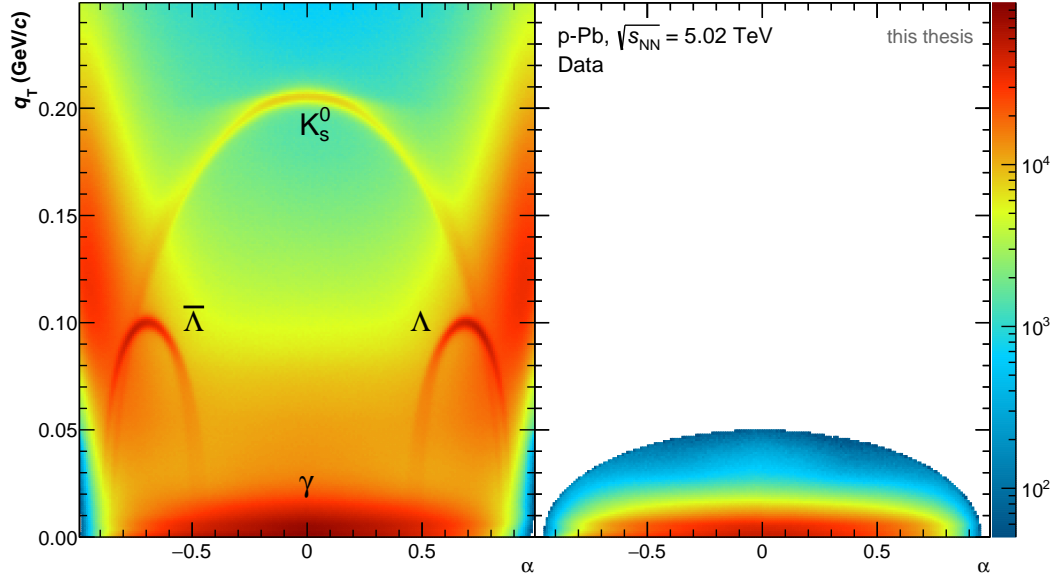
Figure 3.8: Armenteros-Podolanski plot for all V^0 candidates after the track selection (left) and after all electron identification and photon selection cuts (right).
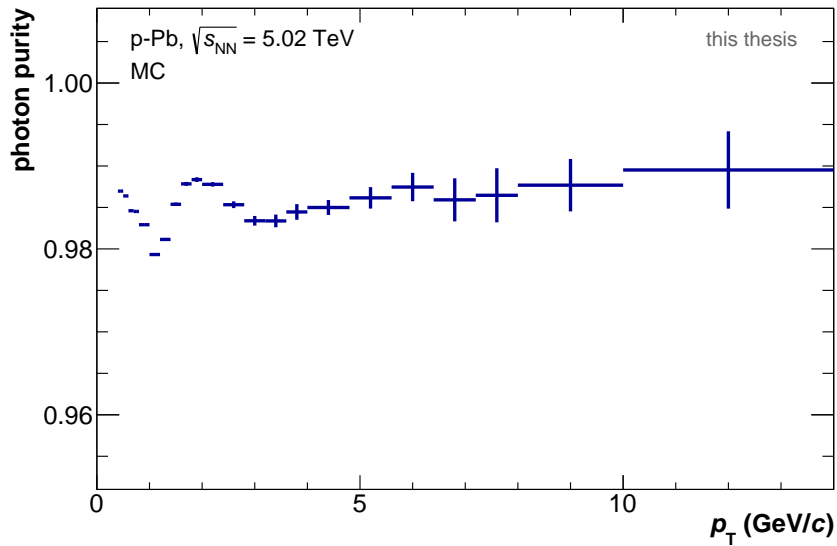
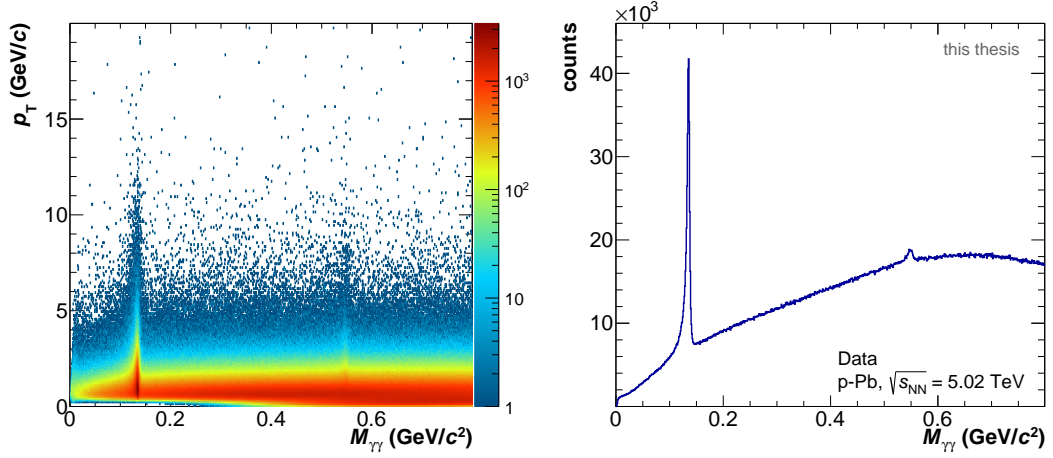Figure 3.9: p_T dependency of the purity of the photon sample at midrapidity.

Figure 3.10: Left: Transverse momentum versus invariant mass for all selected photon candidate pairs. Right: Two-photon invariant mass distribution for all transverse momenta.

3.3 Neutral Meson Reconstruction

In this section the extraction of the neutral meson raw yields is described. This is done on a statistical basis using the invariant mass of two reconstructed photons.

3.3.1 Invariant Mass Technique

For the neutral meson reconstruction, the photon candidates of each event selected with the criteria mentioned in Sec. 3.2 are combined to pairs. In addition, the reconstructed meson candidate has to lie within the rapidity window of $|y_{\text{lab}}| < 0.8$.

For these pairs the invariant mass

$$M_{\gamma\gamma} = \sqrt{2E_{\gamma_1}E_{\gamma_2}(1 - \cos\theta_{12})}, \tag{3.4}$$

is calculated, where E_{γ_1} and E_{γ_2} denote the energies of the two photon candidates and θ_{12} the opening angle between them in the laboratory system. With this technique, the neutral mesons cannot be identified directly one by one, but they appear as an excess in the invariant mass distribution close to their respective mass. For the π^0 this is $m_{\pi^0} = 134.9770 \pm 0.0005\,\text{MeV}/c^2$ and for the η meson $m_\eta = 547.862 \pm 0.01\,\text{MeV}/c^2$ [13].

In the left panel of Fig. 3.10 the transverse momentum of the paired photon candidates is plotted against their invariant mass. Already here, the excess at the neutral pion and η mass is visible. It becomes even clearer in the projection to the x-axis shown in the right panel. An explicit peak at $135\,\mathrm{GeV}/c^2$ appears over the combinatorial background caused by paired photons that don't originate from the same meson. Also a peak at the η meson rest mass is discernible, although much less pronounced than the π^0 peak.

In order to extract p_T-differential raw yields, the invariant mass distribution is binned into several p_T bins and the integral of the meson peak without background is evaluated. For this, a reliable background description and subtraction is needed.

3.3.2 Background Estimation

There are different ways to estimate the combinatorial background under the meson peaks. One possible option would be to fit it with a polynomial function. But it is difficult to estimate the shape of the background below the signal peak just from the regions left or right to the peak. A more elaborated approach is to estimate the background with photon pairs of the used data sample for which the correlations between each other have been destroyed. This can for example happen by rotating single photons in an event by a random angle before pairing them with other photons.

The standard technique that has been chosen for this analysis is the so-called event mixing method. Here, photons from different events which are by default not correlated are paired. For this purpose, photon candidates of 80 reconstructed events are stored in a first-in-first-out buffer for the event mixing. As the resulting invariant mass distribution is purely combinatorial it is well suited to describe the shape of the combinatorial background. Due to different kinematical configurations and combinatorics, the shape of the distribution depends on the transverse momentum of the meson candidate as well as on the multiplicity in the event and on the z-coordinate of the primary vertex. To account for this, the photon candidates are binned in different multiplicity and z-classes and are only combined with other photons of the same event mixing class. The binning was chosen in a way that the statistics is nearly the same in all bins. The bin limits of the different categories in the minimum bias analysis are shown in Tab. 3.6. Note that for the multiplicity assumption two different parameters can be used: the number of charged particle tracks in the acceptance and the number of photon candidates in the

Category	Bin	p–Pb Analysis
V^0 multiplicity	1	0 - 2
	2	3
	3	4
	4	5
	5	≥ 5
Charged track multiplicity	1	0 - 7
	2	8 - 16
	3	17 - 29
	4	30 - 500
z-vertex coordinate (cm)	1	-50.00 - -5.85
	2	-5.85 - -3.35
	3	-3.35 - -1.15
	4	-1.15 - 0.85
	5	0.85 - 2.95
	6	2.95 - 5.55
	7	5.55 - 50.00

Table 3.6: Definition of the p–Pb minimum bias event mixing classes.
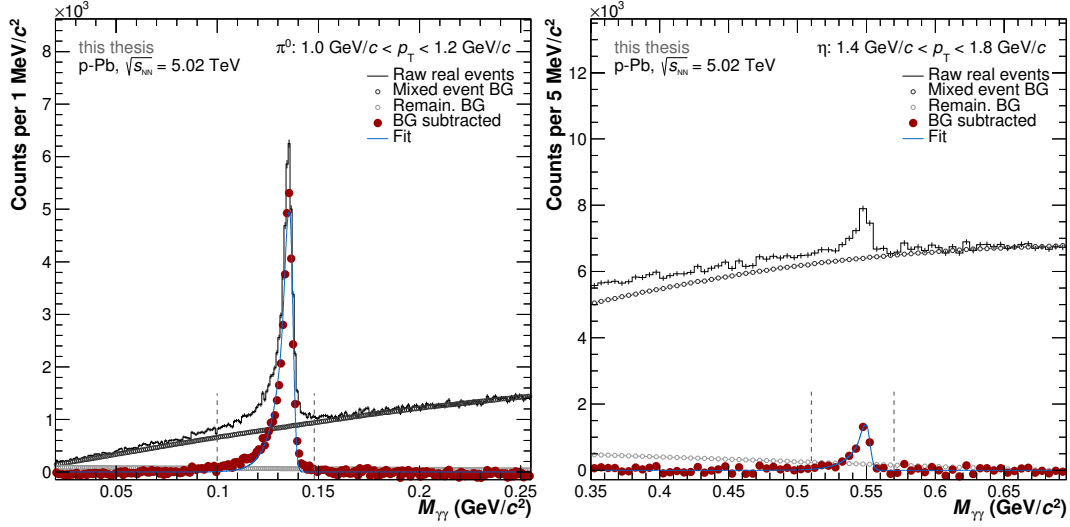
Figure 3.11: Exemplary invariant mass distributions before and after background subtraction for the π^0 (left) and η meson reconstruction.

event. The standard method for the combinatorial background description is the mixed event technique with the V^0 number used as the multiplicity estimator. The event mixing method with the charged track multiplicity as estimator is used for comparisons and the systematic error calculation.

3.3.3 Raw Yield Extraction

In order to extract the meson raw yield from the invariant mass distribution, the combinatorial background estimate obtained with the mixed event technique is normalized to the measured invariant mass distribution outside the peak region and then subtracted. The chosen standard normalization range is $0.17 - 0.3\,\text{GeV}/c^2$ for the π^0 and $0.58 - 0.79\,\text{GeV}/c^2$ for the η meson analysis.

The remaining distribution is then fitted with a Gaussian convoluted with an exponential low-energy tail on the left side to account for electron bremsstrahlung and a linear part to describe possible remaining background under the signal peak. The corresponding fit function is:

$$
\begin{aligned}
y = {} & A \cdot \left(G(M_{\gamma\gamma}) + \exp\left(\frac{M_{\gamma\gamma} - M_{\pi^0(\eta)}}{\lambda}\right)(1 - G(M_{\gamma\gamma}))\theta(M_{\gamma\gamma} - M_{\pi^0(\eta)}) \right) \\
& + B + C \cdot M_{\gamma\gamma}
\end{aligned}
$$

$$(3.5)$$

60

$$\text{with } G = \exp\left(-0.5\left(\frac{M_{\gamma\gamma} - M_{\pi^0,\eta}}{\sigma}\right)^2\right)$$

Here G is a Gaussian with the width σ, the amplitude A and the mean position $M_{\pi^0(\eta)}$, which can be identified with the reconstructed mass position of the corresponding meson. The parameter λ represents the inverse slope of the exponential function whose contribution is set to zero by the Heavyside function $\theta(M_{\gamma\gamma} - M_{\pi^0,\eta})$ above $M_{\pi^0(\eta)}$. B and C are the parameters of the linear function. This linear part is especially needed for the η meson reconstruction as the mixed event background estimate is not able to fully reproduce the shape of the same event background. Most likely, this difference is caused by correlations of paired photons that originate from a common particle decay or that are correlated via their common origin in the fragmentation of jets. As the mixed event background is fully uncorrelated it is not able to describe these correlations.

Invariant mass distributions for exemplary p_{T} bins are shown in Fig. 3.11. The raw signal before background subtraction is shown as black line. The red dots represent the signal after subtraction of the complete background, consisting of the mixed event background estimate and the remaining background determined by the linear fit. These two background contributions are also shown in the plot. The fit of the signal peak without the linear part is depicted as blue line. Invariant mass distributions for all analyzed p_{T} bins before and after background subtraction are shown in A.1.

The reconstructed meson mass position and the width of the signal that is also obtained from the fit is shown in Figure 3.12. Since the invariant mass resolution is overestimated in the Monte Carlo production for the π^0 case a Gaussian smearing of the photon momentum is applied for the Monte Carlo sample. The corresponding formulas used for the smearing can be found in Equation 3.6.

$$a = 0.011; \quad b = 0.007$$
$$\alpha = \sqrt{(a)^2 + (b \cdot P_\gamma)^2} \cdot \text{Random.Gaus(0,1)}$$
$$P_{x,\gamma} = (1 + \alpha) \cdot P_\gamma \cdot \sin(\theta) \cdot \cos(\varphi)$$
$$P_{y,\gamma} = (1 + \alpha) \cdot P_\gamma \cdot \sin(\theta) \cdot \sin(\varphi)$$
$$P_{z,\gamma} = (1 + \alpha) \cdot P_\gamma \cdot \cos(\theta) \tag{3.6}$$

Here, $P_{i,\gamma}$ is the i-th component of the resulting smeared photon momentum and P_γ the initially generated photon momentum. For the η meson, the
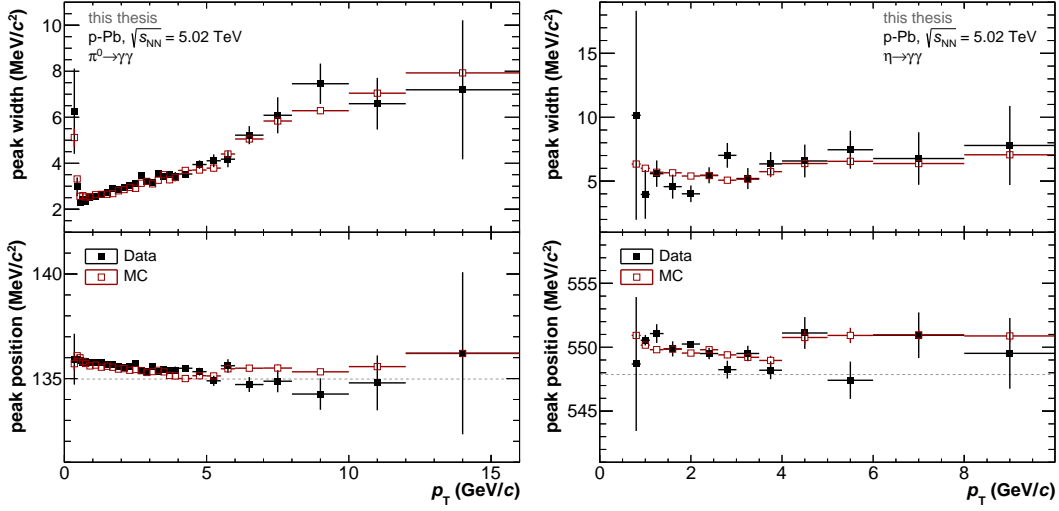
Figure 3.12: Reconstructed π^0 (left) and η (right) peak width and position for the used data and Monte Carlo sample. As the resolution of the π^0 peak is overestimated in the used Monte Carlo productions, an additional smearing is applied.

width of the invariant mass peak is already well described without any smearing. An additional smearing factor would lead to an overestimation of the η width, therefore, no smearing is used for the η analysis. The effect of the smearing on the final meson invariant yield is negligible due to the large integration window of the yield extraction. The reason for the different behavior of the simulations concerning the π^0 and η width is not understood.

For the meson raw yield extraction the signal is integrated within an integration window that is defined by the reconstructed mass position. The chosen integration windows are (M_{π^0} - 0.035 GeV/c^2, M_{π^0} + 0.010 GeV/c^2) for the π^0 and (M_η - 0.047 GeV/c^2, M_η + 0.023 GeV/c^2) for the η meson. The limits of the integration window are illustrated by vertical dashed lines in Fig. 3.11. Asymmetric integration ranges are used to account for the asymmetric peaks which are due to electron bremsstrahlung. The contribution of a possible remaining background is subtracted using the fit parameters of the linear part.

For the π^0 raw yield the resulting formula is:

$$N_{\text{raw}}^{\pi^0} = \int\limits_{M_{\pi^0}-0.035\,\text{GeV}/c^2}^{M_{\pi^0}+0.010\,\text{GeV}/c^2} (N^{\gamma\gamma} - N^{\text{mixed evt. BG}})dM_{\gamma\gamma}$$

$$- \int\limits_{M_{\pi^0}-0.035\,\text{GeV}/c^2}^{M_{\pi^0}+0.010\,\text{GeV}/c^2} (B + C \cdot M_{\gamma\gamma})dM_{\gamma\gamma}$$

(3.7)

The extracted π^0 and η meson p_{T}-differential raw yields for $|y_{\text{lab}}| < 0.8$ normalized to the number of accepted events are presented in Fig. 3.13.
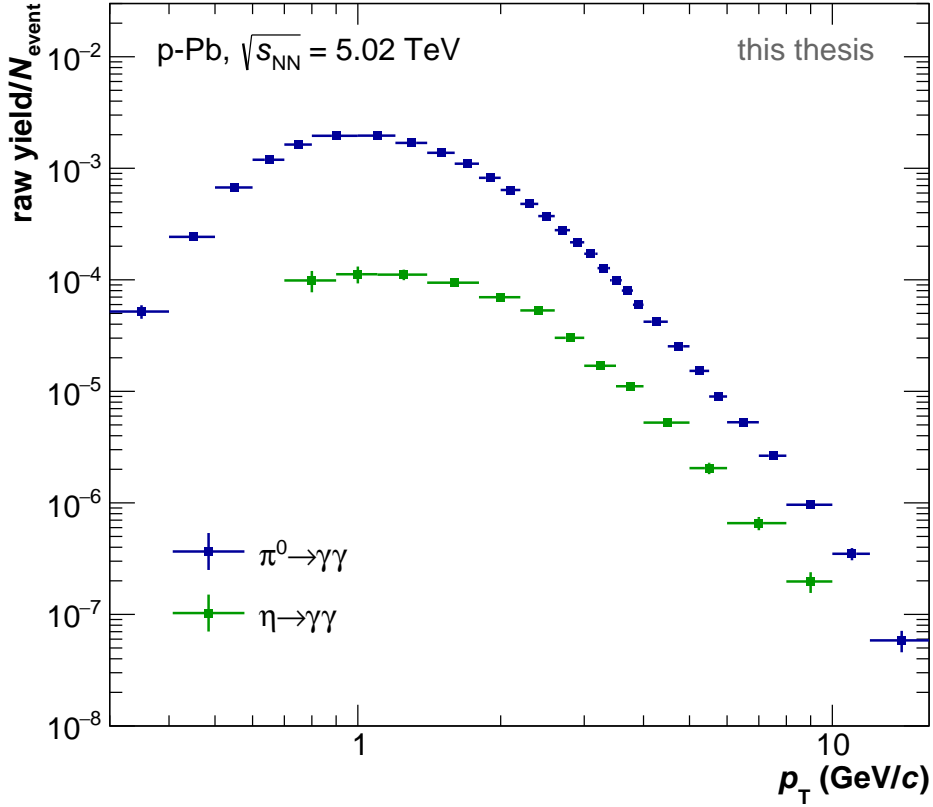
Figure 3.13: Reconstructed π^0 and η p_{T}-differential raw yields in the rapidity range $|y_{\text{lab}}| < 0.8$ normalized per number of accepted events.

3.4 Meson Spectra Corrections

In order to obtain the invariant differential yields from the reconstructed π^0 and η raw spectra, several corrections have to be applied. In the following sections the corrections for secondary mesons (Sec. 3.4.1), efficiency and acceptance (Sec. 3.4.2), out-of-bunch pile-up (Sec. 3.4.3) and finite bin width (Sec. 3.4.4) are discussed.
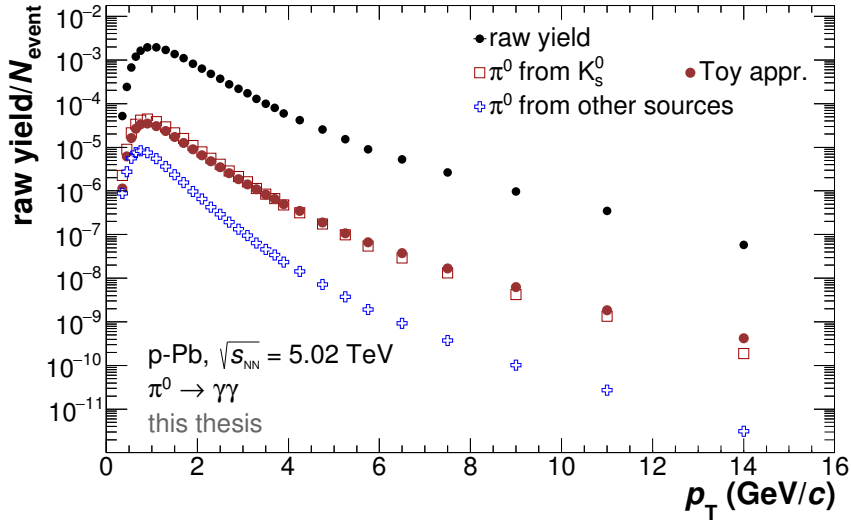
3.4.1 Secondary Correction

Figure 3.14: Measured π^0 raw yield together with the obtained secondary raw yields from the data driven Toy approach and from pure Monte Carlo.

According to the ALICE definition of primary particles [81] a primary π^0 is a π^0, which is either a) produced directly in the primary interaction; or b) from decays of particles with a mean proper lifetime τ smaller than $1\,\mathrm{cm}/c$, excluding particles produced in interactions with the detector material.

Since only primary π^0 may be considered for the invariant yield, secondary neutral pions have to be subtracted from the raw yield. The by far largest part of this contribution originates from feed-down of the decay $K_s^0 \to \pi^0 \pi^0$ with a branching ratio of BR = $30.69 \pm 0.05\%$ [13].

As especially the K_s^0 spectrum is not well reproduced by the event generators employed for the Monte Carlo productions, a data driven approach (Toy approach) is chosen to estimate the secondary contamination. For this,

the measured K_S^0 spectrum [82] is parametrized and the decay is modeled in a full cocktail simulation.

The secondary π^0 yield from K_S^0 decays is calculated in the considered rapidity window of $|y_{lab}| < 0.8$ and afterwards, the secondary π^0 acceptance and efficiency according to the full detector simulation are applied. All other secondary neutral pions originating from decays and interactions with the material are estimated from the analyzed Monte Carlo sample and are in the following referred to as 'from other sources'. The obtained secondary yields are then directly subtracted from the raw yield measured in the analyzed data sample.

In Fig. 3.14 the measured π^0 raw yield is plotted together with the secondary yields obtained with the Toy approach and from pure Monte Carlo. Figure 3.15 shows the ratio of secondaries originating from the respective source X to all measured neutral pions. The contribution of secondaries coming from K_S^0 decays is larger than the contributions from all other sources combined. The comparison between the Monte Carlo estimate and the Toy approach shows that the secondary yield from K_S^0 is overestimated in the Monte Carlo production for $p_T < 4\,\mathrm{GeV}/c$ and underestimated for higher transverse momenta. Therefore, the data driven approach is needed to reproduce the correct shape of the K_S^0 feed-down. The measured η raw yield does not suffer from feed-down as defined above and needs no correction.
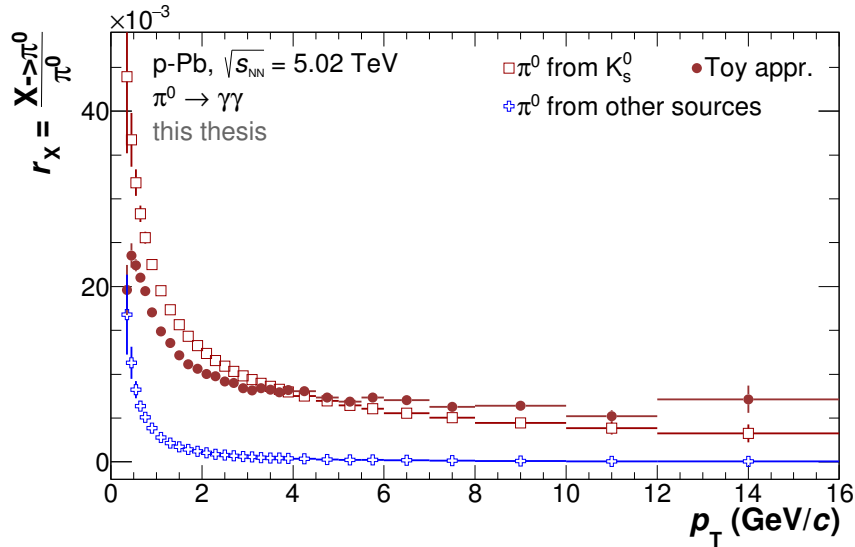

Figure 3.15: Secondary fractions obtained with the Toy approach and pure Monte Carlo approach.

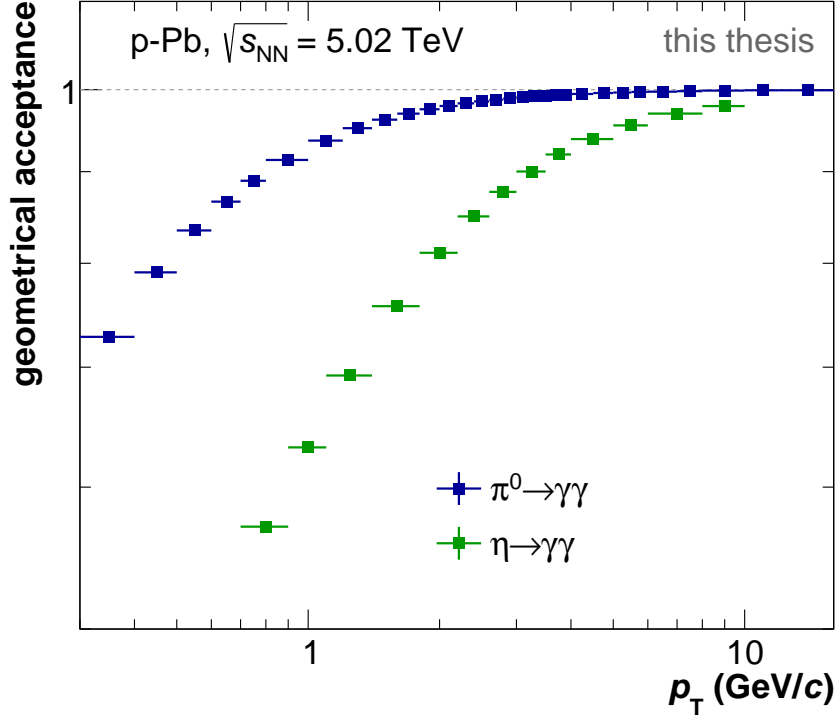### 3.4.2 Efficiency and Acceptance Correction

Figure 3.16: Geometrical acceptance of the π^0 and η meson in p–Pb collisions at $\sqrt{s} = 5.02\,\text{TeV}$.

After the correction for secondary neutral pions, the obtained raw yield has to be corrected for detector acceptance and reconstruction efficiency. For this purpose the Monte Carlo productions described in Sec. 3.1.2 are used. As the shapes of the Monte Carlo spectra do not perfectly reproduce the measured meson spectra, the Monte Carlo spectra are iteratively reweighted to match the data. This is especially needed for the added signals in the HIJING production with their artificial flat p_{T} distribution that is used to enhance the precision of the correction at large transverse momenta which leads to smaller uncertainties in the efficiency correction. HIJING π^0 and η spectra with and without applied weights in comparison with the measured distributions in real data are exemplarily shown in A.2.

The merged minimum bias parts of the HIJING and the DPMJet productions are used for the acceptance determination. The geometrical acceptance $A_{\pi^0(\eta)}$ is defined as the ratio of π^0 (η) mesons within the selected meson rapidity range ($|y_{\text{lab}}| < 0.8$ for the standard cut) with daughter particles

within the photon pseudorapidity range ($|\eta_{\gamma,\mathrm{lab}}| < 0.9$ for the standard cut) over all generated π^0 (η) mesons in this rapidity range.

$$A_{\pi^0(\eta)}(p_\mathrm{T}) = \frac{N_{\pi^0(\eta),|y_{\mathrm{lab}}|<y_{\mathrm{max}},\text{ with the daughter particles within}|\eta_{\gamma,\mathrm{lab}}|<0.9}(p_\mathrm{T})}{N_{\pi^0(\eta),|y_{\mathrm{lab}}|<y_{\mathrm{max}}}(p_\mathrm{T})} \qquad (3.8)$$

The geometrical acceptance for the π^0 and the η meson is shown in Fig. 3.16. Due to the larger mass of the η meson compared to the π^0, the opening angle of the decay photons is larger. This results in a smaller acceptance as it is more likely that one photon lies outside the fiducial detector volume although the meson mother lies inside. As the opening angle gets also smaller for higher transverse momenta, the acceptance increases with p_T and gets close to unity for the π^0 case.

For the determination of the reconstruction efficiency the same analysis as for data is performed for the Monte Carlo sample. The Monte Carlo information is used to verify the V^0 candidates as photons and to check that both photons originate from the same primary π^0 or η mother. In this way contributions from Dalitz decays as well as from secondary neutral pions are rejected. The reconstruction efficiency $\epsilon_{\mathrm{reco},\,\pi^0(\eta)}$ is defined as ratio of the number of true (validated by the Monte Carlo information) primary mesons reconstructed in the Monte Carlo sample and the number of generated primary mesons with daughter particles within the acceptance

$$\epsilon_{\mathrm{reco},\,\pi^0(\eta)}(p_\mathrm{T}) = \frac{N_{\pi^0(\eta)_{\mathrm{true,\,primary}}}(p_\mathrm{T,\,rec})}{N_{\pi^0(\eta)_{\mathrm{primary,\,in\,acceptance}}}(p_\mathrm{T,\,MC})} \qquad (3.9)$$

The efficiency is determined separately for the minimum bias and the added signal part of the Monte Carlo productions and the weighted average of the two efficiencies is taken for the spectra correction. In this way minimum bias efficiencies dominate at low p_T where they have large statistics and the efficiencies reconstructed from the added signals dominate at high p_T where they are more reliable. The reconstruction efficiencies from the minimum bias and the added signal part, as well as the merged result are shown in Fig. 3.17 for both mesons.
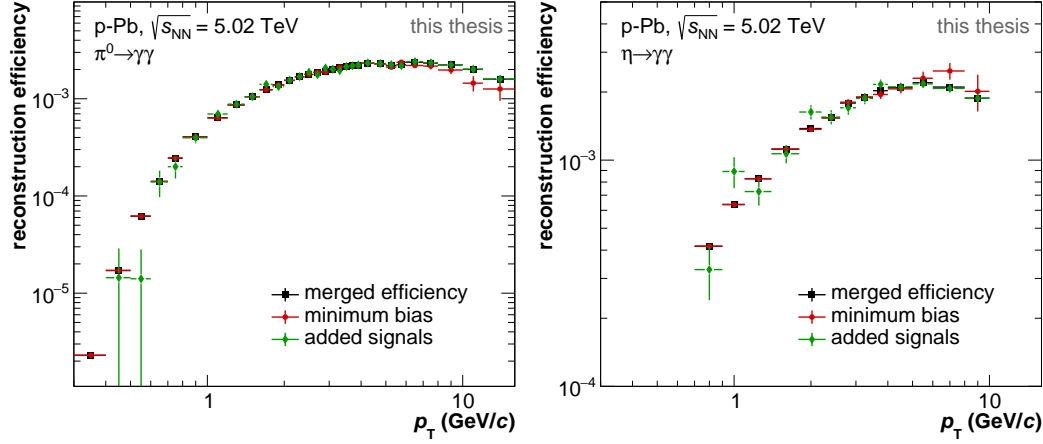
Figure 3.17: Reconstruction efficiencies for π^0 (left) and η meson (right) deduced from the minimum bias and the added signal part of the Monte Carlo productions. The weighted average of the efficiencies, here denoted as 'merged', is used for the correction of the meson spectra.

3.4.3 Out-of-Bunch Pile-up Correction

During the p–Pb data taking period the different LHC bunches had a spacing of 200 ns [83]. For primary tracks that are reconstructed with the SPD whose read-out-time is smaller than 200 ns [52], pile-up from subsequent bunches is negligible. But due to the TPC drift velocity of 2.65 cm/μs which results in a large integration time of 94 μs [53], the PCM measurement is sensitive to so-called out-of-bunch pile-up. Especially for photons whose conversion products are reconstructed with TPC information only, it is possible that they don't originate from the triggered primary collision, but from a pile-up event. This has already been found in previous PCM analyses in pp and Pb–Pb collisions [84].

The common strategy to subtract this pile-up is to identify it by its wide Gaussian shaped DCA$_z$ distribution (distance of closest approach to the primary interaction vertex in z-direction) and estimate its contribution to the meson signal. Figure 3.18 shows two exemplary DCA$_z$ distribution for photons whose conversion products are reconstructed with TPC information only. The pile-up contribution is estimated with fits for different p_T bins for the π^0 (left) and the η meson analysis (right). The pile-up contribution to the meson yields amounts to about 11% for the lowest p_T bin (0.3 GeV/c < p_T < 0.4 GeV/c) and levels out to approximately 2% for higher p_T. The resulting p_T-dependent correction factor for the invariant π^0 yield is shown in Fig. 3.19. Different fitting approaches (method 1 - 6) are made to

estimate the systematic uncertainties resulting from the pile-up correction. For the correction of the standard result method 1 is used.
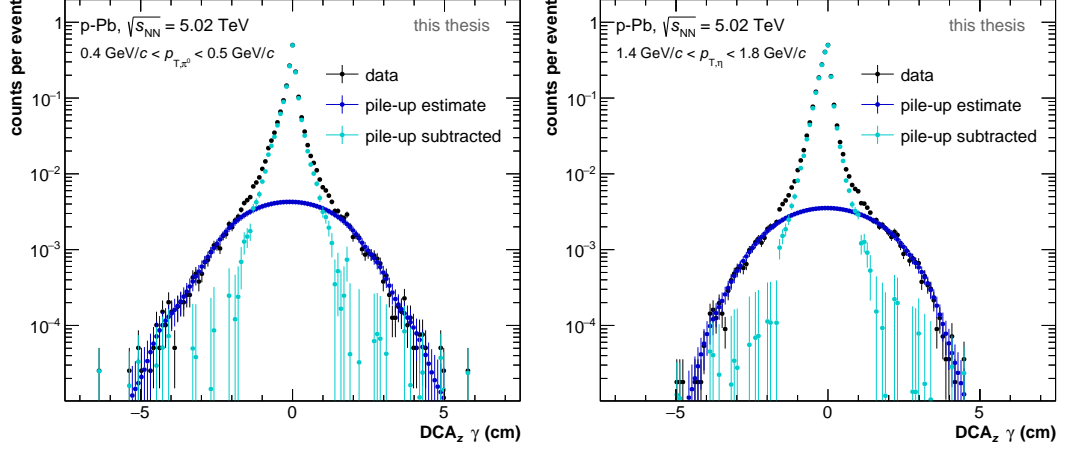

Figure 3.18: Two exemplary DCA_z distributions for converted photons with e^+e^- daughters reconstructed with only TPC information. The pile-up contribution is estimated by fitting the broad DCA_z distribution below the signal peak.

3.4.4 Correction for Finite Bin Width

The fact that neutral mesons cannot be reconstructed in infinitesimal p_T bins leads to the need for a correction for finite bin width [85]. Since the meson spectra are steeply falling with increasing p_T the reconstructed yield of a specific bin does not display the exact value when plotting it at the bin center. To account for that, there are two possibilities: shifting the data points horizontally in p_T so that they lie at the true p_T for the extracted yield (shift in 'x') or shifting the points vertically so that the true yield is obtained for the bin center (shift in 'y'). The horizontal shift in p_T is used to present the invariant meson yields, while shifting the yields in y-direction is usually performed for ratios like the η/π^0 ratio or the R_{pA}, see Chap. 4, as a shift in x would lead to a different binning of numerator and denominator.

For both approaches a parametrization of the measured invariant yield is needed to approximate the underlying spectral shape. For example, a Tsallis fit [86] of the following form provides a good description of the neutral meson spectra:

$$\frac{1}{2\pi N_{ev}} \frac{d^2 N}{p_T dp_T dy} = \frac{A}{2\pi} \cdot \frac{(n-1)(n-2)}{nT(nT + M(n-2))} \left(1 + \frac{m_T - M}{nT}\right)^{-n} , \quad (3.10)$$
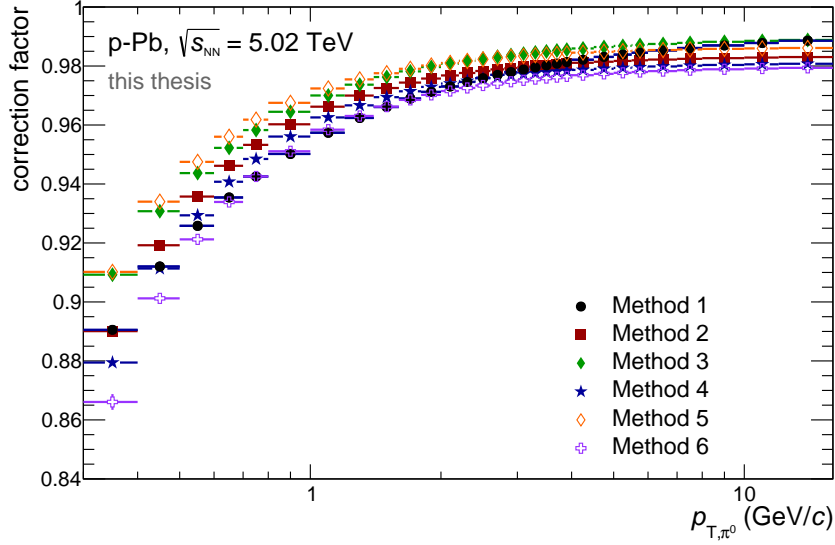
Figure 3.19: Pile-up correction factor for the invariant π^0 yield estimated with different fitting approaches to the DCA_z distributions. The correction factor obtained with method 1 is used for the correction.

with M as mass of the measured meson, the transverse mass $m_\mathrm{T} = \sqrt{M^2 + p_\mathrm{T}^2}$, and A, n and T as fitting parameters.

Another possibility is the so-called two component model (TCM) fit [87]:

$$\frac{1}{2\pi N_\mathrm{ev}} \frac{\mathrm{d}^2 N}{p_\mathrm{T} \mathrm{d} p_\mathrm{T} \mathrm{d} y} = A_\mathrm{e} \exp\left(-E_\mathrm{T,kin}/T_\mathrm{e}\right) + A\left(1 + \frac{p_\mathrm{T}^2}{T^2 n}\right)^{-n} \tag{3.11}$$

Here, $E_\mathrm{T,kin} = \sqrt{p_\mathrm{T}^2 + M^2} - M$ is the transverse kinematic energy of the meson with the mass M, A_e and A are normalization factors and T_e, T, and n are free parameters. As indicated in the name, the TCM fit consist of two components to simultaneously describe the low p_T part of the spectrum as well as the high p_T part. In case of the π^0 this fit is well suited to describe the spectral shape over the whole p_T range. As the η measurement starts at a higher p_T, the TCM fit cannot be sufficiently constrained at low p_T. Thus the Tsallis fit is preferable in this case.

If meson yields measured with different methods are combined (see Sect. 4.2), the correction is based on the fit to the combined result and applied to the individual yields. In this way, the common binning of the different analyses is preserved. In addition, the fit to the combined yield gives a better assumption of the underlying spectral shape than fits to individual measurements.

70

3.5 Systematic Error Evaluation

In this section the different sources of systematic uncertainties of the invariant meson yields and their evaluation are discussed.

For the reconstruction of converted photons the exact knowledge of the conversion probability and therefore of the material budget of the ALICE detector is crucial. The material budget has been studied in detail with the PCM method [88]. The uncertainty due to the mismatch between simulation and experiment was found to be 9% for two converted photons for all transverse momenta and hence the dominant uncertainty source except for the highest and lowest p_T bins. The variation of the analyzed (pseudo)rapidity range and the choice of different event generators is already contained in the material budget uncertainty.
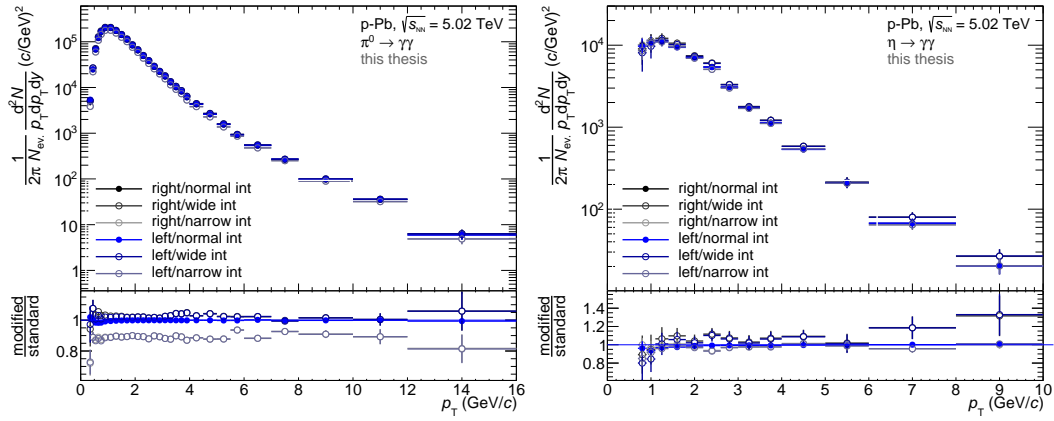

Figure 3.20: π^0 and η meson raw yields for different background normalization and signal integration windows.

The uncertainty of the yield extraction process is estimated by varying the normalization region for the mixed event background and the limits of the signal integration window. For the normalization of the mixed event background estimate two different normalization windows are used. One at high invariant masses, located at the right side of the meson peak - which is also the standard normalization window - and one at lower invariant masses, thus at the left side of the meson peak. In addition to the standard signal integration window, also a narrower and a wider integration window is used for the uncertainty estimation. The limits of the normalization and integration regions for both neutral mesons are listed in Tab. 3.7. The meson raw yields obtained for the different normalization and integration windows are shown in Fig. 3.20. The mean of the positive and negative deviation from

	π^0	η
right	$170\,\mathrm{MeV}/c^2$; $300\,\mathrm{MeV}/c^2$	$580\,\mathrm{MeV}/c^2$; $790\,\mathrm{MeV}/c^2$
left	$50\,\mathrm{MeV}/c^2$; $80\,\mathrm{MeV}/c^2$	$350\,\mathrm{MeV}/c^2$; $480\,\mathrm{MeV}/c^2$
normal int.	M - $35\,\mathrm{MeV}/c^2$; M + $10\,\mathrm{MeV}/c^2$	M - $36\,\mathrm{MeV}/c^2$; M + $18\,\mathrm{MeV}/c^2$
wide int.	M - $55\,\mathrm{MeV}/c^2$; M + $25\,\mathrm{MeV}/c^2$	M - $68\,\mathrm{MeV}/c^2$; M + $32\,\mathrm{MeV}/c^2$
narrow int.	M - $15\,\mathrm{MeV}/c^2$; M + $5\,\mathrm{MeV}/c^2$	M - $33\,\mathrm{MeV}/c^2$; M + $12\,\mathrm{MeV}/c^2$

Table 3.7: Limits of the right and left normalization window for the mixed event background estimate and of the three different signal integration windows used for the systematic uncertainty evaluation of the yield extraction. M denotes here the reconstructed meson mass.

the standard result in each p_T bin gives the final systematic uncertainty for the yield extraction.

In the unrealistic case of a Monte Carlo simulation that perfectly describes the analyzed data sample, the choice of the selection criteria would not influence the extracted meson yield as changes in the meson raw yield would be exactly counterbalanced by the reconstruction efficiency. For an imperfect Monte Carlo sample every selection criterion bears the risk to affect the data and Monte Carlo sample differently and can thus introduce a bias. To estimate the systematic uncertainties resulting from a possible mismatch of data and Monte Carlo production, the used selection criteria for the track, electron, photon and meson reconstruction are varied. The cut variations that are performed for the systematic error calculation are listed in Table 3.8. If possible, each selection criterion is varied at least twice, once to a stricter and once to a more relaxed selection compared to the standard cut. Only one selection criterion is varied at a time and the deviation to the standard result is calculated for each p_T bin. The average of the maximum deviation in positive and negative direction is taken as the systematic error for this particular cut variation in the corresponding p_T bin. For most cuts, this leads to bin-to-bin fluctuations which are mainly dominated by statistical fluctuations. To suppress these fluctuations, all systematic uncertainties are smoothed partially or completely with a polynomial or exponential fit.

Figure 3.21 and Fig. 3.22 show the systematic uncertainties of the π^0 and η analysis. The final total systematic uncertainty is the quadratic sum of all

contributing uncertainties and is plotted in black. For a better overview the single contributions are summarized into groups:

Signal Extraction

This category summarizes all uncertainties concerning the extraction of the meson signal. In addition to the yield extraction uncertainty that has been described above, also uncertainties estimated by the variation of the background scheme and the so-called α meson cut are included here. For the mixed event background the multiplicity estimate is changed from the V^0 multiplicity to charged track multiplicity. With the α meson cut, photon pairs with an asymmetric energy distribution can be rejected. It is defined as $\alpha = \frac{E_{\gamma 1} - E_{\gamma 2}}{E_{\gamma 1} + E_{\gamma 2}}$, with $E_{\gamma i}$ as photon energy. For the standard analysis this selection is not applied. For cross-checks the cut is tighten so that photon pairs with $|\alpha| > 0.8$ are rejected. Besides the material budget, the signal extraction is one of the largest uncertainty sources of the neutral meson analysis.

Track Reconstruction

All cut variations concerning the charged particle track and V^0 selection are grouped in this category. This includes the single p_{T} cut and the number of TPC clusters. Also the requirements on the pointing of the V^0 momentum vector to the primary vertex is varied and the resulting systematic uncertainty is added in quadrature to the track reconstruction uncertainty. The systematic uncertainties originating from the choice of the fiducial detector volume (η and R_{min} cut) are included in the uncertainty on the material budget.

Electron PID

For the estimation of the electron PID uncertainty, the cuts on the TPC dE/dx with respect to the electron and pion hypothesis are varied. Due to the various selection possibilities the dE/dx electron cut is varied three times and the dE/dx pion cut even six times.

Photon Reconstruction

The photon reconstruction uncertainty contains the uncertainties estimated by varying the χ^2_γ, ψ_{pair} and q_{T} cuts. For the two-dimensional χ^2_γ-ψ_{pair} cut the values are varied separately and also the one-dimensional versions of the cuts
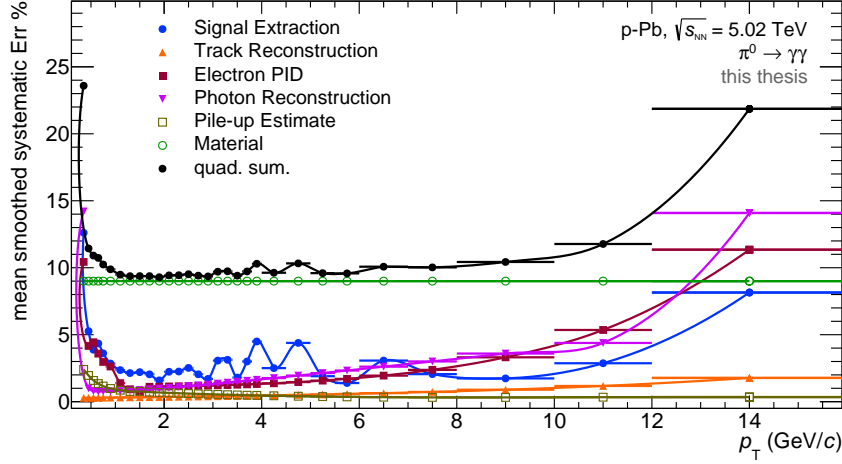
Figure 3.21: Systematic uncertainties of the π^0 analysis summarized in groups. All uncertainties, except for the yield extraction, have completely or partially been smoothed with a polynomial or an exponential function to suppress statistical fluctuations. The quadratic sum of all uncertainties including the material budget error is shown in black.

are analyzed as cross-check. Also for the q_T cut the two- and one-dimensional variants are used for the cut variation.

Pile-up Estimate

The uncertainty of the pile-up correction factor is estimated by varying the fits of the DCA_z distributions. The uncertainty amounts to approximately 2.5% for the lowest p_T bin of the π^0 analysis and then decreases with p_T.

Material

As already mentioned the material budget uncertainty is p_T independent and with 9% for two converted photons the largest error source.

As many systematics are common for the π^0 and the η analysis they partially cancel out in the η/π^0 ratio (see Chap. 4). The systematic uncertainties are therefore directly evaluated on the ratio. They are plotted in the right panel of Fig. 3.22. As the material budget uncertainty is the same for both mesons, it even completely cancels for the ratio. A more detailed overview of all systematic uncertainty components is given in A.3.
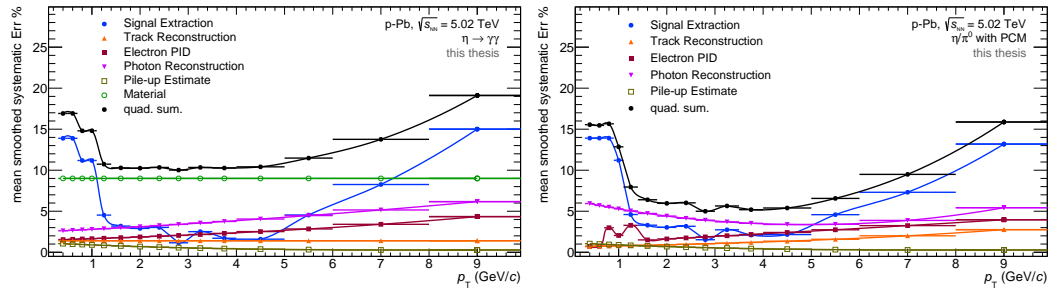
Figure 3.22: Systematic uncertainties of the η analysis (left) and the η/π^0 ratio (right) summarized in groups. All uncertainties, except for the yield extraction, have completely or partially been smoothed with a polynomial or an exponential function to suppress statistical fluctuations. The quadratic sum of all uncertainties is shown in black. In case of the η/π^0 ratio the material budget uncertainty completely cancels out.

Selection Criterion	Standard	Variation 1	Variation 2	Variation 3
single p_T $e^{\pm}$	$> 0.05\,\mathrm{GeV}/c$	$> 0.0\,\mathrm{GeV}/c$	$> 0.1\,\mathrm{GeV}/c$	
min TPC clust./ find. clust.	> 0.6	> 0.35	> 0.7	
$\cos(\theta_{\mathbf{point}})$	> 0.85	> 0.75	> 0.9	
dE/dx e-line $\sigma_{\mathrm{d}E/\mathrm{d}x,e}$	$-4 < \sigma < 5$	$-3 < \sigma < 5$	$-2.5 < \sigma < 4$	$-5 < \sigma < 5$
dE/dx π-line π rej. low p $\sigma_{\mathrm{d}E/\mathrm{d}x,\pi}$	< 1	< 2	< 2	< 1
π rej. high p $\sigma_{\mathrm{d}E/\mathrm{d}x,\pi}$	< -10	< -10	< -10	< -10
$p_{\min,\,\pi\,\mathrm{rej}}$	$0.4\,\mathrm{GeV}/c$	$0.4\,\mathrm{GeV}/c$	$0.4\,\mathrm{GeV}/c$	$0.5\,\mathrm{GeV}/c$
$p_{\max,\,\pi\,\mathrm{rej}}$	$100\,\mathrm{GeV}/c$	$100\,\mathrm{GeV}/c$	$3.5\,\mathrm{GeV}/c$	$100\,\mathrm{GeV}/c$
dE/dx π-line π rej. low p $\sigma_{\mathrm{d}E/\mathrm{d}x,\pi}$	(cont.)	< 1	< 1	< 1
π rej. high p $\sigma_{\mathrm{d}E/\mathrm{d}x,\pi}$		< -10	< -10	< -10
$p_{\min,\,\pi\,\mathrm{rej}}$		$0.3\,\mathrm{GeV}/c$	$0.4\,\mathrm{GeV}/c$	$0.25\,\mathrm{GeV}/c$
$p_{\max,\,\pi\,\mathrm{rej}}$		$100\,\mathrm{GeV}/c$	$3.5\,\mathrm{GeV}/c$	$100\,\mathrm{GeV}/c$
χ^2_{γ}	< 30 (2D)	< 30 (1D)	< 50 (2D)	< 20 (2D)
$\psi_{\mathbf{pair}}$	< 0.1 (2D)	< 0.1 (1D)	< 0.2 (1D)	< 0.05 (2D)
$q_{\mathbf{T,max}}$	$< 0.05\,\mathrm{GeV}/c$ (2D)	$< 0.05\,\mathrm{GeV}/c$ (1D)	$< 0.03\,\mathrm{GeV}/c$ (2D)	$< 0.07\,\mathrm{GeV}/c$ (1D)
α meson	0. - 1.	0. - 0.8		
background	V^0 multiplicity	track multiplicity		

Table 3.8: Variations of the selection criteria for the systematic error evaluation of the neutral meson analyses.

3.6 Multiplicity Dependent Analysis

In addition to the minimum bias analysis, the π^0 and η mesons are also reconstructed for different multiplicity classes. As multiplicity estimator the total charge deposited in the V0A detector is used. In contrast to Pb–Pb collisions, where there is a strong correlation between measured multiplicity and N_{part} as well as between N_{part} and impact parameter b, these correlations are much weaker in p–Pb collisions [89]. In this way it is not possible to define centrality classes from the measured V0A multiplicity without a bias. That is why in the following it will only be referred to as multiplicity classes instead of centrality classes.

Nevertheless, event multiplicity classes are interesting to study since they are related to the system size and the initial energy density. Even with a possible bias that may shift the measured spectra by a constant factor, the influence of the system size on the spectral shape can be investigated.

For the meson analysis, the data sample is divided into four different multiplicity classes: 0-20%, 20-40%, 40-60%, and 60-100%. The number of accepted events for each multiplicity class is given in Tab. 3.9.

	Sample	$\sqrt{s_{NN}}$	Multiplicity	accepted Events
Data	LHC13b & LHC13c	5.02 TeV	0-20%	$20.1 \cdot 10^6$
			20-40%	$20.3 \cdot 10^6$
			40-60%	$20.4 \cdot 10^6$
			60-100%	$38.8 \cdot 10^6$

Table 3.9: Number of p–Pb events passing the event selection for the different multiplicity classes.

The photon and meson reconstruction is basically the same for the minimum bias case and all multiplicity classes. The few adaptions made for the multiplicity studies are described in the following.

As the statistics are reduced for the multiplicity classes a wider binning in p_{T} than for the minimum bias analysis is used for the reconstruction. As it can be seen in Fig. 3.23 the reconstruction efficiency is independent of the analyzed multiplicity class. The observed differences especially at high p_{T}

are only of statistical nature due to the limited Monte Carlo statistics for the multiplicity classes. Therefore, the minimum bias efficiencies are also used for the correction of the multiplicity spectra.
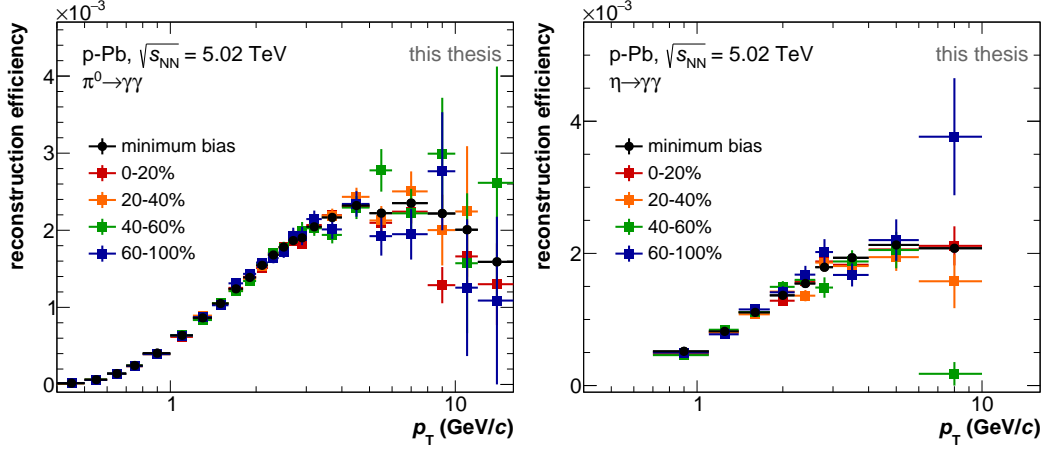

Figure 3.23: Reconstruction efficiencies for π^0 (left) and η meson (right) for different multiplicity classes. The minimum bias efficiencies are used for the correction of all multiplicity spectra

The out-of-bunch pile-up correction factors are evaluated separately for all analyzed multiplicity classes. Due to the lower activity and thus smaller meson numbers in the events the relative pile-up contamination is larger for lower multiplicities, see Fig. 3.24.
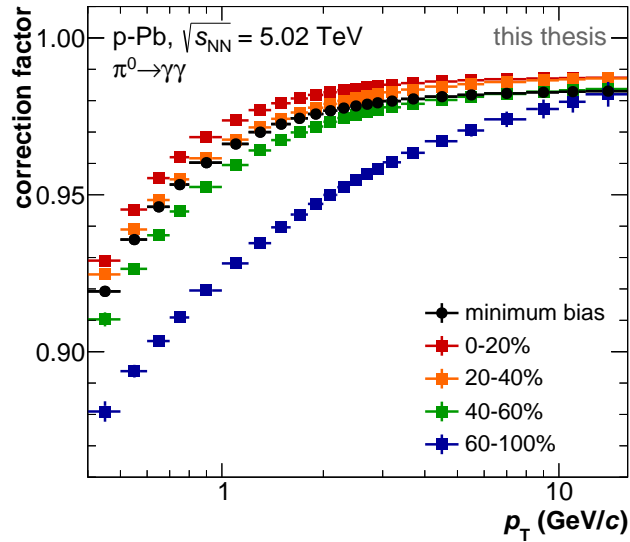
Figure 3.24: Out-of-bunch pile-up correction factors for different multiplicity classes for the π^0 analysis.

The systematic uncertainties originating from the yield extraction and the pile-up estimate are evaluated separately for each multiplicity class. As the multiplicity in p–Pb collisions rarely exceeds 100 TPC tracks, see Fig. 3.25, - compared to up to 20 000 tracks in Pb–Pb collisions - detector effects due to a large occupancy are not expected in p–Pb. All remaining systematic uncertainties are therefore regarded as multiplicity independent and the minimum bias uncertainties are applied. This assumption is also supported by the multiplicity independence of the reconstruction efficiency.
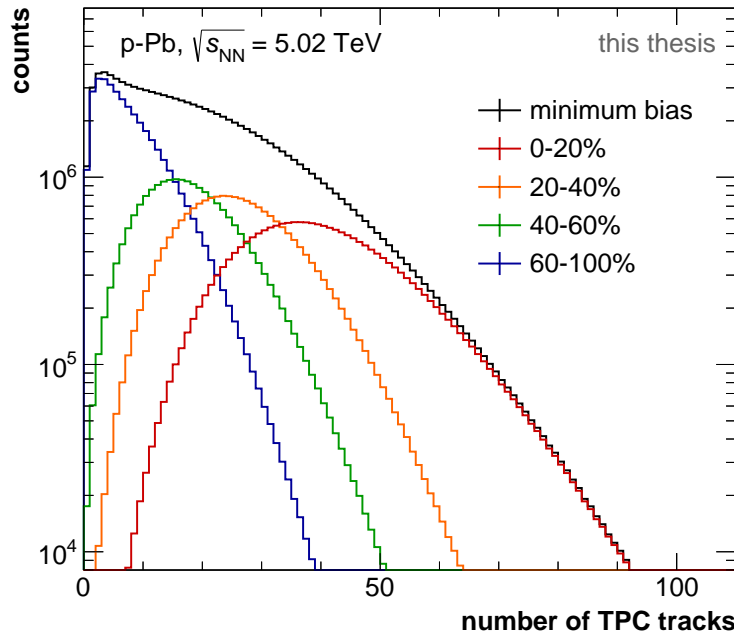
Figure 3.25: Number of charged TPC tracks for the different multiplicity classes.

Chapter 4

Results

In the following chapter, the reconstructed meson yields and deduced properties like the η/π^0 ratio and nuclear modification factors will be presented and discussed. Section 4.1 concentrates on the results of the presented analysis using photon conversions. The minimum bias PCM analysis serves as input for the ALICE neutral meson result published in [90], which is presented in Sec. 4.2. Comparisons between the combined ALICE results and theoretical models are made in Sec. 4.3.

4.1 Photon Conversion Method

In this section the results of the PCM analysis for minimum bias and the different V0A multiplicity bins are presented. It has to be noted that all yields and derived quantities are shown without a correction for finite bin width. Thus, the shown values have to be interpreted as the average value of the presented bin and not as the exact value at the given bin center. For the combined ALICE result (see Sec. 4.2) the bin width correction is applied using the Tsallis fit to the combined result.

4.1.1 Minimum Bias Results

Invariant Differential Yields

The reconstructed invariant differential π^0 and η yields are shown in Fig. 4.1. The statistical uncertainties are represented as vertical error bars, partially covered by the markers, while the systematic uncertainties are given by the light gray boxes. The horizontal error bars show the width of the respective bin. The yields are normalized to the number of accepted minimum bias

events. Fits to the particle yields, with statistical and systematic uncertainties added in quadrature, are also plotted. For the π^0 the TCM fit (Eq. 3.11) is used, the η yield is fitted with a Tsallis function (Eq. 3.10). The corresponding fit parameters can be found in Tab. 4.1.
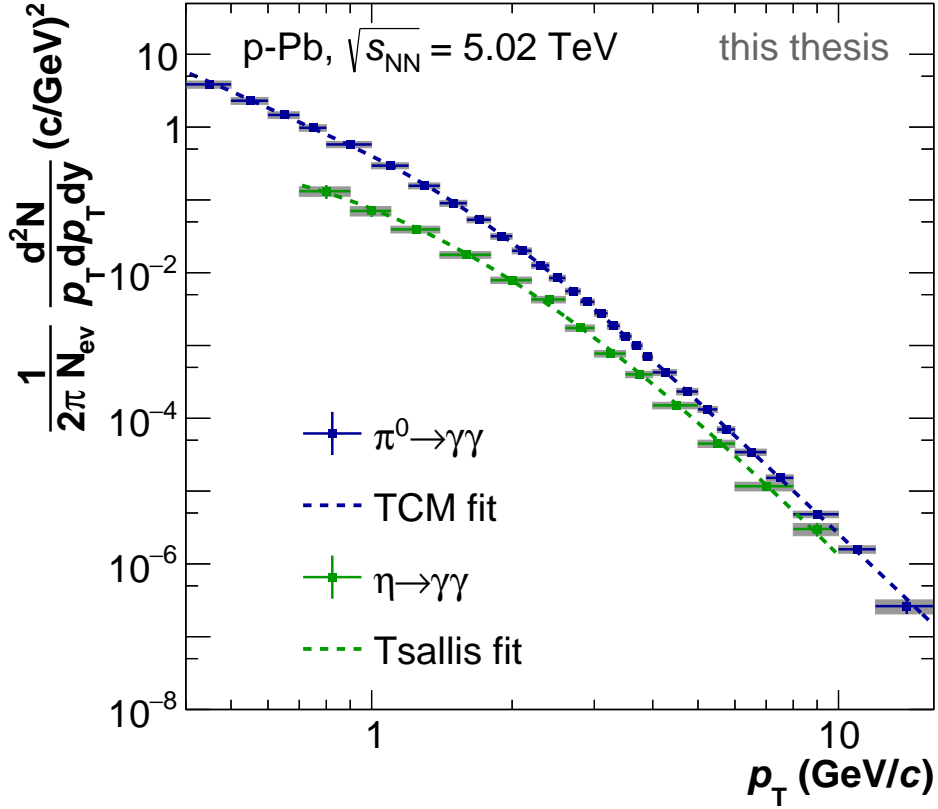

Figure 4.1: Invariant differential π^0 and η yields measured with PCM in minimum bias p–Pb collisions at $\sqrt{s_{NN}}$ = 5.02 TeV. Statistical uncertainties are represented by vertical error bars, systematic uncertainties by the gray boxes. Fits to the meson yields are also shown.

η/π^0 Ratio

In addition to the individual meson yields, also the ratio of η and π^0 is of interest as the influence of the different quark content on the fragmentation can be studied. For this purpose the π^0 is supplementally reconstructed in the same binning as the η meson. As described in Sec. 3.5 common systematics like the material budget cancel in the η/π^0 ratio presented in Fig. 4.2. The ratio increases with p_T and levels out to a constant value of about 0.45 - 0.5 for $p_T > 4\,\mathrm{GeV}/c$.

TCM Parameters	π^0	Tsallis Parameters	η
A_e (GeV$^{-2}c^2$)	50.67 ± 68.88		
T_e (GeV/c)	0.113 ± 0.061		
A (GeV$^{-2}c^2$)	2.57 ± 2.02	A	0.94 ± 0.24
T (GeV/c)	0.614 ± 0.19	T (GeV/c)	0.267 ± 0.063
n	3.09 ± 0.16	n	7.29 ± 1.56
χ^2/NDF	0.018	χ^2/NDF	0.049

Table 4.1: Fitting parameters of the two-component model fit to the π^0 invariant differential yield and of the Tsallis fit to the η invariant differential yield.
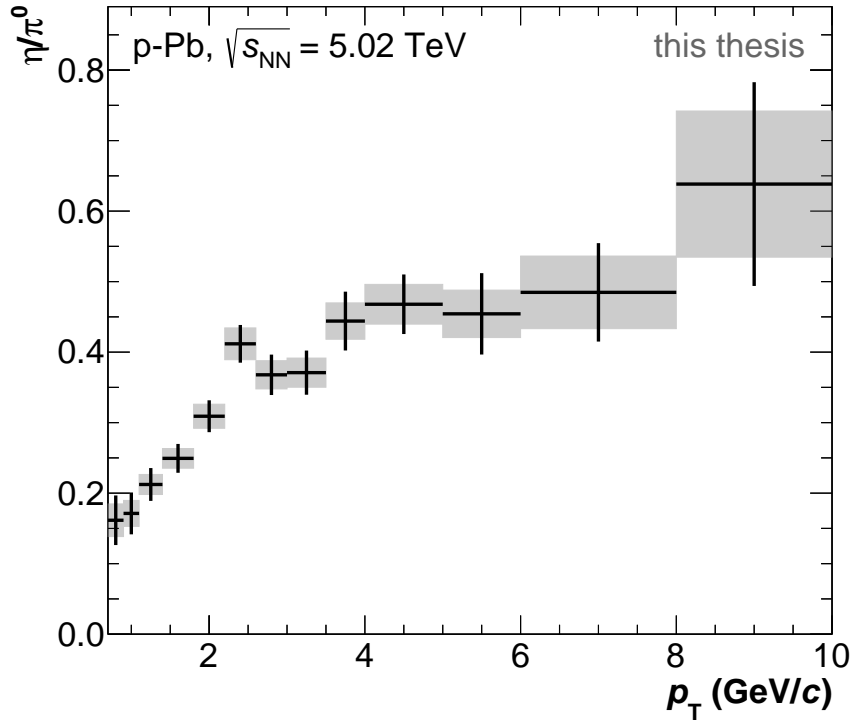
Figure 4.2: η/π^0 ratio versus p_T measured in minimum bias p–Pb collisions at $\sqrt{s_{NN}} = 5.02$ TeV with PCM. Statistical uncertainties are represented by vertical error bars, systematic uncertainties by the gray boxes.

Nuclear Modification Factor

The nuclear modification factor R_{pPb} is defined as the ratio of the measured meson yield in p–Pb and the respective pp cross section at the same collision energy, scaled with the nuclear overlap function $\langle T_{pPb} \rangle = 0.0983 \pm 0.0035$ mb^{-1} [91, 92]:

$$R_{pPb}(p_T) = \frac{\mathrm{d}^2 N_{\pi^0,\eta}^{pPb}/\mathrm{d}y\mathrm{d}p_T}{\langle T_{pPb} \rangle \mathrm{d}^2 \sigma_{\pi^0,\eta}^{pp}/\mathrm{d}y\mathrm{d}p_T} \qquad (4.1)$$

In the absence of nuclear effects a p–Pb collision can be interpreted as a superposition of pp collisions and the nuclear modification factor is expected to be consistent with unity for $p_T > 2\,\mathrm{GeV}/c$. For lower transverse momenta N_{coll} scaling is not fulfilled and the R_{pPb} can deviate from one.

As the π^0 and η pp cross sections at $\sqrt{s} = 5.02$ TeV are not reconstructed so far, a pp reference is constructed from the existing pp measurements at $\sqrt{s} = 2.76$ TeV [1, 93], $\sqrt{s} = 7$ TeV [94] and $\sqrt{s} = 8$ TeV [95] via interpolation. In order to be able to cancel out the common material budget uncertainty in the R_{pPb}, only the PCM contributions to the published spectra are used for the interpolation process. As the out-of-bunch pile-up (see Sec. 3.4.3) was not known at the time of the 7 TeV reconstruction, only data points above 1 GeV/c are considered for the interpolation process. The pile-up contribution for this data set was estimated retrospectively and was found to be smaller than 3% for $p_T > 1\,\mathrm{GeV}/c$ and well covered by the systematic uncertainties. Below 1 GeV/c the interpolation is solely based on the 2.76 and 8 TeV input which is fully corrected for pile-up.

In order to obtain a common binning, the pp cross sections at the different energies are fitted and then reevaluated in the same binning as used for the p–Pb analysis. In case of the π^0 a two component model (TCM) fit is used. Due to the limited p_T reach of the η reconstruction, the Tsallis fit gives a better parametrization and is thus used for this case.

For the new extracted binning the systematic uncertainty for each bin is calculated as average uncertainty of adjacent bins in the original binning. The statistical uncertainties of the parametrized spectra are computed from the fits to the measured spectra with only statistical errors. Once all cross sections are available in the same binning, the 5.02 TeV pp reference is calculated as
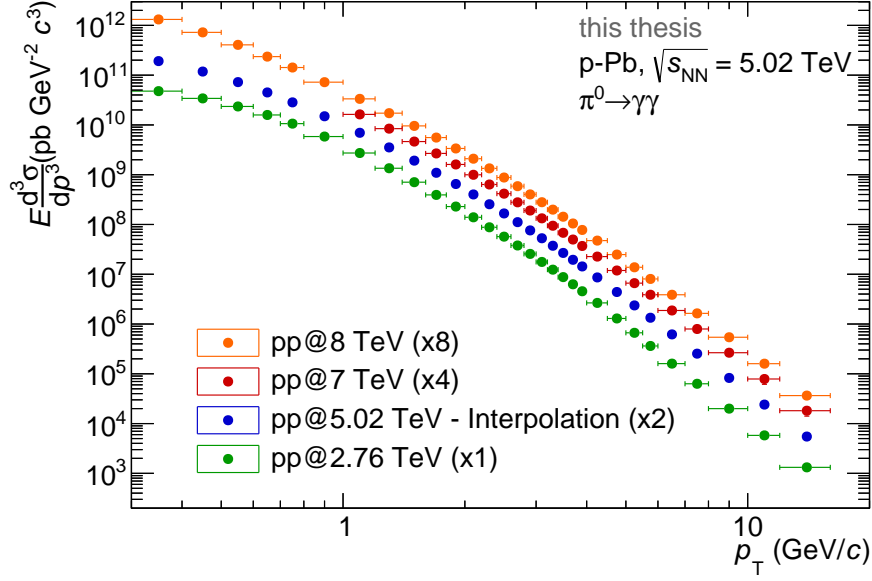
Figure 4.3: Interpolated π^0 cross section at $\sqrt{s}$ = 5.02 TeV (blue dots) together with the cross sections at 2.76, 7 and 8 TeV that are used as input for the interpolation. All cross sections are shown in the p–Pb binning. The 7 TeV spectrum is only considered from 1 GeV/c on, due to a remaining contamination from out-of-bunch pile-up that is not negligible for lower p_T.

interpolation by assuming a power-law behavior for the evolution of the cross section in each p_T bin as a function of $\sqrt{s}$ [28]:

$$\mathrm{d}^2\sigma(\sqrt{s})/\mathrm{d}y\mathrm{d}p_T \propto \sqrt{s}^{\alpha(p_T)} \tag{4.2}$$

This assumption has been validated by PYTHIA 8.21 events [68] at 2.76, 5.02, 7 and 8 TeV, where the difference between the interpolated and the simulated reference is negligible [90]. The interpolated π^0 pp cross section at $\sqrt{s}$ = 5.02 TeV together with the rebinned cross sections at 2.76, 7 and 8 TeV are shown in Fig. 4.3. The statistical and systematic uncertainties of the interpolated pp reference are estimated as follows. For each p_T bin, the systematic uncertainty of the interpolated spectrum is estimated by the largest uncertainty among the input spectra used for the interpolation process. The statistical error is obtained from the power-law fit.

In principle, one needs the p–Pb and pp spectra measured in the same rapidity range for the construction of the R_{pPb}. Due to the rapidity shift in p–Pb collisions, this would only be possible if one restricts the measurement in both systems to about half the detector volume, which would drastically
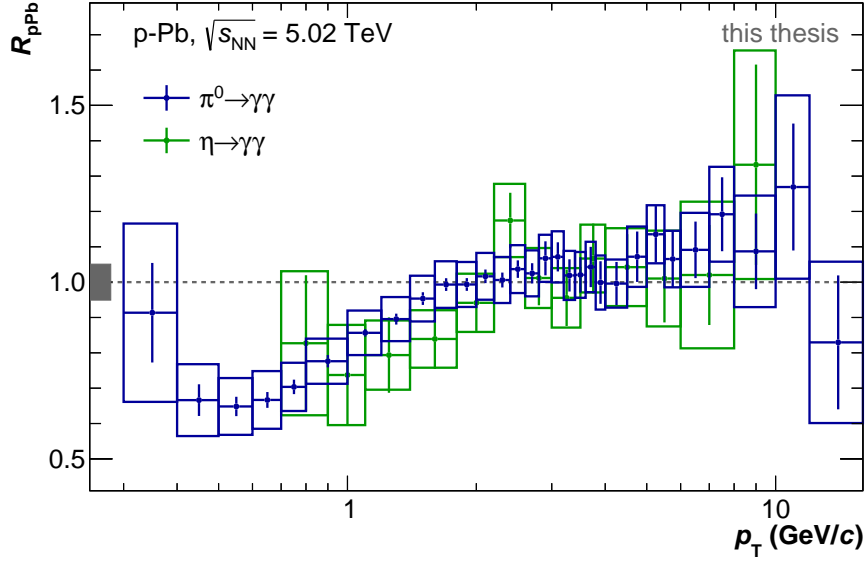
Figure 4.4: Nuclear modification factors for both neutral mesons, measured via photon conversions. Statistical uncertainties are given as vertical error bars, systematic uncertainties are represented as boxes. The overall normalization uncertainty is shown as gray error box around unity.

reduce the statistics. As the pseudorapidity density in p–Pb collisions at $\sqrt{s_{NN}} = 5.02$ TeV [91] and in pp collisions from 0.9 to 7 TeV [96] is flat in the concerning region, the difference caused by the rapidity shift is expected to be very small. This is confirmed by PYTHIA 8.21 simulations in pp collisions at $\sqrt{s} = 5.02$ TeV at $y_{cms} = 0$ and $y_{cms} = -0.465$, where the differences are found to be of the order of 0.5% for $p_T < 1$ GeV/c and 1% for $p_T > 1$ GeV/c [90]. The π^0 and η pp reference spectra are corrected for the rapidity difference using the PYTHIA simulation.

The π^0 and η meson nuclear modification factors that are reconstructed from the measured PCM p–Pb meson spectra and the interpolated PCM pp references are shown in Fig. 4.4. Statistical uncertainties are given as vertical error bars, systematic uncertainties are represented as boxes. As the material budget uncertainty is the same in pp and p–Pb collisions, it is canceled out in the ratio. The overall normalization uncertainty including the uncertainty of $\langle T_{pPb} \rangle$ and of the pp cross section amounts to about 5% and is given as gray error box around unity.

The nuclear modification factors for both mesons agree with each other. For $p_T > 2$ GeV/c the values of R_{pPb} are consistent with unity within the uncertainties. A nuclear modification due to the presence of the lead nucleus cannot be observed.

4.1.2 Multiplicity Dependent Results

In this section, the results of the multiplicity dependent analysis (see Sec. 3.6) are presented. For a better comparison, the minimum bias spectra, which are by default analyzed in a finer p_T binning, have been reanalyzed in the wider binning used for the multiplicity dependent analysis.
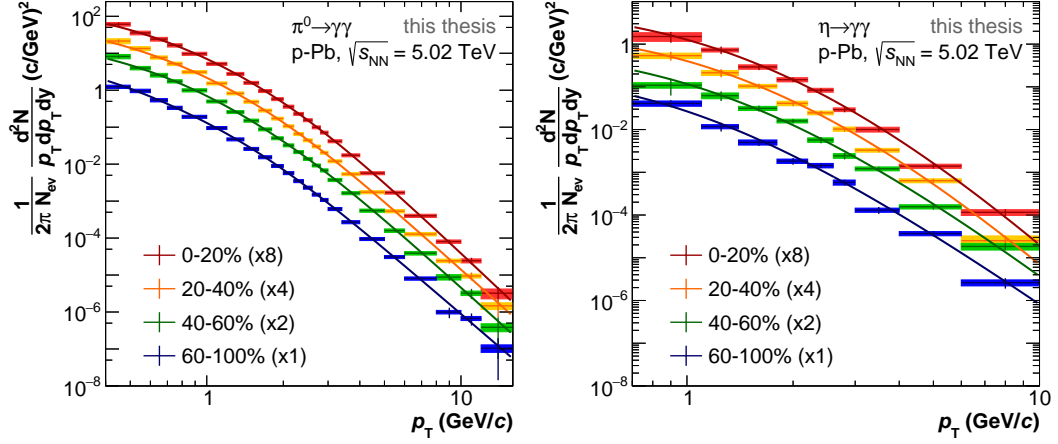

Figure 4.5: π^0 (left) and η (right) invariant differential yields for different V0A multiplicities. Statistical uncertainties are represented as vertical error bars, systematic uncertainties are given as boxes. TCM fits to the π^0 yields and Tsallis fits to the η yields are also shown.

Figure 4.5 shows the invariant differential yields for the π^0 (left) and the η meson (right) for all analyzed multiplicity bins. For a better visibility, the spectra are scaled with a factor 2^n. Statistical uncertainties are represented as vertical error bars and the systematic uncertainties are given as boxes in a lighter color than used for the data points. Fits to the invariant differential meson yields with total uncertainties are also shown. For the π^0 the TCM fit is used, the η yields are fitted with a Tsallis function. The obtained fitting parameters are given in Tab. 4.2 and Tab. 4.3, respectively.

A hardening of the spectra with increasing multiplicity, which would translate into decreasing values of fit parameter n, as it has been observed for charged hadrons [82], especially for the heavier protons and lambdas, cannot be observed for the measured neutral mesons. The large uncertainties of the measurements lead to large uncertainties of the fit parameters. Therefore, the fit values do not allow for a physics interpretation and only serve as an appropriate parametrization of the different spectra. The small values of the reduced χ^2 can also be explained by the large uncertainties which are partially correlated in p_T.

Parameters	0-20%	20-40%	40-60%	60-100%
A_e (GeV$^{-2}c^2$)	26.54 ± 70.83	19.73 ± 101.62	13.36 ± 27.89	10.60 ± 90.91
T_e (GeV$/c$)	0.197 ± 0.330	0.173 ± 0.437	0.189 ± 0.255	0.133 ± 0.409
A (GeV$^{-2}c^2$)	2.27 ± 10.95	2.25 ± 10.81	0.99 ± 4.58	1.02 ± 3.80
T (GeV$/c$)	0.759 ± 0.783	0.668 ± 0.693	0.717 ± 0.727	0.558 ± 0.460
n	3.27 ± 0.86	3.12 ± 0.70	3.13 ± 0.78	2.98 ± 0.49
χ^2/NDF	0.0034	0.0030	0.0066	0.0089

Table 4.2: Fitting parameters of the two-component model fits to the π^0 invariant differential yields.

Parameters	0-20%	20-40%	40-60%	60-100%
A	1.88 ± 0.85	1.20 ± 0.53	0.73 ± 0.46	0.36 ± 0.21
T (GeV$/c$)	0.304 ± 0.128	0.299 ± 0.137	0.265 ± 0.156	0.217 ± 2.516
n	8.11 ± 4.05	7.89 ± 4.73	6.61 ± 3.12	5.98 ± 0.12
χ^2/NDF	0.101	0.047	0.174	0.207

Table 4.3: Fitting parameters of the Tsallis fits to the η invariant differential yields.

The ratios of the measured η and π^0 yields are shown in Figure 4.6 for the different multiplicity bins. As for the minimum bias analysis, common systematics like the material budget uncertainty are canceled out. In comparison to the minimum bias ratio which is also shown, the multiplicity dependent results do not show a significant deviation. Also an ordering by event multiplicity is not observed. For a better visibility, η/π^0 ratios for the different multiplicities in comparison with the minimum bias result are presented in separate plots in A.4.
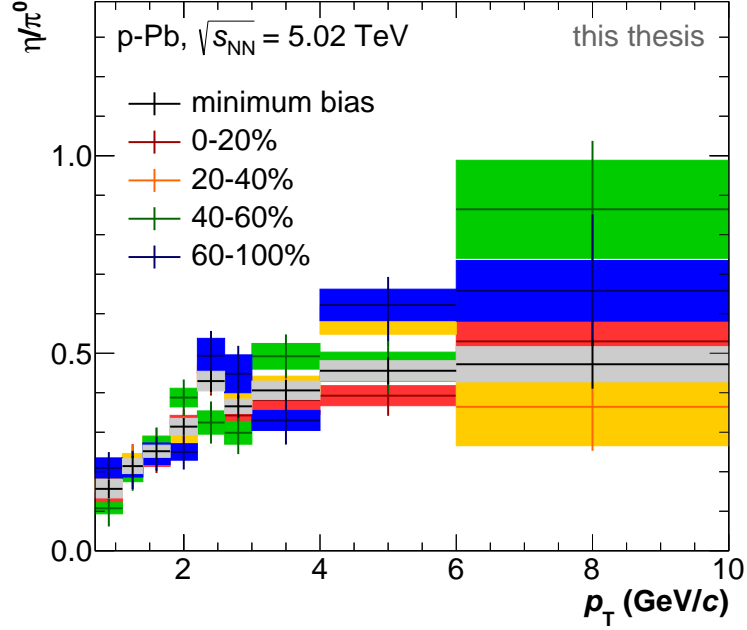
Figure 4.6: Ratio of the η and π^0 invariant differential yields for the different V0A multiplicities and minimum bias. Statistical uncertainties are shown as error bars, systematic uncertainties as boxes.

In order to better compare the multiplicity dependent meson yields with the minimum bias results, the nuclear modification factor $R_{\text{mult/MB}}$ is constructed:

$$R_{\text{mult/MB}}(p_{\text{T}}) = \frac{\langle N_{\text{coll}}^{\text{V0A, MB}} \rangle \cdot \mathrm{d}^2 N_{\pi^0,\eta}^{\text{mult}}/\mathrm{d}y\mathrm{d}p_{\text{T}}}{\langle N_{\text{coll}}^{\text{V0A, mult}} \rangle \mathrm{d}^2 N_{\pi^0,\eta}^{\text{MB}}/\mathrm{d}y\mathrm{d}p_{\text{T}}} \tag{4.3}$$

This is the ratio of the invariant differential meson yields measured in a certain multiplicity class and in minimum bias p–Pb collisions, both normalized to the average number of binary p-nucleus collisions, $\langle N_{\text{coll}}^{\text{V0A}} \rangle$, of the respective V0A multiplicity class. The values of $\langle N_{\text{coll}}^{\text{V0A}} \rangle$ for the different multiplicity classes are calculated with a Glauber model [97] and are taken from [89].

The Nuclear modification factors $R_{\text{mult/MB}}$ for the different multiplicity classes are shown for both neutral mesons in Figure 4.7. As common systematics cancel out in the ratio, the presented systematic uncertainties are dominated by the uncertainties of the $\langle N_{\text{coll}}^{\text{V0A}} \rangle$ values. These are 8% for minimum bias, of the order of 10% for high multiplicities and of the order of 20% for the lowest multiplicities.
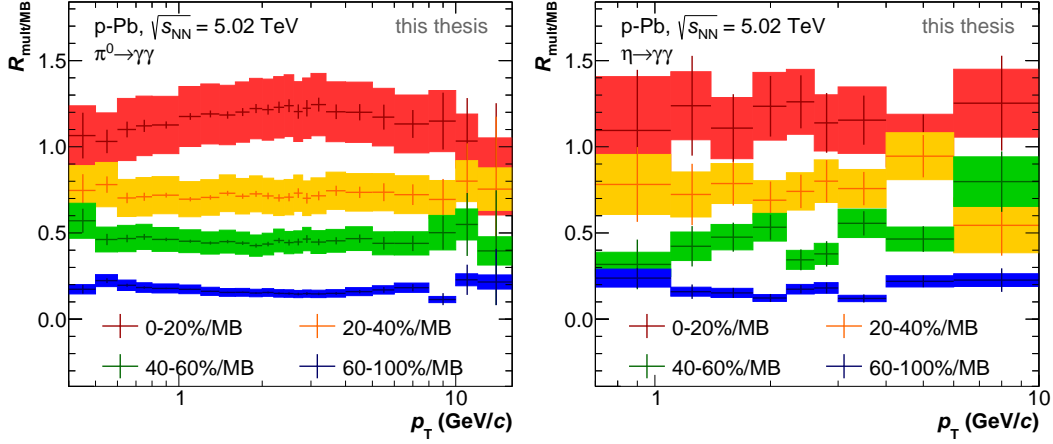
Figure 4.7: Nuclear modification factors $R_{\mathrm{mult/MB}}$ for the different V0A multiplicity classes for neutral pions (left) and η mesons (right). Statistical uncertainties are presented as vertical error bars. The systematic uncertainties, which include the uncertainties of the $R_{\mathrm{mult/MB}}$ normalization, are given as boxes.

The constructed ratios agree for both mesons for same multiplicities. All $R_{\mathrm{mult/MB}}$ show a nearly constant behavior versus p_{T}. In case of the π^0, a small increase of the central values at intermediate p_{T} is observed for the 0-20% multiplicity class, while the 60-100% multiplicity class shows a small decrease in the same p_{T} region. But as already stated before, a pronounced hardening of the spectra with increasing multiplicity in not observed.

For the 0-20% multiplicity class, the π^0 nuclear modification factor lies around 1.18, but still compatible with unity. With decreasing event multiplicity, also the ratio decreases. The mean values obtained from a constant fit are 0.71 for 20-40%, 0.45 for 40-60% and 0.16 for 60-100%. In case of the η analysis, constant fits give similar values.

In contrast to the nuclear modification factor R_{pPb} for minimum bias p–Pb collisions, deviations from unity in the $R_{\mathrm{mult/MB}}$ cannot be directly interpreted as nuclear effects. As already mentioned in Sec. 3.6, the correlation between the measured multiplicity, $N_{\mathrm{part}}/N_{\mathrm{coll}}$ and the impact parameter b is much weaker than for AA collisions and the values of $\langle N_{\mathrm{coll}}^{\mathrm{V0A}} \rangle$ and thus the constructed $R_{\mathrm{mult/MB}}$ may be biased. This is discussed in detail in the ALICE paper "Centrality dependence of particle production in p–Pb collisions at $\sqrt{s_{\mathrm{NN}}} = 5.02$ TeV " [89]. In this paper, also the centrality dependent nuclear modification factor Q_{pPb} for charged hadrons shows a deviation from unity, when using V0A as estimator. In order to minimize the multiplicity bias the

choice of a different centrality estimator in combination with $\langle N_{\mathrm{coll}} \rangle$ values determined with assumptions on the particle production is proposed. For this approach the charged hadron Q_{pPb} is found to be consistent with unity at high transverse momenta for all centrality classes. A corresponding continuation of the neutral meson analysis would be of interest, as well as the comparison to model calculations.

4.2   Combined ALICE Results

For the published ALICE neutral meson results [90], analyses using different approaches and detectors are combined. In addition to the photon conversion method presented in this thesis, neutral mesons in p–Pb collisions are also reconstructed via the following methods:

PCM-$\gamma^*\gamma$

With the PCM-$\gamma^*\gamma$ method, the neutral pion is reconstructed via the Dalitz decay channel $\pi^0 \to \gamma^*\gamma \to e^+e^-\gamma$ with a branching ratio of $1.174 \pm 0.035\%$ [13]. The primary e^+e^- pair that originates from the virtual photon is reconstructed within ITS and TPC. The real photon is reconstructed with the photon conversion method. For this purpose, the same selection criteria are applied as descried in this work. More details concerning this method and the p–Pb analysis can be found in [98]. Also the η meson decays via the Dalitz decay, but due to the branching ratio of only $(6.9 \pm 0.4) \cdot 10^{-3}$ the statistics are not sufficient for a proper reconstruction via this method.

PHOS

With the PHOS method, neutral pions are measured via the two-photon decay channel $\pi^0 \to \gamma\gamma$ with both photons reconstructed in the PHOS calorimeter. A detailed description of the π^0 p–Pb analysis with PHOS can be found in [99] and [100]. Although it is in principle possible to also reconstruct the η meson via its two-photon decay with the PHOS method, this approach was not followed for the analysis of the p–Pb data sample. Due to the small acceptance of the PHOS calorimeter in combination with the larger opening angle of the photons and the smaller branching ratio as compared to the π^0 two-photon decay, the statistics are very limited for a corresponding η PHOS analysis.

EMC

Analog to the PHOS analysis, neutral mesons can also be measured via the reconstruction of two photons in the electro-magnetic calorimeter EMCal. The EMC analysis is performed for π^0 and η mesons in p–Pb collisions. Details of the meson reconstruction using EMC can be found in the corresponding ALICE internal analysis note [101].

PCM-EMC

In addition to the PCM and the EMC method, also the hybrid PCM-EMC approach is performed for the neutral meson analysis in p–Pb collisions. Here, one photon of the two-photon decay is reconstructed with PCM and the other with the EMC method. The selection criteria are the same as for the stand-alone PCM and EMC method. Details of the π^0 and η analysis using PCM-EMC can be found in [102].
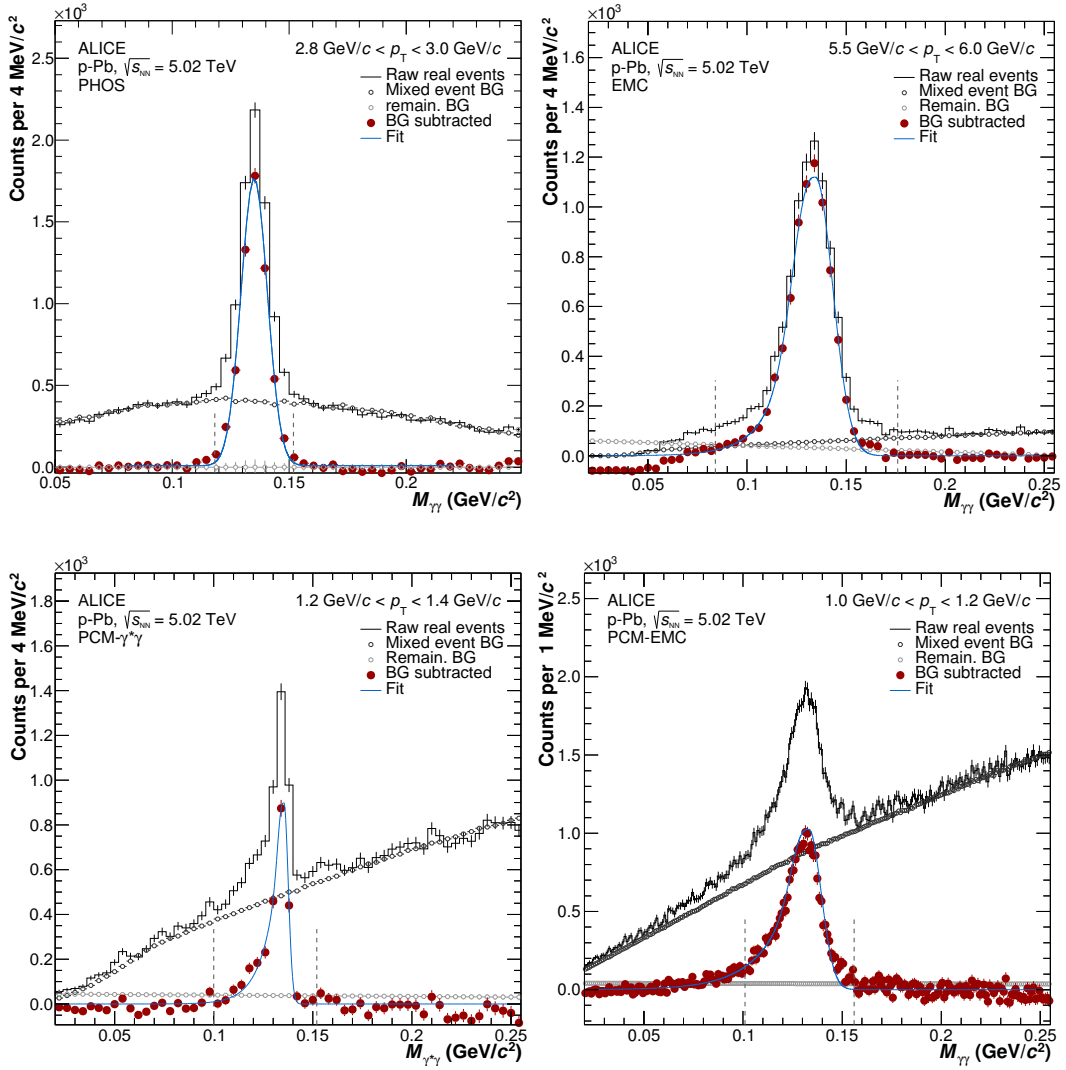

Figure 4.8: Exemplary diphoton invariant mass distributions around the π^0 mass before and after background subtraction for the PHOS, EMC, PCM-$\gamma^*\gamma$, and PCM-EMC reconstruction methods. The limits of the signal integration region are indicated by the two vertical dashed lines. [90]

4.2.1 Invariant Differential Meson Yields

For all approaches the neutral mesons are reconstructed on a statistical basis via the invariant mass of the two real photons or of the virtual and the real photon in the PCM-$\gamma^*\gamma$ case. Corresponding exemplary invariant mass distribution for the π^0 and η reconstruction are shown in Fig. 4.8 and Fig. 4.9, respectively. Equivalent PCM invariant mass distributions have already been shown in Fig. 3.11.
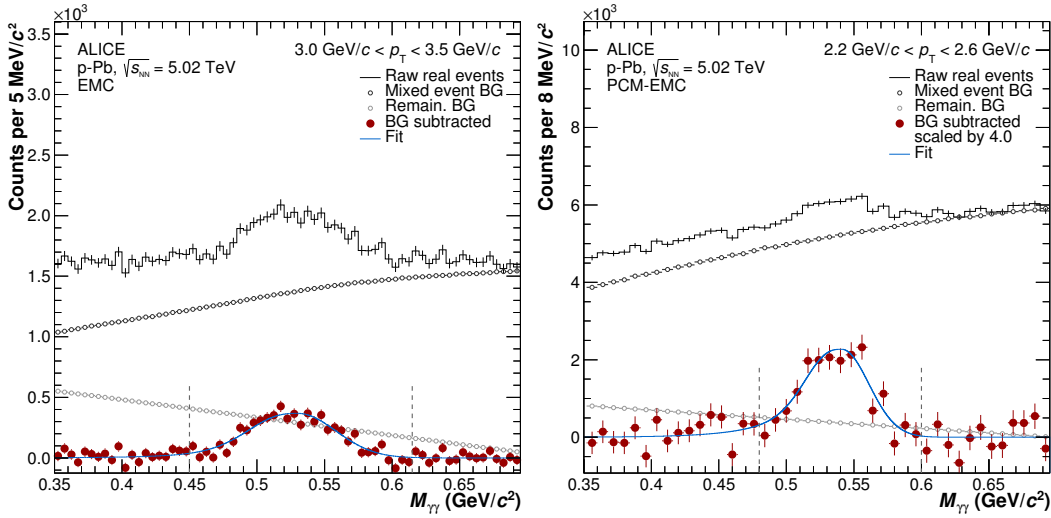

Figure 4.9: Exemplary diphoton invariant mass distributions around the η mass before and after background subtraction for the EMC and PCM-EMC reconstruction methods. The limits of the signal integration region are indicated by the two vertical dashed lines. [90]

The reconstructed peak widths and positions for data and Monte Carlo simulation are shown in Fig. 4.10 for both mesons and all used analysis methods. Data and Monte Carlo simulation show a good agreement for all methods in peak width and position. For the EMC and PCM-EMC measurements the reconstructed peak position is not calibrated to match the actual meson mass, but the Monte Carlo peak position is tuned to match the position reconstructed in data. Differences are considered in the systematic uncertainties of the measurements. For details see [90] and the given references of the individual reconstruction methods.

For the ALICE neutral meson result, the five individual invariant differential π^0 yields and the three individual invariant differential η yields are combined. In this way the advantages of the individual methods are combined. In addition to higher statistics, the ALICE neutral meson measure-
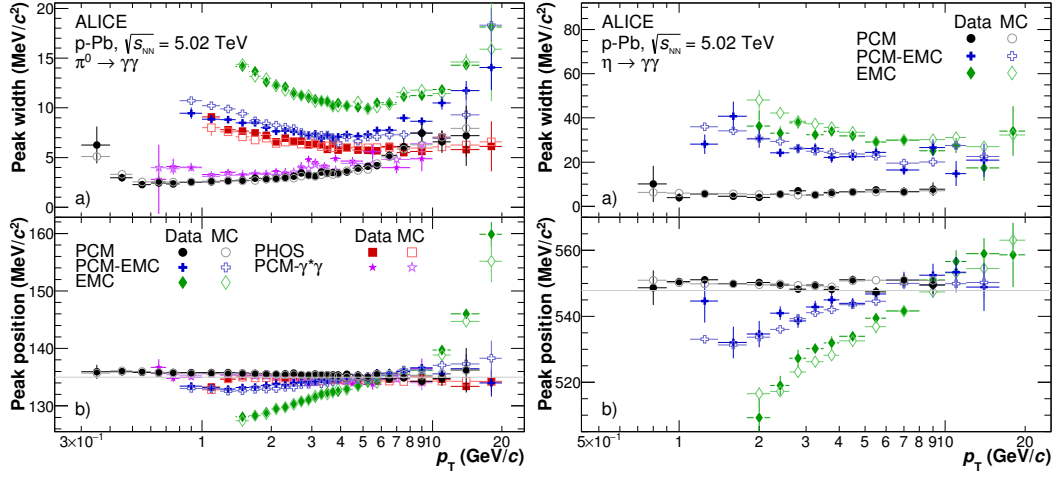
Figure 4.10: Reconstructed π^0 (left) and η (right) peak widths (top) and position (bottom) versus p_T for data and Monte Carlo simulation for all used analysis methods. [90]

ments also benefit from the precise reconstruction capabilities of the photon conversion method at very low p_T as well as from the higher p_T reach of the calorimeters. This is illustrated in Fig. 4.11, where the product of detector acceptance and reconstruction efficiency is plotted for the individual neutral meson measurements [98]-[102]. At high p_T this product reaches the largest values for measurements which include calorimeters. But for decreasing transverse momenta the acceptance times efficiency steeply decreases and measurements which include photon conversions are favored.
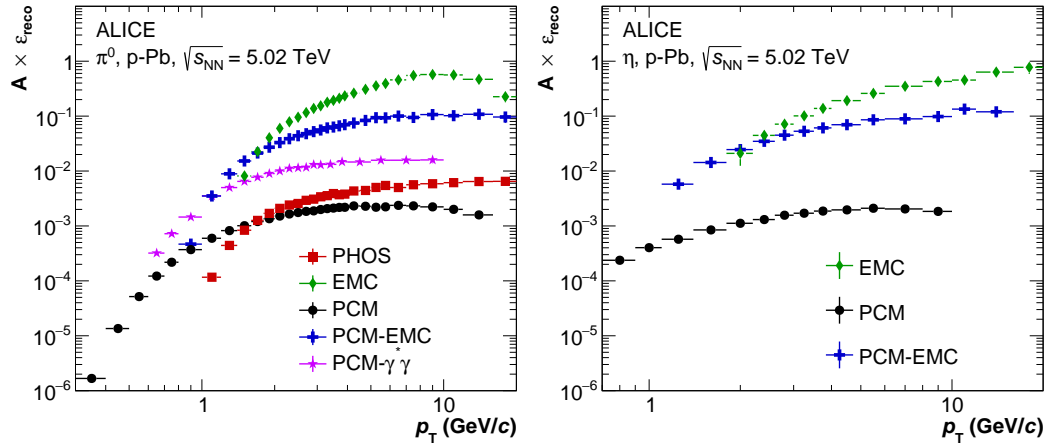

Figure 4.11: Product of detector acceptance and reconstruction efficiency versus p_T for the individual π^0 (left) and η (right) measurements.

The individual meson yields are combined using the Best Linear Unbiased Estimate (BLUE) method [103, 104]. Hereby, the correlations between the measurements are taken into account. While the results of PCM, PHOS and EMC are regarded as uncorrelated among each other, PCM, PCM-$\gamma^*\gamma$ and PCM-EMC are correlated due to the common reconstruction of one photon. For the same reason, also the EMC and PCM-EMC measurements are correlated. The correlation factors, needed as input for the combination, are estimated from the common systematic uncertainties of the methods. The different p_T reaches and statistics of the individual methods lead to differences in the individual p_T binnings. For the combined result, the finest possible binning is chosen and only measurements that provide data for a respective p_T bin are considered.

The combined ALICE neutral meson invariant differential yields are shown in Fig. 4.12. Statistical uncertainties are given as vertical error bars, systematic uncertainties are given as boxes.

It has to be noted that the yields and all ALICE results that are shown in the following are normalized to non-single diffractive events (NSD). The chosen minimum bias trigger (see Sec. 3.1.3) already suppresses contamination from single diffractive and electromagnetic interactions. In order to normalize to NSD events, the number of minimum bias events is divided by the factor 96.4% $\pm$ 3.1%. This corrected number is then used for the final normalization. Details about the determination of the NSD correction factor can be found in [105]. The uncertainty of the NSD corrections is quadratically added to the systematic uncertainty of the meson yields.

Tsallis Parameters	π^0	η
A	9.40 $\pm$ 0.49	0.87 $\pm$ 0.10
T (GeV/c)	0.159 $\pm$ 0.004	0.269 $\pm$ 0.019
n	7.169 $\pm$ 0.079	7.56 $\pm$ 0.34
χ^2/NDF	0.69	0.18

Table 4.4: Fit parameters and reduced χ^2 of the Tsallis fits to the combined π^0 and η meson invariant differential yields. [90]
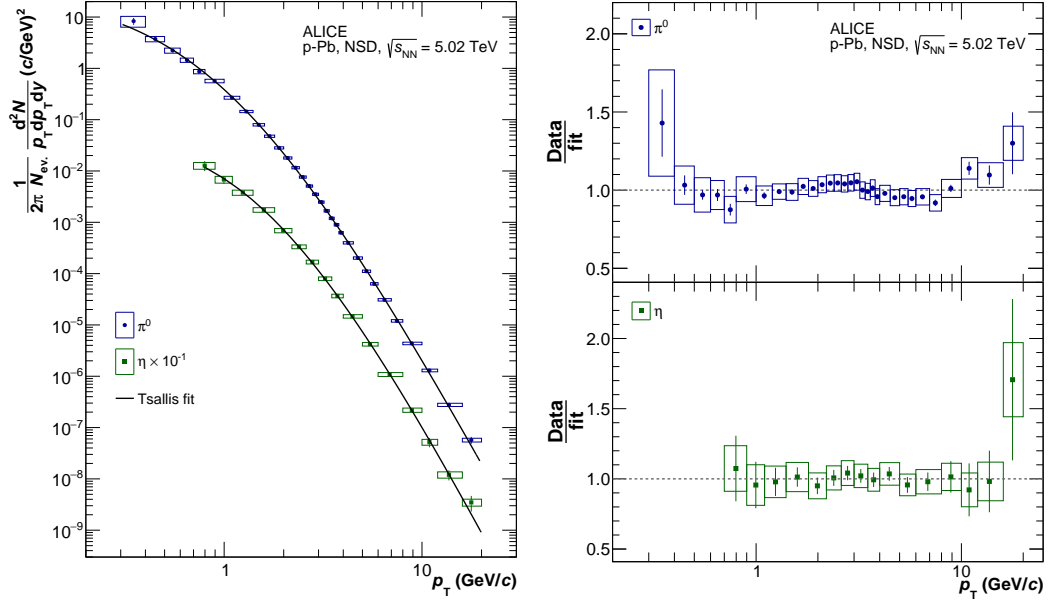
Figure 4.12: Left: Invariant differential π^0 and η yields produced in NSD p–Pb collisions at $\sqrt{s_{NN}}$ = 5.02 TeV. The statistical uncertainties are represented as vertical error bars whereas the systematic uncertainties are shown as boxes. In addition, Tsallis fits to the measured yields are shown. Right: Ratios of the measured data to their corresponding Tsallis fits. [90]

The π^0 and η yields are corrected for finite bin width (see Sec. 3.4.4) using Tsallis fits to the combined yields with quadratically added statistical and systematic uncertainties. These fits are also plotted. In the right panel of Fig. 4.12 the ratios of the π^0 and η yields to the respective Tsallis fit are shown. The Tsallis fits are able to successfully describe the meson yields. Only for the lowest and highest p_T bin, the data deviates from the fit, but as the uncertainties are large, the deviations are smaller than 2σ. However, it has to be noted that the Tsallis fit does not correspond to a perfect power law, which is expected from QCD as spectral shape at high p_T. The corresponding fitting parameters can be found in Tab. 4.4. The small values of the reduced χ^2 are due to correlations of the systematic uncertainties that are not considered.

Figure 4.13 shows the ratios between the individual invariant differential yields and the Tsallis fit to the combined measurement for the π^0 and the η meson. Again, statistical uncertainties are represented as vertical error bars whereas the systematic uncertainties are given as boxes. The ratios illustrate the good agreement of the individual neutral meson measurements with the combined results as well as among each other.
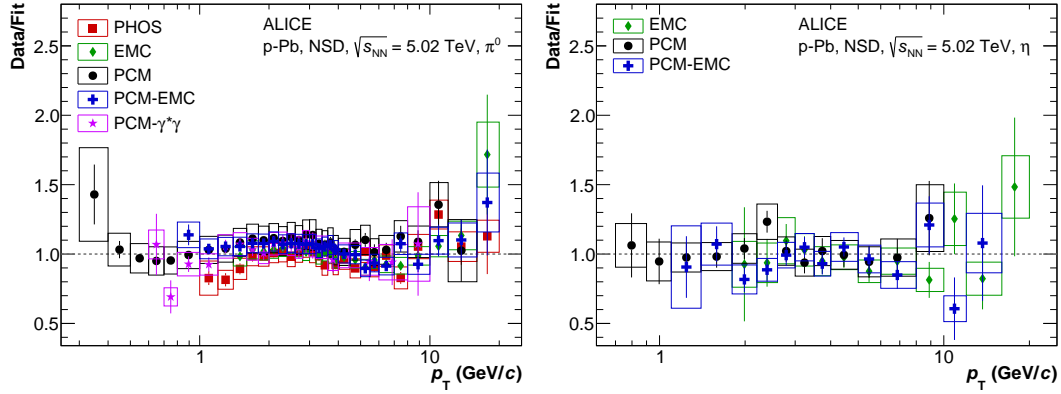
Figure 4.13: Ratios between the individual invariant differential yields and the Tsallis fit to the combined measurement for the π^0 (left) and the η meson (right). The statistical uncertainties are represented as vertical error bars whereas the systematic uncertainties are shown as boxes. [90]

4.2.2 η/π^0 Ratio

The η/π^0 ratio is calculated individually for the three methods that provide a π^0 and an η measurement: EMC, PCM, and PCM-EMC. The individual ratios are then combined with the BLUE method, as it is done for the meson invariant differential yields. In this way, common systematic uncertainties like the material budget uncertainty for PCM or the global energy scale uncertainty for the EMC method can be canceled out in the ratio. The ratios are corrected for finite bin width by a vertical shift of the meson spectra.

The combined ALICE η/π^0 ratio is presented in Fig. 4.14. The ratio increases with p_T and reaches a plateau of $0.483 \pm 0.015(\text{stat}) \pm 0.015(\text{sys})$ for transverse momenta above $4\,\text{GeV}/c$. The ALICE p–Pb η/π^0 ratio is compared to the ALICE pp result at $\sqrt{s} = 7$ TeV, as well as to the ratio measured in d–Au collisions at $\sqrt{s_{NN}} = 200$ GeV with PHENIX [106] and in fixed-target p–Be and p–Au collisions at $\sqrt{s_{NN}} = 29.1$ GeV with TAPS/CERES [107]. All measured ratios are in good agreement in shape and magnitude, despite the different collision systems and energies. This universality of the η/π^0 ratio was already reported in [106] and might indicate that the fragmentation into light mesons is independent of the collision system.

In addition to the measured data, the η/π^0 ratio is also estimated via the so-called m_T scaling. This method is often used to estimate the yield of the η meson or other particles in the absence of a real measurement. For this purpose, the η yield is calculated from the Tsallis parametrization to
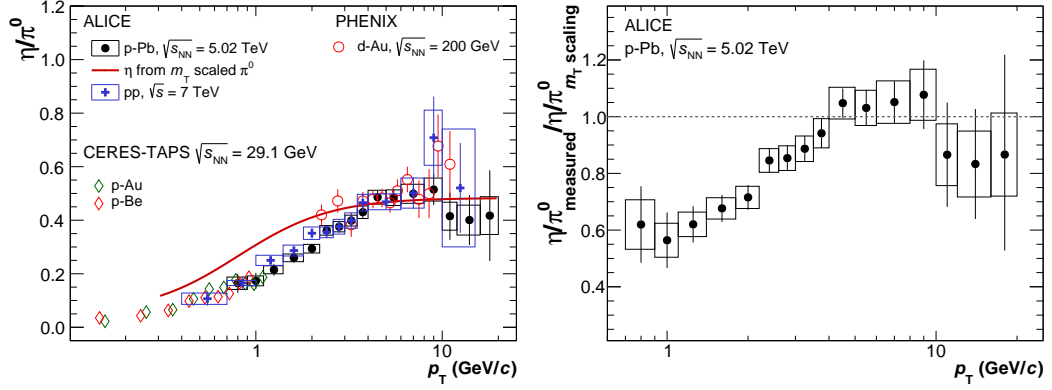
Figure 4.14: Left: η/π^0 ratio as function of p_T measured in NSD p–Pb collisions at $\sqrt{s_\mathrm{NN}}$ = 5.02 TeV. The statistical uncertainties are shown as vertical error bars. The systematic uncertainties are represented as boxes. For comparison, also the η/π^0 ratios measured in 7 TeV pp collisions with ALICE [94], in d-Au collisions at $\sqrt{s_\mathrm{NN}}$ = 200 GeV with PHENIX [106], and in p–Au and p–Be collisions at $\sqrt{s_\mathrm{NN}}$ = 29.1 GeV with TAPS/CERES [107] are shown, as well as the ratio where the η yield is obtained via m_T scaling from the measured p–Pb π^0 yield. Right: Ratio of the measured η/π^0 ratio to the one obtained via m_T scaling. [90]

the combined π^0 yield, P_{π^0}, assuming a scaling behavior with the transverse mass $m_\mathrm{T} = \sqrt{p_\mathrm{T}^2 + m^2}$:

$$E\,\mathrm{d}^3N^\eta/\mathrm{d}p^3 = C_\mathrm{m} \cdot P_{\pi^0}\left(m_{\mathrm{T},\eta}\right)\ , \tag{4.4}$$

with $C_\mathrm{m} = 0.483 \pm 0.015_\mathrm{stat} \pm 0.015_\mathrm{sys}$

The ratio of the m_T-scaled η yield to the π^0 Tsallis fit is shown in Fig. 4.14 as a red curve. In the plateau region above $4\,\mathrm{GeV}/c$, the m_T scaling prediction agrees with the measurement, but with decreasing transverse momentum the data more and more deviates from the prediction. The ratio of the measured η/π^0 ratio to the m_T scaling curve is shown in the right panel of Fig. 4.14. Here, the deviation of about 40% for the lowest p_T bins becomes visible. Also for pp collisions at $\sqrt{s}$ = 7 TeV, it has recently been shown, that particle yields are overestimated by m_T scaling at low transverse momenta, especially if pions are used as reference particles [108]. For analyses that rely on an accurate description of particle yields, like it is the case for a direct photon or dilepton measurement, a measurement of the η meson especially at low p_T therefore becomes crucial as input. Since the deviation from m_T scaling

appears rather uniform for different $\sqrt{s}$, the ratio presented in the right panel of Fig. 4.14 could be used as an empirical correction to the m_T scaled η spectra in the absence of a measurement.

4.2.3 Nuclear Modification Factor

The combined ALICE nuclear modification factor R_pPb (see Eq. 4.1) is not directly calculated from the combined meson yields, but individually for each method. As described for the PCM pp reference, see Sec. 4.1.1, the references for the other reconstruction methods are also constructed via interpolation. Therefore, solely their respective contributions to the published meson spectra measured at $\sqrt{s} = 2.76$ TeV [1, 93], $\sqrt{s} = 7$ TeV [94] and $\sqrt{s} = 8$ TeV [95] are used as input. The individual R_pPb are then combined with the BLUE method.
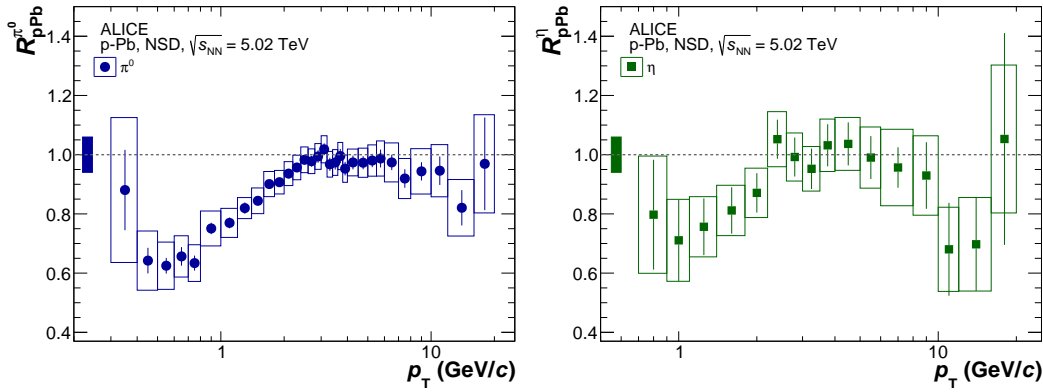

Figure 4.15: π^0 (left) and η (right) nuclear modification factors R_pPb measured in NSD p–Pb collisions at $\sqrt{s_\text{NN}} = 5.02$ TeV. The statistical uncertainties are shown as vertical error bars and the systematic uncertainties are represented as boxes. The overall normalization uncertainty is given as the solid box around unity. [90]

As for the η/π^0 ratio, this approach has the advantage that common uncertainties of the p–Pb and pp measurement can be canceled. Due to the lack of a published PCM-$\gamma^*\gamma$ pp measurement, the PCM pp reference is used for the calculation of the PCM-$\gamma^*\gamma$ nuclear modification factor. In this way, the uncertainty of the material budget for the reconstruction of one converted photon can be canceled out, but an additional correlation between the PCM and the PCM-$\gamma^*\gamma$ R_pPb is introduced that is considered in the combination. In order to correct for finite bin width, the bin-shift of the data points is

applied in the *y*-direction. In this way, the common binning of the p–Pb measurements and the constructed pp references is preserved. Due to the similar shape of the spectra in pp and p–Pb, the effect is small.

The combined ALICE nuclear modification factors for neutral pions and η mesons measured in NSD p–Pb collisions at $\sqrt{s_{NN}}$ = 5.02 TeV are presented in Fig. 4.15. Statistical uncertainties are show as vertical error bars, whereas the systematic uncertainties are presented as boxes. The overall normalization uncertainty includes the uncertainties of the NSD normalization, of the nuclear overlap function $\langle T_{pPb} \rangle$ and of the pp cross section. It amounts to about 6% and is illustrated in the plots as solid box around unity.

The nuclear modification factors for both neutral mesons are compatible with unity for transverse momenta above 2 GeV/*c*. The comparison to the charged pion R_{pPb} [28] in Fig. 4.16 shows a good agreement between the measurements for neutral and charged pions within uncertainties over the whole p_T range.
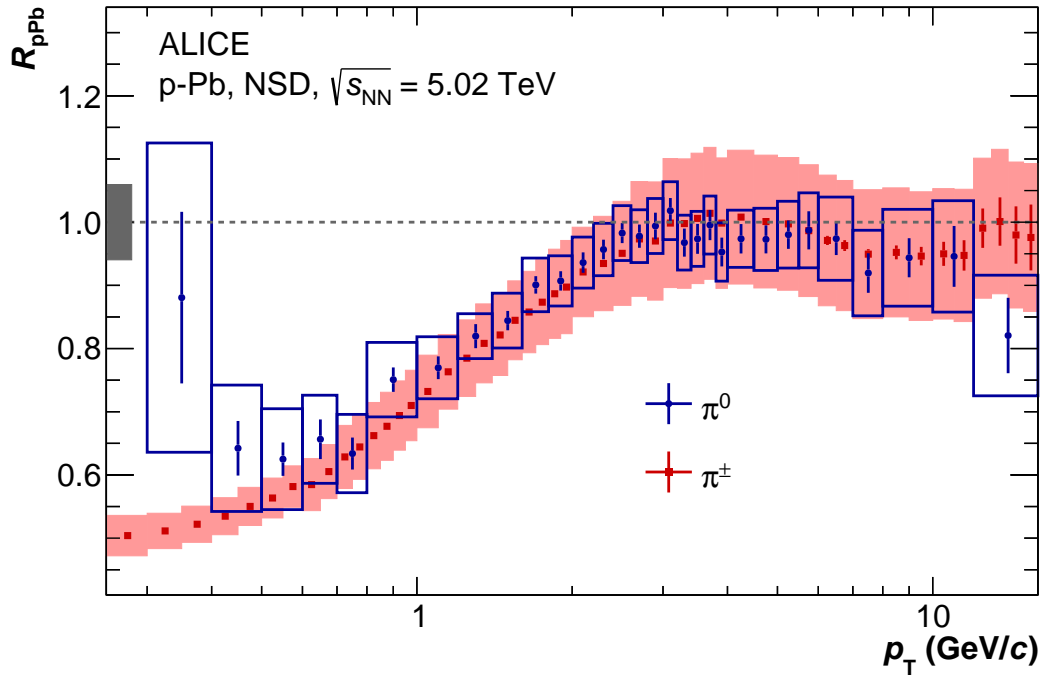

Figure 4.16: Comparison of the nuclear modification factors for neutral [90] and charged pions [28]. Statistical uncertainties are given as vertical error bars, systematic uncertainties as boxes. The overall normalization uncertainty of about 6% that is common for both measurements is represented as the solid box around unity.

4.3   Comparison to Theoretical Models

The combined ALICE neutral meson results presented in Sec. 4.2 are in the following compared to different theoretical model predictions.

The comparison of several calculations to the invariant differential π^0 and η yields is shown in Fig. 4.17. In the right panel, the ratios of the predictions and the Tsallis fits to the measured spectra are presented. For a better comparison, also the ratios of the measured data points to their respective fits are shown.
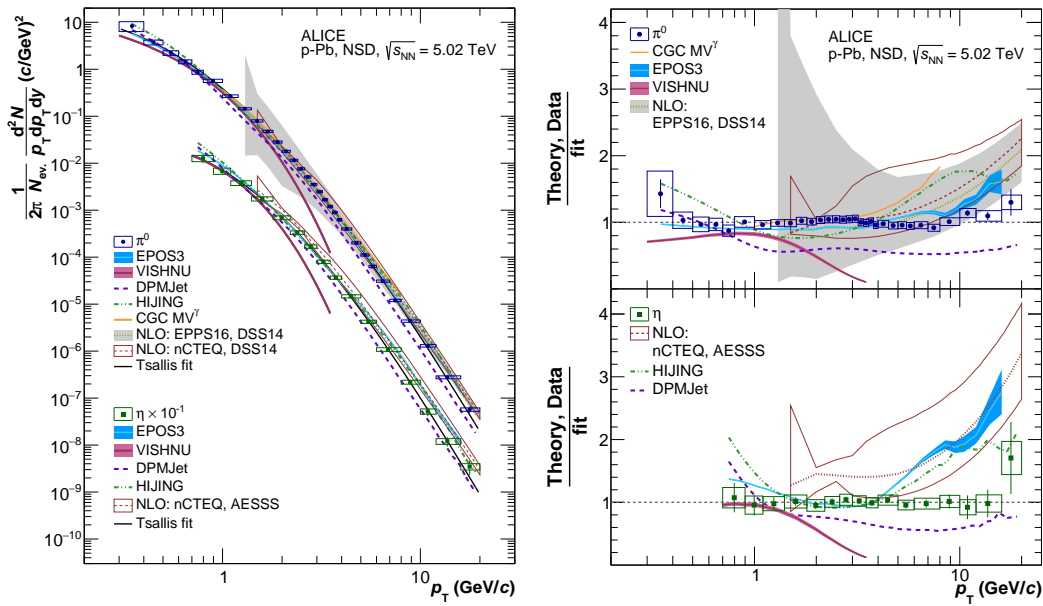

Figure 4.17: Comparison of several theoretical calculations to the invariant differential π^0 and η yields produced in NSD p–Pb collisions at $\sqrt{s_{\mathrm{NN}}} = 5.02$ TeV from Fig. 4.12. In the right panel, the ratios of the measured meson yields and the theory predictions to the corresponding Tsallis fits are shown. See text or [90] for details and references.

Two different NLO pQCD calculations are compared to the measured π^0 yield. The calculation represented by the ocher dashed line and the gray uncertainty band uses the EPPS16 nPDF [25] with the CT14 PDF [109]. The NLO pQCD calculation shown by the red dashed line and the red uncertainty box uses the nCTEQ nPDF [26]. Both measurements use DSS14 [110] as fragmentation function (FF). Both calculations are able to reproduce the measured π^0 invariant differential yield within the large uncertainties that

are due to the nPDF, the FF and variation of the factorization, renormalization and fragmentation scales. This choice of scales dominates the systematic uncertainties of the model calculations. The η meson invariant differential yield is compared to a respective pQCD NLO calculation using nCTEQ nPDF [26] and AESSS FF [111]. The central values of this calculation overestimate the measured η yield, but within the uncertainties it still agrees at intermediate p_T between 1.5 and 5 GeV/c. For larger transverse momenta the difference between data and calculation increases up to a factor two at 10 GeV/c. It has to be noted that so far the results of inclusive η meson measurements at the LHC [93–95] are not included into global fits to constrain the η meson fragmentation function. An inclusion of these measurement could help to further improve the pQCD NLO prediction for the η meson.

The measured meson yields are also compared to predictions of the two event generators HIJING [69] and DPMJet [70] . The central values of the HIJING calculation are shown as green dashed line. The model underestimates the measured π^0 yield at intermediate p_T between 1 and 4 GeV/c by about 20%, while it agrees with the η measurement in the same transverse momentum range. For lower and higher p_T it overestimates both meson yields by up to 60-80%. The DPMJet calculation, shown as dashed purple line, is able to reproduce the neutral meson yields for p_T smaller than 1 GeV/c, but underestimates them by about 40% for higher transverse momenta. DPMJET was tuned to reproduce RHIC measurements of hadron production at low and moderate p_T, thus an adaption of the model parameters to successfully describe particle yields in the LHC energy regime may be needed. Also the comparison of DPMJET model predictions to particle production measurements in pp collisions at LHC energies shows that the energy dependence of hadron production predicted by the model does not agree with data [112].

The inclusive π^0 spectrum is also calculated with a Color Glass Condensate (CGC) calculation [113] using MV$^\gamma$ [114] as initial condition. The CGC calculation, shown as orange line, agrees with the measured π^0 yield at intermediate p_T between 1 and 4 GeV/c. For larger transverse momenta the CGC calculation overestimates the neutral pion yield by up to 80% at 8 GeV/c.

The iEBE-VISHNU package [115] consists of a 3+1 viscous hydrodynamical model coupled to a hadronic cascade model [116]. A Monte-Carlo Glauber model is used to generate fluctuating initial conditions in the transverse plane. In Fig. 4.17 calculations for the π^0 and η invariant differential yields

with this model are represented as pink band. The measured meson yields are in agreement with this model for transverse momenta between 0.7 and 1.5 GeV/c, while for lower p_T the model underestimates the π^0 yield by about 20-40%. For higher p_T the discrepancy is even larger for both mesons. At 3.5 GeV/c the neutral meson yields are underestimated by the iEBE-VISHNU calculation by a factor five. The large deviation at high transverse momenta might indicate that additional mechanisms are needed to sufficiently describe particle production in p–Pb collisions. In particular jet production is missing in this hydrodynamical model.

Calculations of the EPOS3 [117] event generator are shown in Fig. 4.17 as light blue line with a blue error band representing statistical uncertainties. This model is based on 3D+1 viscous hydrodynamics, with flux tube initial conditions that are generated in the Gribov-Regge multiple scattering framework. The reaction volume is divided into a core and a corona part. The core is evolved using viscous hydrodynamics. The corona is composed of hadrons from string decays. The EPOS3 model is able to reproduce the measured invariant differential π^0 yield over the whole p_T range. Also inclusive spectra of other identified hadrons like charged pions, kaons, protons, Λ and Ξ baryons are properly described by this model, but only if collective radial flow is added to the model [82, 118]. In case of the η meson, the measured p_T spectrum is only reproduced by the EPOS3 calculation for transverse momenta below 4 GeV/c. For larger p_T the η yield is highly overestimated.

The theoretical models that provide calculation for the neutral pion as well as for the η meson can also be compared to the measured η/π^0 ratio. The two event generators HIJING and DPMJet give a similar result and lie both close to the m_T scaling prediction shown as red line (see Sec. 4.2.2). At high p_T they both agree with the measured ratio but overestimate it for lower transverse momenta, as it is also observed for the m_T scaling curve. The EPOS3 prediction lies below the m_T scaling curve and closer to the measured ratio for transverse momenta below 4 GeV/c. For higher p_T the EPOS3 calculation overestimates the η/π^0 ratio by nearly a factor two. This is due to the bad description of the η spectrum in this p_T range. The VISHNU calculation is in agreement with the measured data over the whole p_T range of the calculation, which means up to 3.5 GeV/c, although the individual neutral meson spectra are only reproduced up to 1.5 GeV/c.

In Figure 4.19 the π^0 (left) and η (right) nuclear modification factors R_{pPb} measured in NSD p–Pb collisions at $\sqrt{s_{NN}} = 5.02$ TeV are compared to different model calculations. NLO pQCD calculation of the π^0 R_{pPb} using
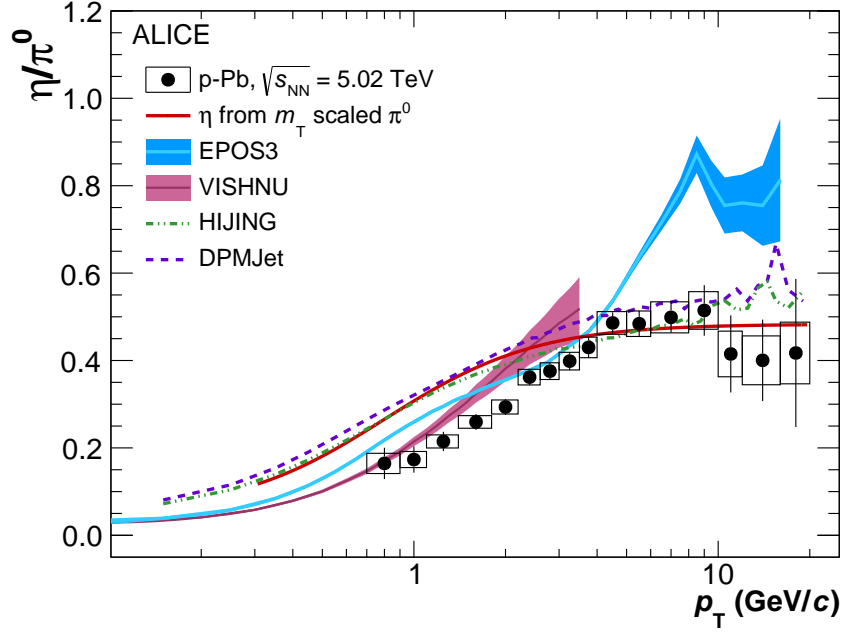
Figure 4.18: Comparison of different theoretical calculations to the η/π^0 ratio measured in NSD p–Pb collisions at $\sqrt{s_{\mathrm{NN}}} = 5.02$ TeV from Fig. 4.14. See text or [90] for details and references.

the EPPS16 nPDF[25] or the nCTEQ nPDF[26] are shown as ocher and red dashed line. The systematic uncertainties are given as gray error band and red error box, respectively. Both calculations use the DSS14 FF [110]. The η R_{pPb} is compared to an NLO calculation using nCTEQ nPDF [26] and AESSS FF [111]. The central values of the NLO calculations underestimate the measured nuclear modification factors for transverse momenta below $6\,\mathrm{GeV}/c$. While the discrepancy of the central values to the data is well covered within the large systematic uncertainties of the EPPS16 calculation, the nCTEQ predictions with their smaller systematic uncertainties show a sizable deviation. At high p_{T} the calculations are in agreement with the measured data. The CGC calculation [113] nicely reproduces the neutral pion R_{pPb} in the whole p_{T} range of the calculation.

The presented comparison of the measured data to model calculations shows that several theoretical approaches are able to reproduce the data at least in confined p_{T} ranges. While models that include hydrodynamic approaches show a better agreement with the data at low p_{T}, the inclusion of jet production seems to be mandatory for a good description at higher p_{T}. State-of-the-art pQCD calculations agree with the measured π^0 spec-
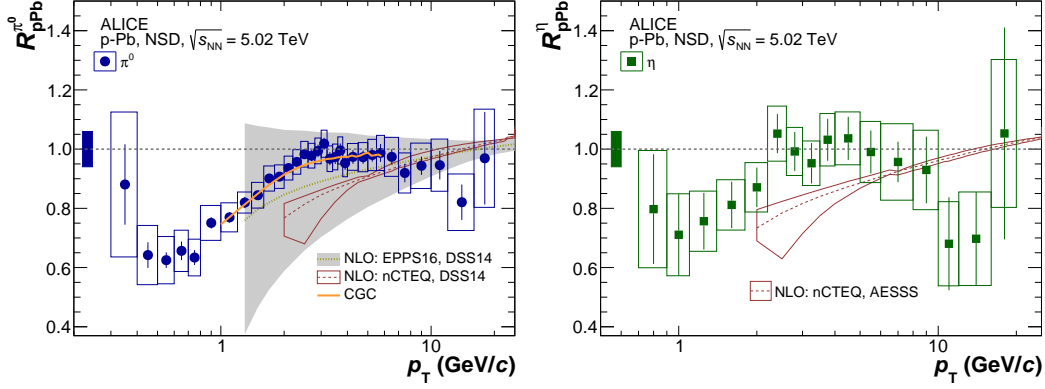
Figure 4.19: Comparison of different theoretical model calculations to the π^0 (left) and η (right) nuclear modification factors R_{pA} measured in NSD p–Pb collisions at $\sqrt{s_{NN}}$ = 5.02 TeV. See text or [90] for details and references.

trum within the large uncertainties, but the η invariant differential yield is overestimated. In general, the agreement between the models and the neutral π^0 measurement is better than for the η. It seems that the η meson is very challenging to model, maybe due to the mixed quark content, and the inclusion of the recent inclusive η measurements at the LHC could help to further constrain the theory calculations. As systematic uncertainties of the theory calculations are either very large or not given at all, a real differentiation between the different calculations is not possible.

Summary

The measurement of particle production in p-Pb collisions at LHC energies allows for the study of fundamental properties of quantum chromodynamics at low parton momentum fraction x and high gluon densities.

Moreover, it is important as reference for heavy-ion collisions. It can show whether the initial state of the colliding nuclei plays a role in the observed suppression of hadron production at high p_{T} in Pb-Pb collisions. The measurement of neutral pions has the advantage of large statistics of identified particles over a relatively large transverse momentum range. In addition, the π^0 and η spectra are crucial for the background determination of other analyses like the measurement of direct photons or electrons from heavy flavor decays.

This thesis presents the measurement of neutral mesons, π^0 and η, via photon conversions in p–Pb collisions at $\sqrt{s_{\mathrm{NN}}} = 5.02$ TeV with the ALICE detector. The mesons are studied via their two-photon decay channels $\pi^0 \to \gamma\gamma$ and $\eta \to \gamma\gamma$ with both photons converted into e^+e^- pairs which are reconstructed in ITS and TPC. A secondary vertex finder is used to construct photon candidates from charged track pairs. The neutral meson reconstruction is done on a statistical basis via the invariant mass of two photon candidates. Monte Carlo simulations using the DPMJet and HIJING event generators are used for spectra corrections.

The presented analysis is executed for minimum bias collisions and for four different multiplicity classes, using the total charge deposited in the V0A detector at backward rapidity (according to the rapidity definition in p–Pb collisions) as multiplicity estimator. A hardening of the neutral meson spectra with increasing multiplicity as found for charged hadrons, especially for the heavier protons and lambdas, is not observed. The hardening may be masked by the large uncertainties that mainly arise from the low statistics of the multiplicity dependent analysis. The η/π^0 ratio does not show a multiplicity dependence. $R_{\mathrm{mult/MB}}$, the ratio of the invariant differential meson yields measured in a certain multiplicity class and in minimum bias p–Pb collisions,

both normalized to the average number of binary p-nucleus collisions, shows a nearly constant behavior as a function of p_T for all multiplicity classes and both mesons. While $R_{mult/MB}$ exceeds unity for highest event multiplicities, the ratio decreases with decreasing multiplicity and is strongly suppressed for small multiplicities. Although the ratios show a clear deviation from unity, the observation of a nuclear modification cannot be stated as the chosen multiplicity estimator introduces a multiplicity bias. This has been shown in Ref. [89], where the charged hadron nuclear modification factor Q_{pPb} shows a similar behavior when using V0A as centrality estimator. In this paper, the use of a different estimator in combination with $\langle N_{coll} \rangle$ values determined with assumptions on the particle production is proposed to minimize the bias. Using this approach, the charged hadron Q_{pPb} is in agreement with unity at high p_T for all centrality classes. A corresponding adaption of the neutral meson analysis would be of interest, as well as the comparison to theoretical model predictions.

The combined ALICE results on neutral meson production, including the minimum bias results presented in this thesis for the PCM method, have been published in [90]. The invariant differential meson yields, the η/π^0 ratio and the π^0 and η nuclear modification factors, R_{pPb}, are presented and compared to several theoretical model predictions, including state-of-the-art NLO pQCD calculations, event generators, hydrodynamical models and a Color Glass Condensate calculation.

All models are able to reproduce the measured π^0 and η yields at least in restricted p_T regions. While models that include a hydrodynamic description show a better agreement at low p_T, the inclusion of hard production processes (jets) seems to be mandatory for a good description at high transverse momenta. NLO pQCD calculations agree with the measured π^0 yield within the large uncertainties of the calculations over the whole available p_T range. A respective calculation for the η meson only agrees with the measured yield for intermediate p_T. At larger transverse momenta the calculation overestimates the η yield by about a factor two. In general, the discrepancies between measurement and model predictions are larger for the η meson. The presented η measurement provides an additional constraint for calculations, in particular for the fragmentation function of the η.

The measured η/π^0 ratio is in good agreement with the ratios measured in pp collisions at $\sqrt{s} = 7$ TeV and in pA and AA collisions at lower energies. This observed universality indicates that the fragmentation into light mesons might be independent of the collision system. For transverse momenta below

$2\,\mathrm{GeV}/c$, a clear deviation from m_T scaling is observed. Since models that include hydrodynamics better describe this behavior than other models, radial flow might also play a role in small collision systems like pp and p–Pb.

The π^0 and η nuclear modification factors agree with each other and are consistent with unity for transverse momenta above $2\,\mathrm{GeV}/c$. A nuclear modification is not observed which supports the interpretation that the measured π^0 suppression in Pb–Pb collisions is due to parton energy loss in the hot QCD medium. The CGC prediction nicely reproduces the measured π^0 R_pPb, while the central values of the pQCD calculations underestimate it for intermediate p_T.

However, a clear differentiation between the theoretical models is not possible since their uncertainties are either large or not given at all. Regarding the NLO pQCD calculations, the large uncertainties are dominated by the scale uncertainty as well as by the uncertainties of nuclear PDFs and FFs. Hence, the presented neutral meson measurement provides an important input for theoretical models and can help to further constrain fragmentation and nuclear parton distribution functions.

Zusammenfassung

Die Messung von Teilchenproduktion in p–Pb-Kollisionen bei LHC-Energien ermöglicht die Untersuchung von fundamentalen Eigenschaften der Quantenchromodynamik bei niedrigem Partonimpulsanteil x und hohen Gluonendichten.

Darüber hinaus ist sie wichtig als Referenz für Schwerionenkollisionen. Sie kann zeigen, ob der Anfangszustand des kollidierenden Kerns eine Rolle bei der beobachteten Unterdrückung der Hadronenproduktion bei hohem p_T in Pb–Pb-Kollisionen spielt. Die Messung von neutralen Pionen liefert den Vorteil großer Statistik identifizierter Teilchen über einen relativ großen Transversalimpulsbereich. Zusätzlich sind die π^0- und η-Spektren wichtig für die Untergrundbestimmung anderer Analysen, wie der Messung direkter Photonen oder Elektronen aus Beauty- und Charm-Zerfällen.

Diese Arbeit präsentiert die Messung neutraler Mesonen, π^0 und η, mittels Photonkonversionen in p–Pb-Kollisionen bei $\sqrt{s_\mathrm{NN}}$ = 5.02 TeV mit dem ALICE-Detektor. Die Mesonen werden mittels ihres Zerfalls in zwei Photonen untersucht, $\pi^0 \rightarrow \gamma\gamma$ und $\eta \rightarrow \gamma\gamma$, wobei beide Photonen in e^+e^--Paare konvertieren, die im ITS und der TPC rekonstruiert werden. Ein Sekundärvertexsucher konstruiert Photonkandidaten aus Paaren geladener Tracks. Die Rekonstruktion der neutralen Mesonen geschieht auf statistischer Basis über die invariante Masse zweier Photonkandidaten. Monte-Carlo-Simulationen, die DPMJet und HIJING als Ereignisgeneratoren nutzen, werden genutzt um die Spektren zu korrigieren.

Die präsentierte Analyse wird für Minimum-Bias-Kollisionen und für vier verschiedene Multiplizitätsklassen durchgeführt. Die komplette deponierte Ladung im V0A-Detektor bei rückwärtiger Rapidität (entsprechend der Rapiditätsdefinition für p–Pb-Kollisionen) wird zur Multiplizitätsbestimmung genutzt. Ein Härterwerden der neutralen Mesonenspektren mit zunehmender Multiplizität wie es für geladene Hadronen gefunden wird, besonders für die schwereren Protonen und Lambdas, wird nicht beobachtet. Das Härterwerden könnte aber durch die großen Unsicherheiten verdeckt

sein, die hauptsächlich durch die niedrige Statistik der multiplizitätsabhängigen Analyse hervorgerufen werden. Das η/π^0-Verhältnis zeigt keine Abhängigkeit von der Multiplizität. $R_{\text{mult/MB}}$, das Verhältnis der invarianten differenziellen Mesonen-Yields in einer speziellen Multiplizitätsklasse und in Minimum-Bias-Kollisionen, beide auf die mittlere Anzahl binärer p-Kern-Kollisionen normiert, zeigt ein nahezu konstantes Verhalten als Funktion des Transversalimpulses für alle Multiplizitätsklassen und für beide Mesonen. Während $R_{\text{mult/MB}}$ größer als eins für die höchsten Multiplizitäten ist, nimmt das Verhältnis mit kleiner werdenden Multiplizitäten ab und zeigt eine starke Unterdrückung für niedrige Multiplizitäten. Obwohl das Verhältnis eine klare Abweichung von eins zeigt, kann die Beobachtung einer nuklearen Modifikation nicht bestätigt werden, da die verwendete Multiplizitätsbestimmung einen Bias einbringt. Dies wurde in Ref. [89] anhand des nuklearen Modifikationsfaktors Q_{pPb} für geladene Hadronen gezeigt, der ein ähnliches Verhalten zeigt, wenn V0A zur Ermittlung der Zentralität verwendet wird. In diesem Artikel wird die Wahl einer anderen Zentralitätsersbestimmung in Kombination mit $\langle N_{\text{coll}} \rangle$-Werten, in die Annahmen zur Teilchenproduktion einfließen, empfohlen, um den Bias zu minimieren. Mit dieser Herangehensweise stimmt Q_{pPb} für die geladenen Hadronen bei hohem p_{T} für alle Zentralitätsklassen mit eins überein. Eine entsprechende Fortführung der neutralen Mesonenanalyse wäre wünschenswert, sowie der Vergleich zu theoretischen Vorhersagen.

Die kombinierten ALICE-Resultate zur Produktion neutraler Mesonen, einschließlich der in dieser Arbeit präsentierten Minimum-Bias-Resultate mittels der PCM-Methode, wurden in [90] veröffentlicht. Die invarianten differenziellen Mesonen-Yields, das η/π^0-Verhältnis und die nuklearen Modifikationsfaktoren, R_{pPb}, für π^0 und η werden präsentiert und mit verschiedenen theoretischen Modellvorhersagen verglichen, darunter aktuelle NLO pQCD-Rechnungen, Ereignisgeneratoren, hydrodynamische Modelle und eine Color-Glass-Condensate-Rechnung.

Alle Modelle sind in der Lage, die gemessenen π^0- und η-Yields zumindest in begrenzten p_{T}-Bereichen zu reproduzieren. Während Modelle, die eine hydrodynamische Beschreibung beinhalten, eine bessere Übereinstimmung bei niedrigen p_{T} zeigen, scheint die Inklusion von harten Produktionsprozessen (Jets) für eine gute Beschreibung bei hohen Transversalimpulsen erforderlich zu sein. NLO pQCD-Rechnungen stimmen mit dem gemessenen π^0-Yield innerhalb der großen Unsicherheiten über den gesamten p_{T}-Bereich überein. Eine entsprechende Rechnung für das η-Meson

ist mit dem gemessenen Yield nur bei mittleren p_T verträglich. Bei höheren Transversalimpulsen überschätzt die Rechnung den η-Yield um ungefähr das Zweifache. Generell sind die Abweichungen zwischen Messung und Modellvorhersagen größer für das η-Meson. Die präsentierte η-Messung liefert zusätzliche Randbedingungen für Rechnungen, insbesondere für die Fragmentationsfunktion für das η-Meson.

Das gemessene $η/π^0$-Verhältnis ist in guter Übereinstimmung mit denen, die in pp-Kollisionen bei $\sqrt{s}$ = 7 TeV und in pA- und AA-Kollisionen bei niedrigeren Energien gemessen wurden. Diese festgestellte Universalität deutet an, dass die Fragmentation in leichte Mesonen unabhängig vom Kollisionssystem sein könnte. Für Transversalimpulse unterhalb von 2 GeV/c wird eine klare Abweichung von einer m_T-Skalierung beobachtet. Da Modelle, die Hydrodynamik beinhalten, dieses Verhalten besser beschreiben als andere Modelle, könnte es sein, dass radialer Fluss auch in kleinen Kollisionssystemen wie pp und p–Pb eine Rolle spielt.

Die nuklearen Modifikationsfaktoren für $π^0$ und η stimmen miteinander überein und sind verträglich mit eins für Transversalimpulse über 2 GeV/c. Eine nukleare Modifikation wird nicht beobachtet, was die Interpretation stützt, dass die gemessene $π^0$-Unterdrückung in Pb–Pb-Kollisionen durch Parton-Energieverlust im heißen QCD-Medium bedingt ist. Die CGC-Vorhersage reproduziert das gemessene $π^0$-R_pPb sehr genau, während die zentralen Werte der pQCD-Rechnungen den nuklearen Modifikationsfaktor für mittlere p_T unterschätzen.

Dennoch ist eine klare Differenzierung zwischen einzelnen Theoriemodellen nicht möglich, da deren Unsicherheiten entweder sehr groß sind oder gar nicht angegeben werden. Die NLO pQCD-Rechnungen betreffend werden die großen Unsicherheiten von der Skalenunsicherheit dominiert, sowie von den Unsicherheiten der nuklearen PDFs und FFs. Deshalb liefert die präsentierte Messung neutraler Mesonen einen wichtigen Input für theoretische Modelle und kann helfen, Fragmentationsfunktionen und nukleare Partonverteilungsfunktionen weiter einzuschränken.

Appendix A

Appendix

A.1 Invariant Mass Distributions

Figure A.1 shows the invariant mass distributions for all analyzed p_T bins of the π^0 minimum bias analysis. The raw signal before background subtraction is shown in black, the scaled mixed event background estimate in blue. The blue band in the upper right of each plot indicates the region to which the mixed event background is normalized. π^0 invariant mass distributions for all analyzed p_T bins after subtraction of the mixed event background estimate are presented in Fig. A.2. The fit to the signal peak is shown in cyan, the linear fit to describe possible remaining background is blue. The reconstructed meson mass that is determined from the signal fit is represented as red vertical line. The limits of the standard signal integration range are depicted as solid lines. Narrower and wider integration ranges to estimate the uncertainty of the yield extraction process are represented by the dotted and dashed lines, respectively.

The corresponding invariant mass distributions for the η analysis are shown in Fig. A.3 and Fig. A.4.
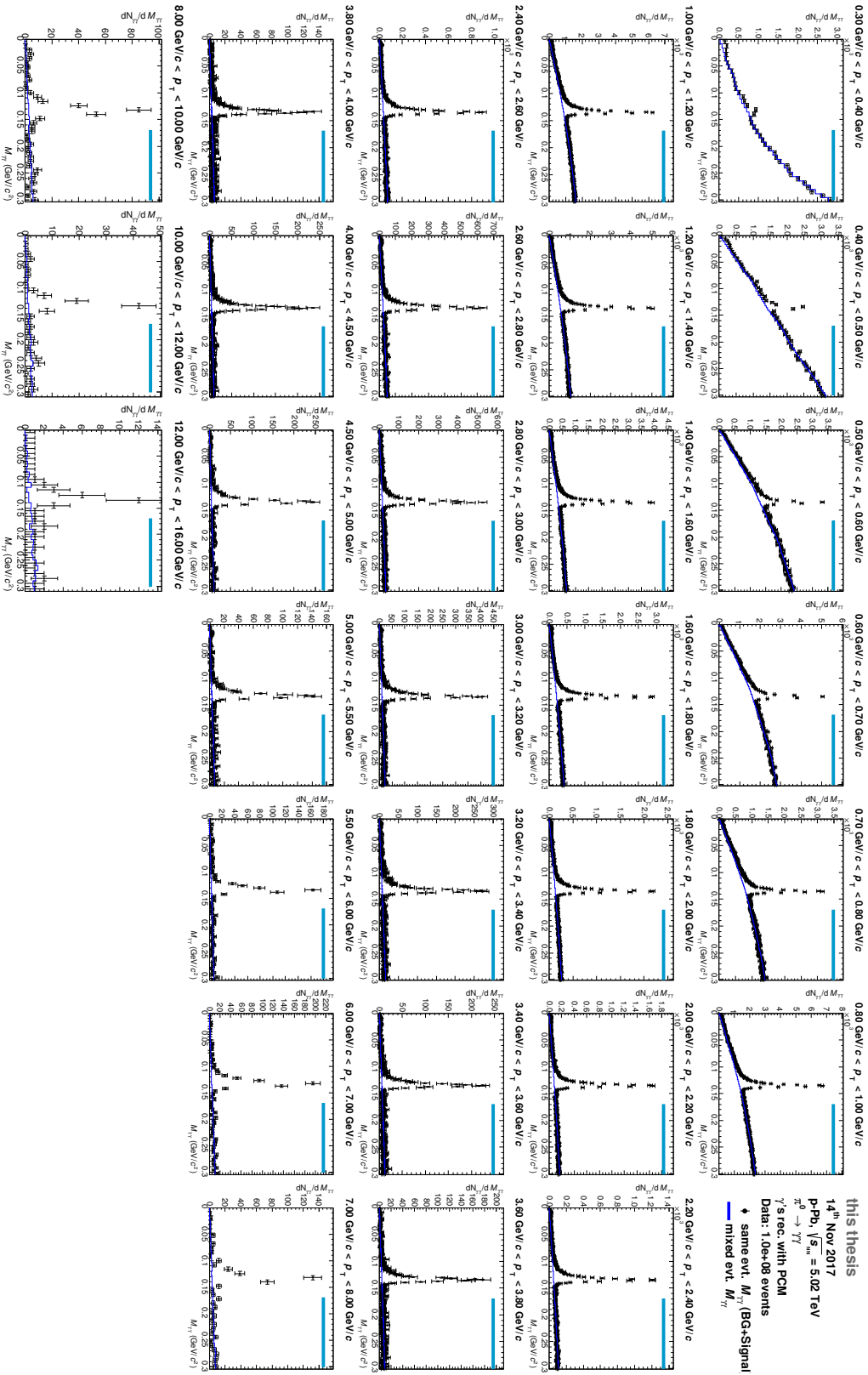
Figure A.1: π^0 invariant mass distributions with combinatorial background.
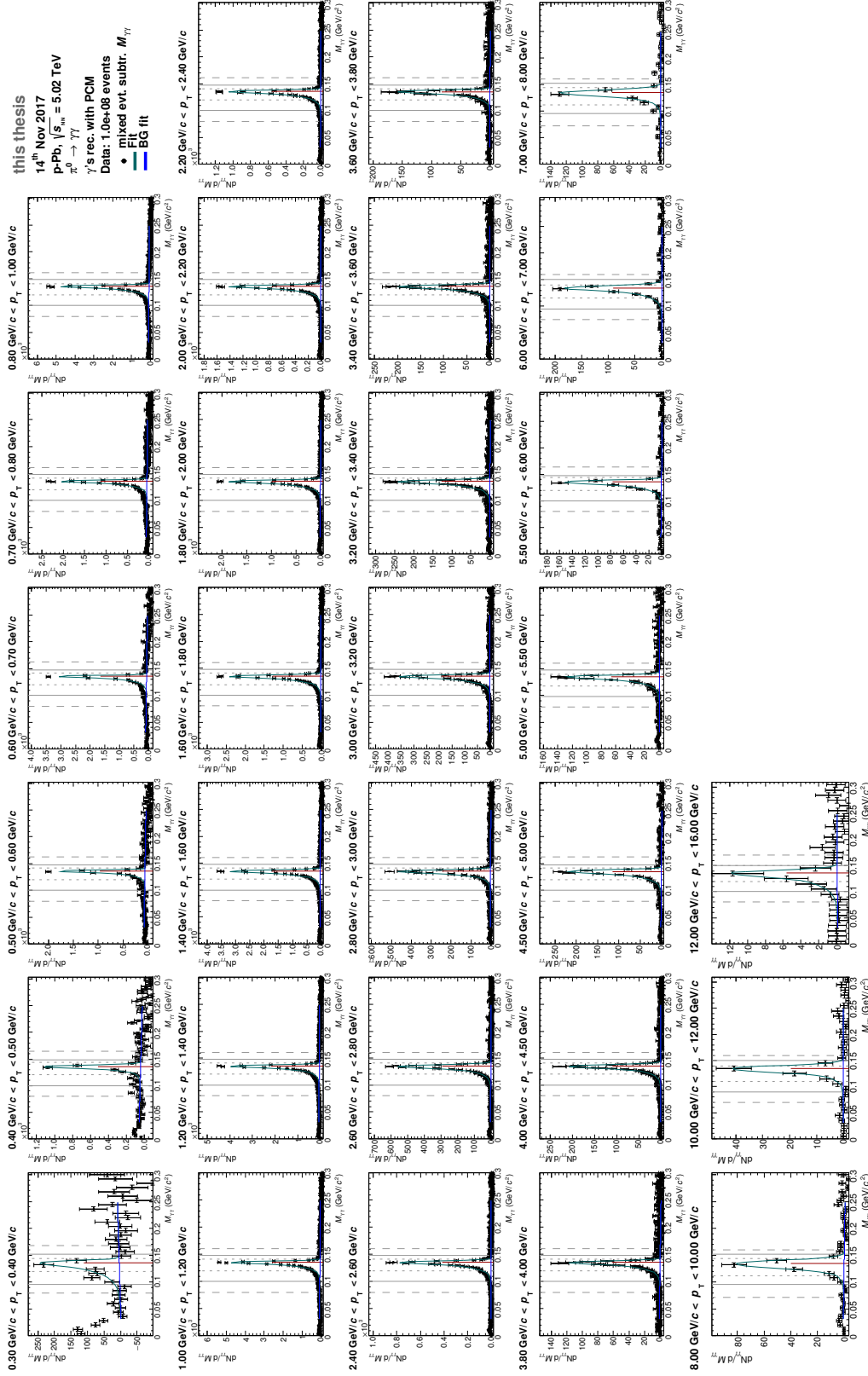
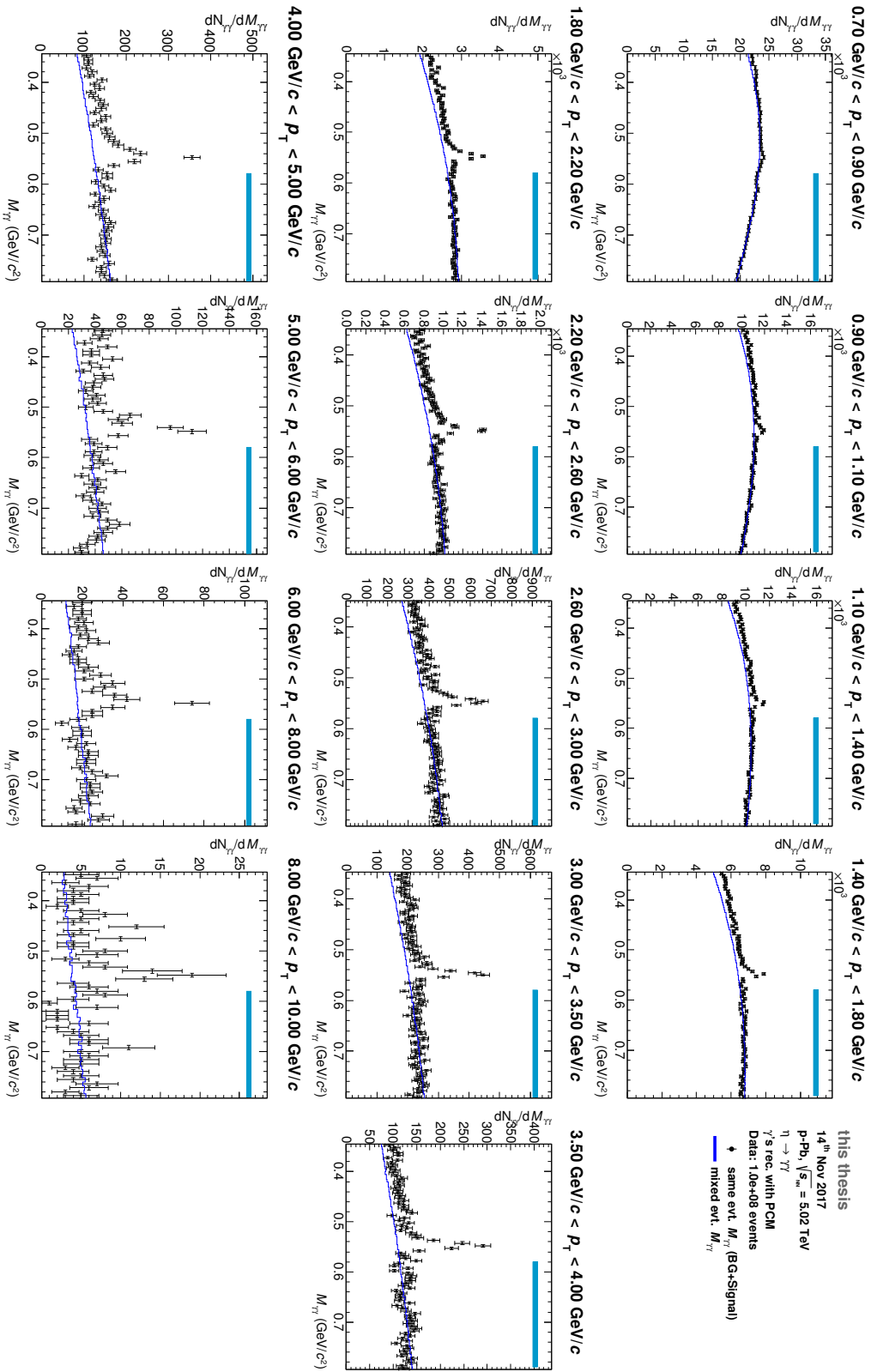Figure A.2: π^0 Invariant mass distributions after background subtraction.

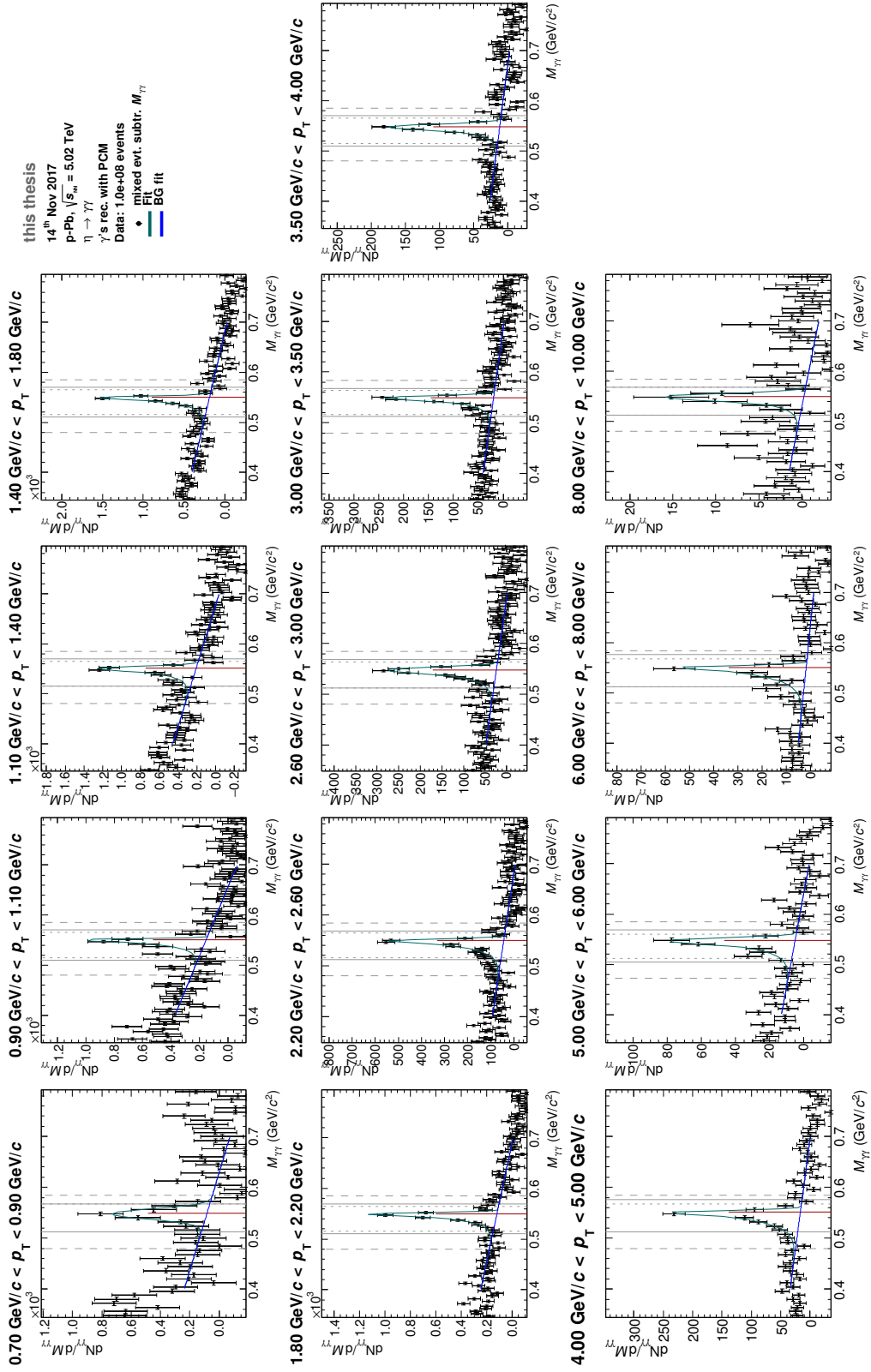Figure A.3: η invariant mass distributions with combinatorial background.

Figure A.4: η invariant mass distributions after background subtraction.
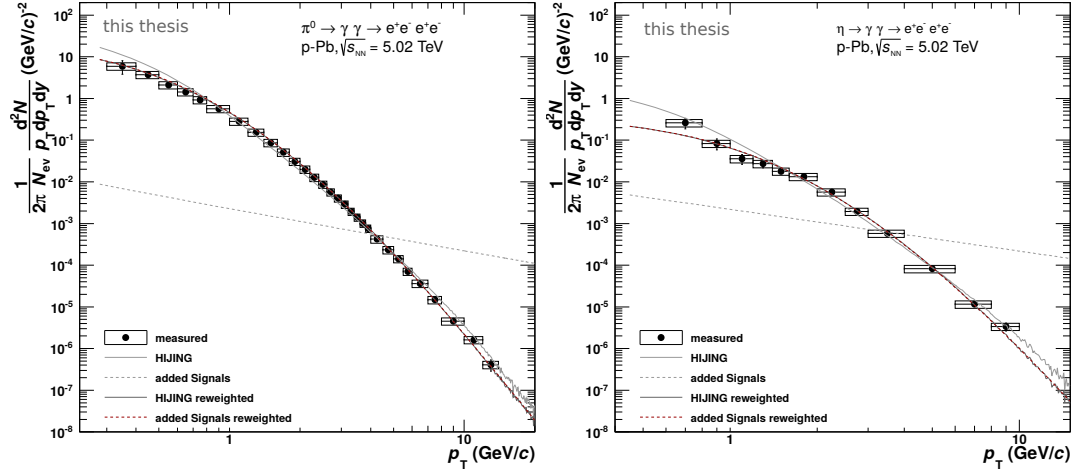
A.2   Monte Carlo Reweighting

Figure A.5: Invariant π^0 (left) and η (right) yields for data and Monte Carlo simulations. The minimum bias and the added signal part of the HIJING sample are shown with and without applied weights.

A.3 Systematic Uncertainties

In Fig. A.6-Fig. A.8 the systematic uncertainties for all cut variations of the π^0, η and η/π^0 analysis are presented. All uncertainties, except for the yield extraction, have completely or partially been smoothed with a polynomial or an exponential function to suppress statistical fluctuations. The quadratic sum of all uncertainties excluding the material budget error is shown in black, the full systematic uncertainty including the material budget error is shown in red. In case of the η/π^0 ratio, the material budget uncertainty completely cancels out.
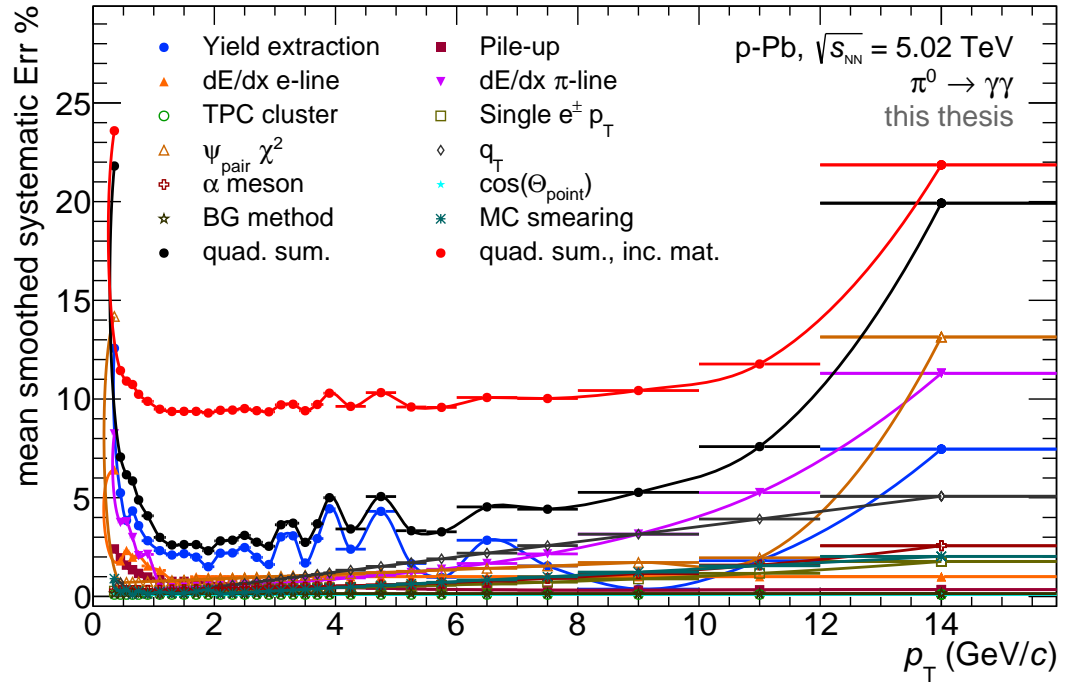

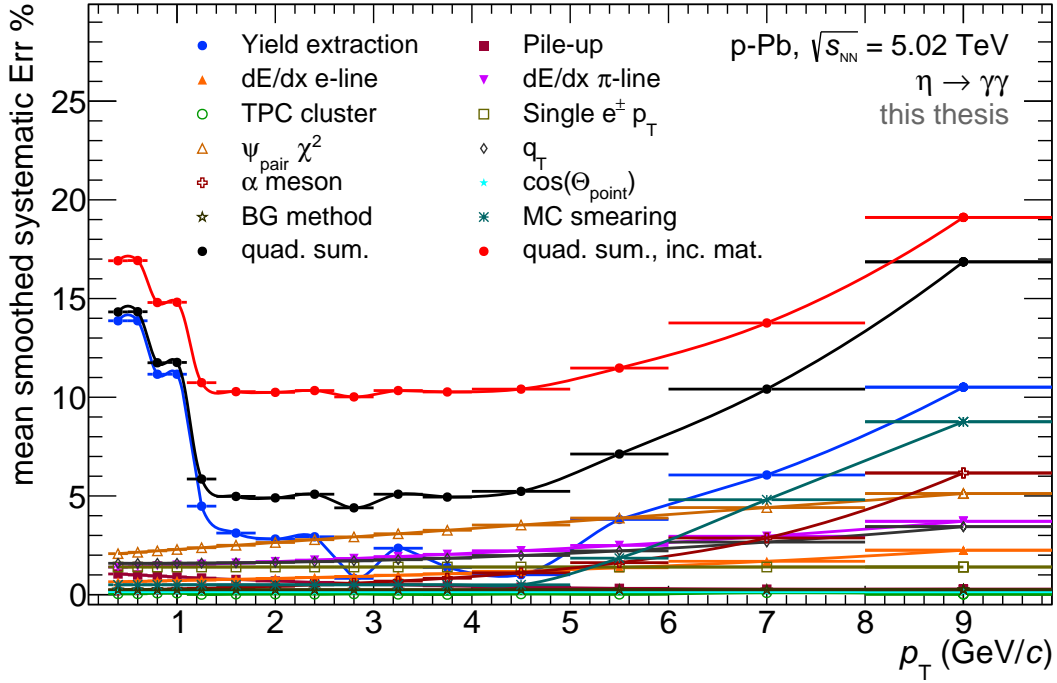Figure A.6: Systematic uncertainties for all cut variations of the π^0 analysis.

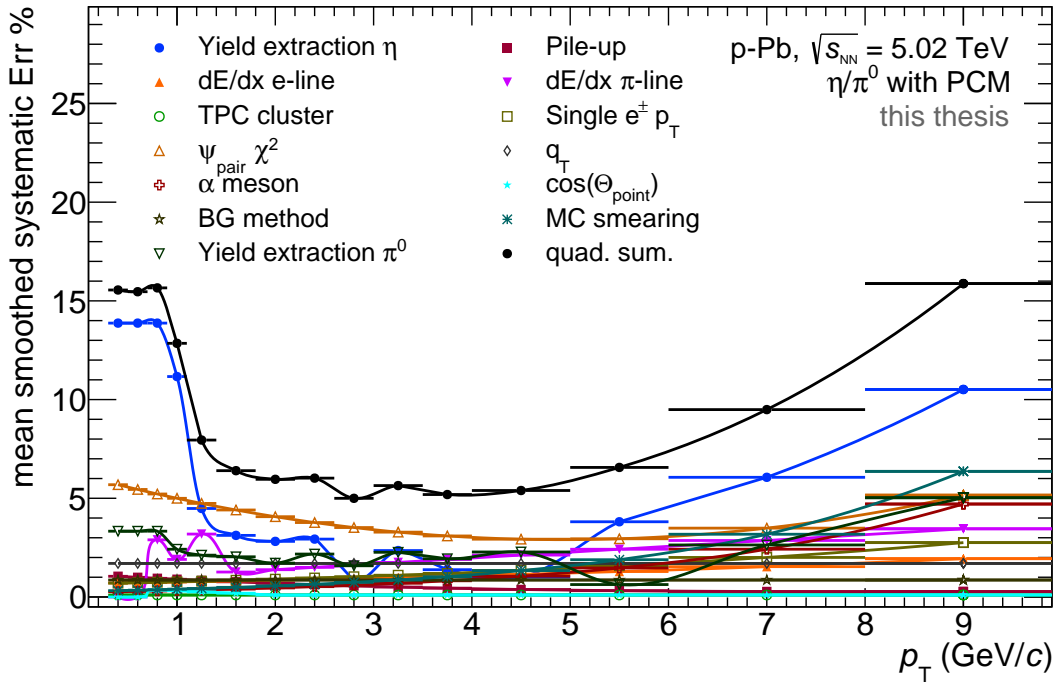Figure A.7: Systematic uncertainties for all cut variations of the η analysis.

Figure A.8: Systematic uncertainties for all cut variations of the η/π^0 ratio.

A.4 Multiplicity Dependent η/π^0 Ratios

Figure A.9-Fig. A.12 show the η/π^0 ratio for different V0A multiplicity classes, together with the minimum bias result. Statistical and systematic uncertainties are added in quadrature. The limited statistics, especially for lower event multiplicities, lead to large uncertainties. Within these uncertainties, a significant deviation from the minimum bias result cannot be observed for any multiplicity class.

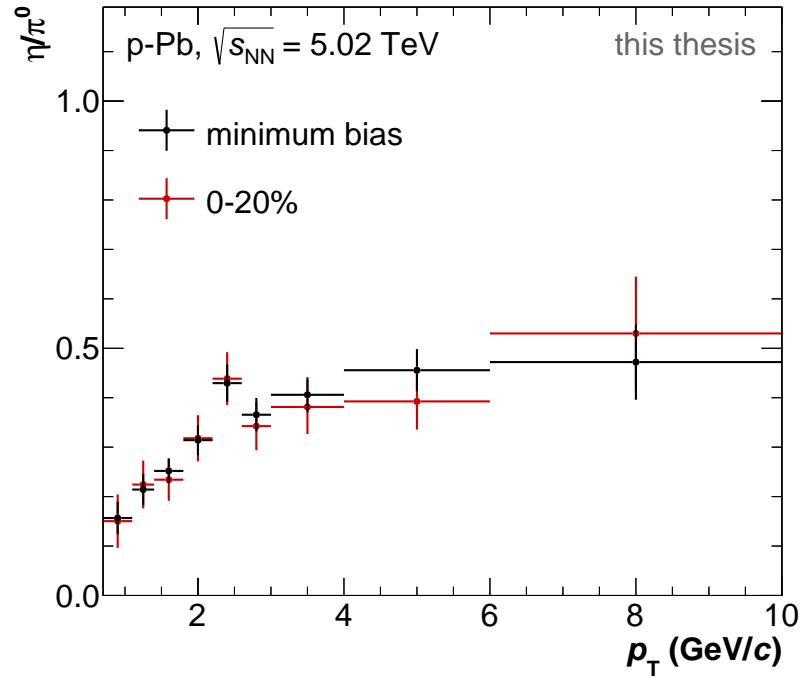Figure A.9: η/π^0 ratio with total uncertainties for minimum bias and 0-20% V0A multiplicity.
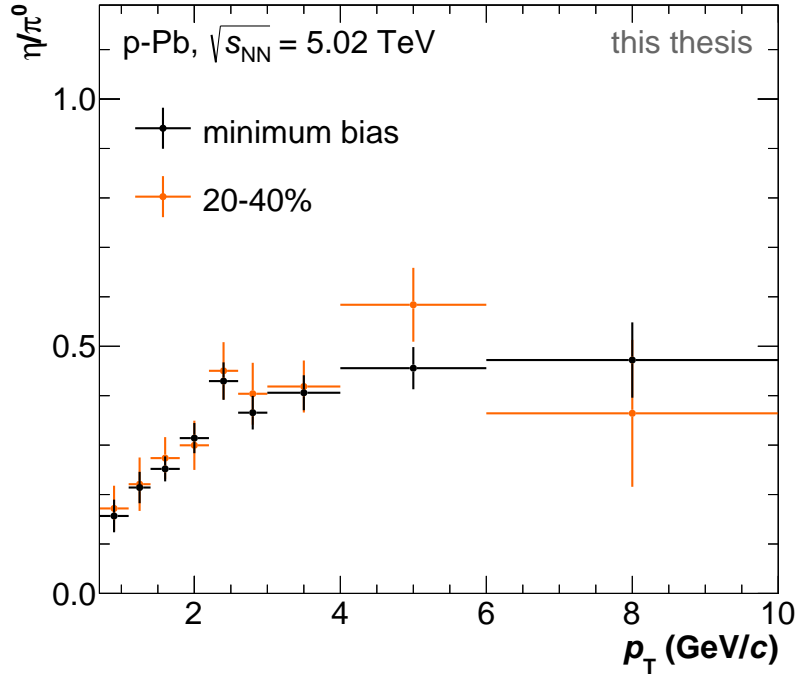
Figure A.10: η/π^0 ratio with total uncertainties for minimum bias and 20-40% V0A multiplicity.
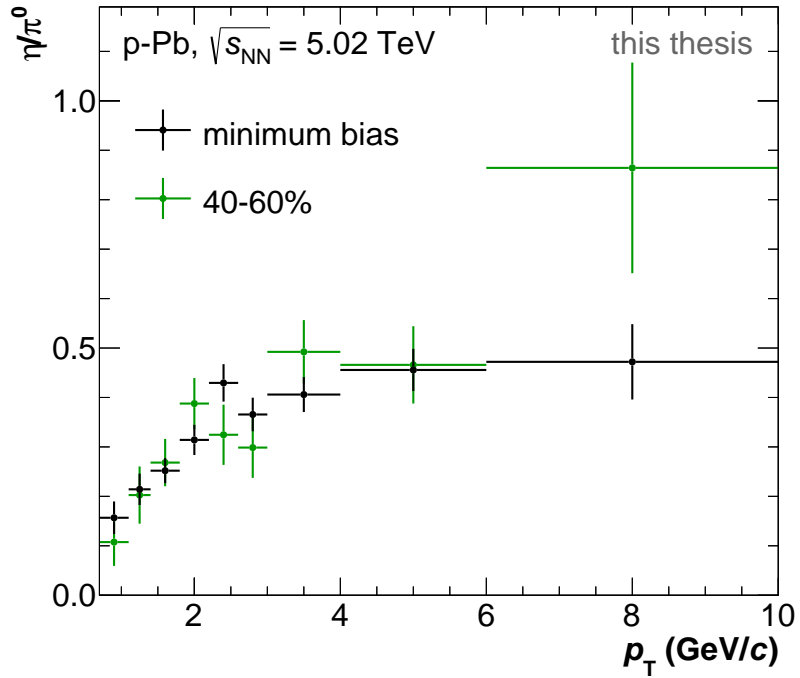

Figure A.11: η/π^0 ratio with total uncertainties for minimum bias and 40-60% V0A multiplicity.
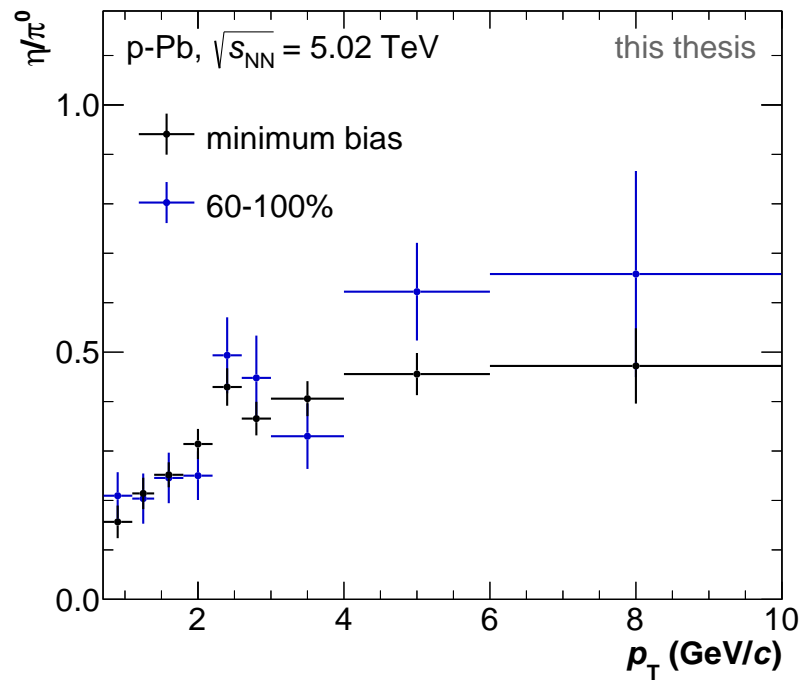
Figure A.12: η/π⁰ ratio with total uncertainties for minimum bias and 60-100% V0A multiplicity.

Bibliography

[1] **ALICE** Collaboration, B. Abelev *et al.*, "Neutral pion production at midrapidity in pp and Pb–Pb collisions at $\sqrt{s_{\mathrm{NN}}} = 2.76\,\mathrm{TeV}$," *Eur. Phys. J.* **C74** no. 10, (2014) 3108, arXiv:1405.3794 [nucl-ex].

[2] **ALICE** Collaboration, B. Abelev *et al.*, "Long-range angular correlations on the near and away side in p-Pb collisions at $\sqrt{s_{NN}} = 5.02\,\mathrm{TeV}$," *Phys. Lett.* **B719** (2013) 29–41, arXiv:1212.2001 [nucl-ex].

[3] **CMS** Collaboration, V. Khachatryan *et al.*, "Evidence for collectivity in pp collisions at the LHC," *Phys. Lett.* **B765** (2017) 193–220, arXiv:1606.06198 [nucl-ex].

[4] C. A. Salgado *et al.*, "Proton-Nucleus Collisions at the LHC: Scientific Opportunities and Requirements," *J. Phys.* **G39** (2012) 015010, arXiv:1105.3919 [hep-ph].

[5] **ALICE** Collaboration, J. Adam *et al.*, "Direct photon production in Pb-Pb collisions at $\sqrt{s_{\mathrm{NN}}} = 2.76\,\mathrm{TeV}$," *Phys. Lett.* **B754** (2016) 235–248, arXiv:1509.07324 [nucl-ex].

[6] **ALICE** Collaboration, S. Acharya *et al.*, "Direct photon production at low transverse momentum in proton-proton collisions at $\sqrt{\mathbf{s}} = \mathbf{2.76}$ and 8 TeV," arXiv:1803.09857 [nucl-ex].

[7] **ALICE** Collaboration, J. Adam *et al.*, "Measurement of electrons from heavy-flavour hadron decays in p-Pb collisions at $\sqrt{s_{\mathrm{NN}}} = 5.02\,\mathrm{TeV}$," *Phys. Lett.* **B754** (2016) 81–93, arXiv:1509.07491 [nucl-ex].

[8] R. R. G. Musiol, J. Ranft and D. Seeliger, "Kern- und Elementarteilchenphysik," *VCH Verlagsgesellschaft Weinheim* (1988) . https://doi.org/10.1002/piuz.19890200109.

[9] G. Dissertori, I. Knowles, and M. Schmelling, "Quantum chromodynamics: High energy experiments and theory," *Clarendon Press* (2003) . `https://books.google.de/books?id=9PtKDgAAQBAJ`.

[10] M. L. Perl, E. R. Lee, and D. Loomba, "Searches for fractionally charged particles," *Ann. Rev. Nucl. Part. Sci.* **59** (2009) 47–65.

[11] C. Berger, "Elementarteilchenphysik," *Springer* (2006) .

[12] B. Andersson, G. Gustafson, G. Ingelman, and T. Sjostrand, "Parton Fragmentation and String Dynamics," *Phys. Rept.* **97** (1983) 31–145.

[13] **Particle Data Group** Collaboration, C. Patrignani *et al.*, "Review of Particle Physics," *Chin. Phys.* **C40** (2016) 100001.

[14] K. G. Wilson, "Confinement of quarks," *Phys. Rev. D* **10** (Oct, 1974) 2445–2459. `https://link.aps.org/doi/10.1103/PhysRevD.10.2445`.

[15] C. Klein-Bösing, "Study of the quark-gluon plasma with hard and electromagnetic probes," *Habilitation, Westfälische Wilhelms-Universität Münster* (2013) . `https://www.uni-muenster.de/imperia/md/content/physik_kp/agwessels/thesis_db/ag_wessels/klein-boesing_c_2013_habilitation.pdf`.

[16] M. Kliemant, R. Sahoo, T. Schuster, and R. Stock, "Global Properties of Nucleus-Nucleus Collisions," *Lect. Notes Phys.* **785** (2010) 23–103, `arXiv:0809.2482 [nucl-ex]`.

[17] E. Shuryak, "Strongly coupled quark-gluon plasma in heavy ion collisions," *Rev. Mod. Phys.* **89** (Jul, 2017) 035001. `https://link.aps.org/doi/10.1103/RevModPhys.89.035001`.

[18] J. C. Collins, D. E. Soper, and G. F. Sterman, "Soft Gluons and Factorization," *Nucl. Phys.* **B308** (1988) 833–856.

[19] R. Sassot, P. Zurita, and M. Stratmann, "Inclusive Hadron Production in the CERN-LHC Era," *Phys. Rev.* **D82** (2010) 074011, `arXiv:1008.0540 [hep-ph]`.

[20] **ZEUS** Collaboration, S. Chekanov *et al.*, "A ZEUS next-to-leading-order QCD analysis of data on deep inelastic scattering," *Phys. Rev.* **D67** (2003) 012007, `arXiv:hep-ex/0208023 [hep-ex]`.

[21] M. Arneodo, "Nuclear effects in structure functions," *Physics Reports* **240** no. 5, (1994) 301 – 393. `http://www.sciencedirect.com/science/article/pii/0370157394900485`.

[22] K. J. Eskola, H. Paukkunen, and C. A. Salgado, "EPS09: A New Generation of NLO and LO Nuclear Parton Distribution Functions," *JHEP* **04** (2009) 065, `arXiv:0902.4154 [hep-ph]`.

[23] **European Muon** Collaboration, J. J. Aubert *et al.*, "The ratio of the nucleon structure functions $F2_n$ for iron and deuterium," *Phys. Lett.* **123B** (1983) 275–278.

[24] D. F. Geesaman, K. Saito, , and A. W. Thomas, "The Nuclear EMC Effect," *Annual Review of Nuclear and Particle Science* **45** no. 1, (1995) 337–390, `https://doi.org/10.1146/annurev.ns.45.120195.002005`. `https://doi.org/10.1146/annurev.ns.45.120195.002005`.

[25] K. J. Eskola, P. Paakkinen, H. Paukkunen, and C. A. Salgado, "EPPS16: Nuclear parton distributions with LHC data," *Eur. Phys. J.* **C77** no. 3, (2017) 163, `arXiv:1612.05741 [hep-ph]`.

[26] K. Kovarik *et al.*, "nCTEQ15 - Global analysis of nuclear parton distributions with uncertainties in the CTEQ framework," *Phys. Rev.* **D93** no. 8, (2016) 085037, `arXiv:1509.00792 [hep-ph]`.

[27] J. W. Cronin, H. J. Frisch, M. J. Shochet, J. P. Boymond, R. Mermod, P. A. Piroue, and R. L. Sumner, "Production of hadrons with large transverse momentum at 200, 300, and 400 GeV," *Phys. Rev.* **D11** (1975) 3105–3123.

[28] **ALICE** Collaboration, J. Adam *et al.*, "Multiplicity dependence of charged pion, kaon, and (anti)proton production at large transverse momentum in p–Pb collisions at $\sqrt{s_{\mathrm{NN}}} = 5.02$ TeV," *Phys. Lett.* **B760** (2016) 720–735, `arXiv:1601.03658 [nucl-ex]`.

[29] F. Gelis, "Color Glass Condensate and Glasma," *Int. J. Mod. Phys.* **A28** (2013) 1330001, `arXiv:1211.3327 [hep-ph]`.

[30] F. Gelis, E. Iancu, J. Jalilian-Marian, and R. Venugopalan, "The Color Glass Condensate," *Ann. Rev. Nucl. Part. Sci.* **60** (2010) 463–489, `arXiv:1002.0333 [hep-ph]`.

[31] D. H. Perkins, "Hochenergiephysik," *Addison-Wesley* (1990) .

[32] A. Bramon, R. Escribano, and M. D. Scadron, "The eta - eta-prime mixing angle revisited," *Eur. Phys. J.* **C7** (1999) 271–278, `arXiv:hep-ph/9711229 [hep-ph]`.

[33] P. Kroll, "Mixing of pseudoscalar mesons and isospin symmetry breaking," *Int. J. Mod. Phys.* **A20** (2005) 331–340, `arXiv:hep-ph/0409141 [hep-ph]`.

[34] J. H. Christenson, J. W. Cronin, V. L. Fitch, and R. Turlay, "Evidence for the 2π Decay of the K_2^0 Meson," *Phys. Rev. Lett.* **13** (Jul, 1964) 138–140. `https://link.aps.org/doi/10.1103/PhysRevLett.13.138`.

[35] K. Kleinknecht, "Detektoren für Teilchenstrahlung," *Springer* (2005) .

[36] K. Bethge, "Kernphysik," *Springer* (2008) .

[37] Y.-S. Tsai, "Pair production and bremsstrahlung of charged leptons," *Rev. Mod. Phys.* **46** (Oct, 1974) 815–851. `https://link.aps.org/doi/10.1103/RevModPhys.46.815`.

[38] H. Davies, H. A. Bethe, and L. C. Maximon, "Theory of bremsstrahlung and pair production. ii. integral cross section for pair production," *Phys. Rev.* **93** (Feb, 1954) 788–795. `https://link.aps.org/doi/10.1103/PhysRev.93.788`.

[39] L. Evans and P. Bryant, "LHC Machine," *JINST* **3** (2008) S08001.

[40] S. Myers, "The LEP Collider, from design to approval and commissioning," *CERN* (1991) . `http://cds.cern.ch/record/226776`. Delivered at CERN, 26 Nov 1990.

[41] C. Lefèvre, "The CERN accelerator complex. Complexe des accélérateurs du CERN." Dec, 2008.

[42] **ATLAS** Collaboration, G. Aad *et al.*, "The ATLAS Experiment at the CERN Large Hadron Collider," *JINST* **3** (2008) S08003.

[43] **CMS** Collaboration, S. Chatrchyan *et al.*, "The CMS experiment at the CERN LHC," *JINST* **3** (2008) S08004.

[44] **LHCb** Collaboration, A. A. Alves, Jr. *et al.*, "The LHCb Detector at the LHC," *JINST* **3** (2008) S08005.

[45] **ALICE** Collaboration, K. Aamodt *et al.*, "The ALICE experiment at the CERN LHC," *JINST* **3** (2008) S08002.

[46] **ATLAS** Collaboration, G. Aad *et al.*, "Observation of a new particle in the search for the Standard Model Higgs boson with the ATLAS detector at the LHC," *Phys. Lett.* **B716** (2012) 1–29, `arXiv:1207.7214 [hep-ex]`.

[47] **CMS** Collaboration, S. Chatrchyan *et al.*, "Observation of a new boson at a mass of 125 GeV with the CMS experiment at the LHC," *Phys. Lett.* **B716** (2012) 30–61, `arXiv:1207.7235 [hep-ex]`.

[48] F. Marcastel, "CERN's Accelerator Complex. La chaîne des accélérateurs du CERN,". `https://cds.cern.ch/record/1621583`. General Photo.

[49] **ALICE** Collaboration, "Alice webpage." `http://aliceinfo.cern.ch/`.

[50] B. Adeva *et al.*, "The construction of the L3 experiment," *Nuclear Instruments and Methods in Physics Research Section A: Accelerators, Spectrometers, Detectors and Associated Equipment* **289** no. 1, (1990) 35 – 102. `http://www.sciencedirect.com/science/article/pii/016890029090250A`.

[51] N. Readioff, "The Large Hadron Collider." `https://build-your-own-particle-detector.org/models/lhc-micro-models`.

[52] **ALICE** Collaboration, G. Dellacasa *et al.*, "ALICE technical design report of the inner tracking system (ITS),".

[53] J. Alme *et al.*, "The ALICE TPC, a large 3-dimensional tracking device with fast readout for ultra-high multiplicity events," *Nucl. Instrum. Meth.* **A622** (2010) 316–367, `arXiv:1001.1950 [physics.ins-det]`.

[54] **ALICE** Collaboration, G. Dellacasa *et al.*, "ALICE technical design report of the photon spectrometer (PHOS)," CERN-LHCC-99-04.

[55] **ALICE** Collaboration, P. Cortese *et al.*, "ALICE Electromagnetic Calorimeter Technical Design Report," Tech. Rep. CERN-LHCC-2008-014. ALICE-TDR-14, Aug, 2008. `https://cds.cern.ch/record/1121574`.

[56] **ALICE EMCal** Collaboration, U. Abeysekara *et al.*, "ALICE EMCal Physics Performance Report," `arXiv:1008.0413 [physics.ins-det]`.

[57] J. Allen *et al.*, "ALICE DCal: An Addendum to the EMCal Technical Design Report Di-Jet and Hadron-Jet correlation measurements in ALICE," Tech. Rep. CERN-LHCC-2010-011. ALICE-TDR-14-add-1, Jun, 2010. `https://cds.cern.ch/record/1272952`.

[58] **ALICE** Collaboration, P. Cortese *et al.*, "ALICE technical design report on forward detectors: FMD, T0 and V0,".

[59] **ALICE** Collaboration, E. Abbas *et al.*, "Performance of the ALICE VZERO system," *JINST* **8** (2013) P10016, `arXiv:1306.3130 [nucl-ex]`.

[60] **ALICE** Collaboration, B. B. Abelev *et al.*, "Performance of the ALICE Experiment at the CERN LHC," *Int. J. Mod. Phys.* **A29** (2014) 1430044, `arXiv:1402.4476 [nucl-ex]`.

[61] Y. Belikov, M. Ivanov, K. Safarik, and J. Bracinik, "TPC tracking and particle identification in high density environment," *eConf* **C0303241** (2003) TULT011, `arXiv:physics/0306108 [physics]`.

[62] R. Frühwirth, "Application of Kalman filtering to track and vertex fitting," *Nuclear Instruments and Methods in Physics Research Section A: Accelerators, Spectrometers, Detectors and Associated Equipment* **262** no. 2, (1987) 444 – 450. `http://www.sciencedirect.com/science/article/pii/0168900287908874`.

[63] **ALICE** Collaboration, G. Dellacasa *et al.*, "ALICE technical design report of the time-of-flight system (TOF)," 2000.

[64] **ALICE** Collaboration, P. Cortese, "ALICE transition-radiation detector: Technical Design Report," 2001. `https://cds.cern.ch/record/519145`.

[65] **ALICE** Collaboration, "Alice offline - aliroot documentation." `http://alice-offline.web.cern.ch/AliRoot/Manual.html`.

[66] R. Brun and F. Rademakers, "ROOT: An object oriented data analysis framework," 1997.

[67] "Paw webpage." `http://paw.web.cern.ch/paw/`.

[68] Sjötrand *et al.*, "An Introduction to PYTHIA 8.2," *Comput. Phys. Commun.* **191** (2015) 159–177, `arXiv:1410.3012 [hep-ph]`.

[69] Gyulassy, Miklos and Wang, Xin-Nian, "HIJING 1.0: A Monte Carlo program for parton and particle production in high-energy hadronic and nuclear collisions," *Comput. Phys. Commun.* **83** (1994) 307, `arXiv:nucl-th/9502021 [nucl-th]`.

[70] S. Roesler, R. Engel, and J. Ranft, "The Monte Carlo event generator DPMJET-III," in *Advanced Monte Carlo for radiation physics, particle transport simulation and applications. Proceedings, Conference, MC2000, Lisbon, Portugal, October 23-26, 2000*, pp. 1033–1038. 2000. `arXiv:hep-ph/0012252 [hep-ph]`.

[71] R. Brun, R. Hagelberg, M. Hansroul, and J. Lassalle, "Simulation program for particle physics experiments, GEANT: user guide and reference manual," *CERN* (1978) . `https://cds.cern.ch/record/118715`.

[72] **ALICE** Collaboration, "Alien webpage." `http://alien.web.cern.ch/`.

[73] **ALICE** Collaboration, "Photon conversion group." `https://twiki.cern.ch/twiki/bin/view/ALICE/PWG4GammaConversion`.

[74] A. Capella, U. Sukhatme, C.-I. Tan, and J. T. T. Van, "Dual parton model," *Physics Reports* **236** no. 4, (1994) 225 – 329. `http://www.sciencedirect.com/science/article/pii/0370157394900647`.

[75] K. Koch, "Measurement of π^0 and η mesons with photon conversions in alice in proton-proton collisions at $\sqrt{s} = 0.9, 2.76, 7$ tev," February, 2012. `http://www.ub.uni-heidelberg.de/archiv/13113`.

[76] F. Bock, "Neutral Pion and Eta Meson Production in pp and Pb–Pb Collisions at the LHC with the ALICE Detector," Master's thesis, University Heidelberg, December, 2012. `http://www.physi.uni-heidelberg.de//Publications/Bock-Masterthesis.pdf`.

[77] S. Gorbunov and I. Kisel, "AliKFParticle package." `https://github.com/alisw/AliRoot/blob/master/STEER/ESD/AliKFParticle.h`.

[78] S. Gorbunov and I. Kisel, "Reconstruction of decayed particles based on the kalman filter," *CBM-SOFT note 2007-003* .

[79] **PHENIX** Collaboration, T. Dahms, "Measurement of photons via conversion pairs in $\sqrt{s_{\mathrm{NN}}} = 200$ GeV Au+Au collisions with the PHENIX experiment at RHIC," *Eur. Phys. J.* **C49** (2007) 249–253, `arXiv:nucl-ex/0608009 [nucl-ex]`.

[80] J. Podolanski and R. Armenteros, "III. Analysis of V-events," *Philosophical Magazine* **45** no. 360, (1954) 13–30.

[81] **ALICE** Collaboration, "The ALICE definition of primary particles,". `https://cds.cern.ch/record/2270008`.

[82] **ALICE** Collaboration, B. Abelev *et al.*, "Multiplicity Dependence of Pion, Kaon, Proton and Lambda Production in p–Pb Collisions at $\sqrt{s_{\mathrm{NN}}} = 5.02$ TeV," *Phys. Lett.* **B728** (2014) 25–38, `arXiv:1307.6796 [nucl-ex]`.

[83] **ALICE** Collaboration, "Run condition table." `https://alimonitor.cern.ch/configuration`.

[84] M. Wilde, "Measurement of direct photons in pp and pb-pb collisions with conversion pairs," 2015. `https://www.uni-muenster.de/imperia/md/content/physik_kp/agwessels/thesis_db/ag_wessels/wilde_2015_dissertation.pdf`.

[85] G. Lafferty and T. Wyatt, "Where to stick your data points: The treatment of measurements within wide bins," *Nuclear Instruments and Methods in Physics Research Section A: Accelerators, Spectrometers, Detectors and Associated Equipment* **355** no. 2, (1995) 541 – 547. `http://www.sciencedirect.com/science/article/pii/0168900294011125`.

[86] C. Tsallis, "Possible generalization of Boltzmann-Gibbs statistics," *Journal of Statistical Physics* **52** no. 1, (1988) 479–487.

[87] A. Bylinkin, N. S. Chernyavskaya, and A. A. Rostovtsev, "Predictions on the transverse momentum spectra for charged particle production at LHC-energies from a two component model," *Eur. Phys. J.* **C75** no. 4, (2015) 166, `arXiv:1501.05235 [hep-ph]`.

[88] F. Bock, "ALICE Capabilities for Studying Photon Physics with the Conversion Method at LHC Energies," June, 2010. `http://www.physi.uni-heidelberg.de//Publications/Bock-Bachelorthesis.pdf`.

[89] **ALICE** Collaboration, J. Adam *et al.*, "Centrality dependence of particle production in p-Pb collisions at $\sqrt{s_{\mathrm{NN}}}$= 5.02 TeV," *Phys. Rev.* **C91** no. 6, (2015) 064905, `arXiv:1412.6828 [nucl-ex]`.

[90] **ALICE** Collaboration, S. Acharya *et al.*, "Neutral pion and η meson production in p-Pb collisions at $\sqrt{s_{\mathrm{NN}}} = 5.02$ TeV," *submitted to EPJC* (2018) , `arXiv:1801.07051 [nucl-ex]`.

[91] **ALICE** Collaboration, B. Abelev *et al.*, "Pseudorapidity density of charged particles in p+Pb collisions at $\sqrt{s_{NN}}$=5.02 TeV," *Phys. Rev. Lett.* **110** (Jan, 2013) 032301.
`https://link.aps.org/doi/10.1103/PhysRevLett.110.032301`.

[92] **ALICE** Collaboration, B. Abelev *et al.*, "Transverse momentum distribution and nuclear modification factor of charged particles in p-Pb collisions at $\sqrt{s_{\mathrm{NN}}} = 5.02$ TeV," *Phys. Rev. Lett.* **110** no. 8, (2013) 082302, `arXiv:1210.4520 [nucl-ex]`.

[93] **ALICE** Collaboration, S. Acharya *et al.*, "Production of π^0 and η mesons up to high transverse momentum in pp collisions at 2.76 TeV," *Eur. Phys. J.* **C77** no. 5, (2017) 339, `arXiv:1702.00917 [hep-ex]`.

[94] **ALICE** Collaboration, B. Abelev *et al.*, "Neutral pion and η meson production in proton-proton collisions at $\sqrt{s} = 0.9$ TeV and $\sqrt{s} = 7$ TeV," *Phys. Lett.* **B717** (2012) 162–172, `arXiv:1205.5724 [hep-ex]`.

[95] **ALICE** Collaboration, S. Acharya *et al.*, "π^0 and η meson production in proton-proton collisions at $\sqrt{s} = 8$ TeV," `arXiv:1708.08745 [hep-ex]`.

[96] **CMS** Collaboration, V. Khachatryan *et al.*, "Transverse-momentum and pseudorapidity distributions of charged hadrons in pp collisions at $\sqrt{s} = 7$ TeV," *Phys. Rev. Lett.* **105** (2010) 022002, `arXiv:1005.3299 [hep-ex]`.

[97] M. L. Miller, K. Reygers, S. J. Sanders, and P. Steinberg, "Glauber modeling in high-energy nuclear collisions," *Annual Review of Nuclear and Particle Science* **57** no. 1, (2007) 205–243.
`https://doi.org/10.1146/annurev.nucl.57.090506.123020`.

[98] P. G. Zamora, "Measurement of the π^0 meson properties through its Dalitz decay channel in pp and p-pPb collisions with the ALICE

experiment at the LHC," 2016. `http://inspirehep.net/record/1503580/files/Thesis-2016-Zamora.pdf`.

[99] T. Okubo and T. Sugitate, "Neutral pion measurement in p-Pb collisions at $\sqrt{s_{NN}}$ = 5.02 TeV.," Jan, 2017. `https://cds.cern.ch/record/2255065`. Presented 16 Feb 2017.

[100] T. Okubo and D. Peressounko, "Measurements of neutral π meson production in p-Pb collisions at $\sqrt{\mathbf{s_{NN}}} = 5.02$ TeV with PHOS detector at ALICE," 2017. `https://aliceinfo.cern.ch/Notes/node/413`. ALICE Analysis Note.

[101] M. Sas, "Neutral meson measurements with EMCal-EMCal in ALICE in pPb collisions at $\sqrt{\mathbf{s_{NN}}} = 5.02$ TeV," 2017. `https://aliceinfo.cern.ch/Notes/node/467`. ALICE Analysis Note.

[102] F. Bock, "Measurement of Direct Photons and Neutral Mesons in Small Collisions Systems with the ALICE Experiment at the LHC ," November, 2017. `http://www.ub.uni-heidelberg.de/archiv/23888`.

[103] L. Lyons, D. Gibaut, and P. Clifford, "How to Combine Correlated Estimates of a Single Physical Quantity," *Nucl. Instrum. Meth.* **A270** (1988) 110.

[104] A. Valassi, "Combining correlated measurements of several different physical quantities," *Nucl. Instrum. Meth.* **A500** (2003) 391–405.

[105] **ALICE** Collaboration, B. Abelev *et al.*, "Pseudorapidity Density of Charged Particles at p + Pb collisions at $\sqrt{s_{NN}}$ = 5.02 TeV," *Phys. Rev. Lett.* **110,032301** (2013) 10.

[106] **PHENIX** Collaboration, S. S. Adler *et al.*, "High transverse momentum η meson production in pp, d–Au, and Au–Au collisions at $\sqrt{s_{NN}} = 200$ GeV," *Phys. Rev. C* **75** (2007) 024909.

[107] G. Agakishiev *et al.*, "Neutral meson production in p–Be and p–Au collisions at 450-GeV beam energy," *Eur. Phys. J.* **C4** (1998) 249–257.

[108] L. Altenkämper, F. Bock, C. Loizides, and N. Schmidt, "Applicability of transverse mass scaling in hadronic collisions at the LHC," `arXiv:1710.01933 [hep-ph]`.

[109] S. Dulat *et al.*, "New parton distribution functions from a global analysis of quantum chromodynamics," *Phys. Rev.* **D93** no. 3, (2016) 033006, `arXiv:1506.07443 [hep-ph]`.

[110] D. de Florian, R. Sassot, M. Epele, R. J. Hernández-Pinto, and M. Stratmann, "Parton-to-Pion Fragmentation Reloaded," *Phys. Rev.* **D91** no. 1, (2015) 014035, `arXiv:1410.6027 [hep-ph]`.

[111] C. A. Aidala, F. Ellinghaus, R. Sassot, J. P. Seele, and M. Stratmann, "Global Analysis of Fragmentation Functions for Eta Mesons," *Phys. Rev.* **D83** (2011) 034002, `arXiv:1009.6145 [hep-ph]`.

[112] F. Bopp and J. Ranft, "Inclusive distributions in p-p collisions at LHC energies compared with an adjusted DPMJET-III model with chain fusion," in *Proceedings, 3rd International Workshop on Multiple Partonic Interactions at the LHC (MPI@LHC 2011): Hamburg, Germany, 21-25 Nov 2011*, pp. 41–49. 2011. `arXiv:1110.6403 [hep-ph]`.

[113] T. Lappi and H. Mäntysaari, "Single inclusive particle production at high energy from HERA data to proton-nucleus collisions," *Phys. Rev.* **D88** (2013) 114020, `arXiv:1309.6963 [hep-ph]`.

[114] J. L. Albacete, N. Armesto, J. G. Milhano, P. Quiroga-Arias, and C. A. Salgado, "AAMQS: A non-linear QCD analysis of new HERA data at small-x including heavy quarks," *Eur. Phys. J.* **C71** (2011) 1705, `arXiv:1012.4408 [hep-ph]`.

[115] C. Shen, Z. Qiu, H. Song, J. Bernhard, S. Bass, and U. Heinz, "The iEBE-VISHNU code package for relativistic heavy-ion collisions," *Comput. Phys. Commun.* **199** (2016) 61–85, `arXiv:1409.8164 [nucl-th]`.

[116] C. Shen, J.-F. Paquet, G. S. Denicol, S. Jeon, and C. Gale, "Collectivity and electromagnetic radiation in small systems," *Phys. Rev.* **C95** no. 1, (2017) 014906, `arXiv:1609.02590 [nucl-th]`.

[117] K. Werner, B. Guiot, I. Karpenko, and T. Pierog, "Analysing radial flow features in p–Pb and pp collisions at several TeV by studying identified particle production in EPOS3," *Phys. Rev.* **C89** no. 6, (2014) 064903, `arXiv:1312.1233 [nucl-th]`.

[118] **CMS** Collaboration, S. Chatrchyan *et al.*, "Study of the production of charged pions, kaons, and protons in p–Pb collisions at $\sqrt{s_{\mathrm{NN}}} = 5.02$ TeV," *Eur. Phys. J.* **C74** no. 6, (2014) 2847, `arXiv:1307.3442 [hep-ex]`.

Danksagung

Zum Abschluss möchte ich mich bei allen bedanken, die zum Gelingen dieser Arbeit beigetragen haben.

Ein besonderer Dank geht dabei an Prof. Dr. Johannes P. Wessels für die Möglichkeit, in einem so interessanten Forschungsfeld arbeiten und meine Doktorarbeit anfertigen zu können. PD Dr. Christian Klein-Bösing möchte ich für die tolle Betreuung, viele Ratschläge und seinen moralischen Beistand, wenn es mal nicht so rund lief, danken. Auch Dr. Tom Dietel danke ich für die gute Betreuung und gemeinsame Arbeit gerade zu Beginn meiner Promotion und während meines Forschungsaufenthalts in Kapstadt, der eine ganz besondere Erfahrung für mich darstellt. Ebenso danke ich apl. Prof. Dr. Alfons Khoukaz für sein stets offenes Ohr und seine Expertise in Mesonenfragen.

Generell möchte ich ein großes Dankeschön an meine Arbeitsgruppe und das gesamte Institut für die gute Zusammenarbeit und die tolle Stimmung aussprechen. Auch wenn die Arbeit vielleicht gerade mal keinen Spaß gemacht hat, bin ich immer gerne ins Institut gekommen. Nach einer Pause im Kaffeeraum ist alles besser und nach ner Runde Musikmachen im besten Probenraum Münsters sowieso.

Within the ALICE collaboration I want to thank the photon conversion group and especially the members of the PC and IRC for the fruitful work on the neutral meson p–Pb paper, by the way the 200th ALICE paper - sure, this was on purpose.

Zu guter Letzt möchte ich die Menschen erwähnen, die mich stets abseits der Arbeit unterstützen und mir Halt geben: meine Familie Muttfried, Papusch, Meuki und Wanda und besonders meinen Freund Stefan, der am meisten unter schwierigen Phasen der Promotion zu leiden hatte.
Danke, dass ihr immer für mich da seid.

Lebenslauf

Name	Annika Passfeld
Geburtsdatum	02.01.1985
Geburtsort	Münster
Staatsangehörigkeit	deutsch
Eltern	Erich Passfeld
	Maria Elisabeth Passfeld, geb. Koch
Familienstand	ledig

Schulbildung

1991 - 1995	Grundschule Everswinkel
1995 - 2004	Gymnasium Wolbeck
Juni 2004	Allgemeine Hochschulreife

Studium

10/2004 - 08/2010	Diplomstudiengang Physik an der WWU Münster
09/2006 - 05/2007	Erasmusstudium an der Université Paris-Sud
08/2010	Diplomprüfung

Promotiostudium

seit 11/2010	Beginn der Dissertation am Institut für Kernphysik bei Prof. Dr. J. P. Wessels

Berufstätigkeit

10/2007 - 07/2010	Studentische Hilfskraft am Physikalischen Institut der WWU Münster
08/2010 - 10/2010	Wissenschaftliche Hilfskraft am Institut für Kernphysik der WWU Münster
seit 11/2010	Wissenschaftliche Mitarbeiterin am Institut für Kernphysik der WWU Münster

Münster, 14. Mai 2018